INTENTIONALLY LEFT BLANK

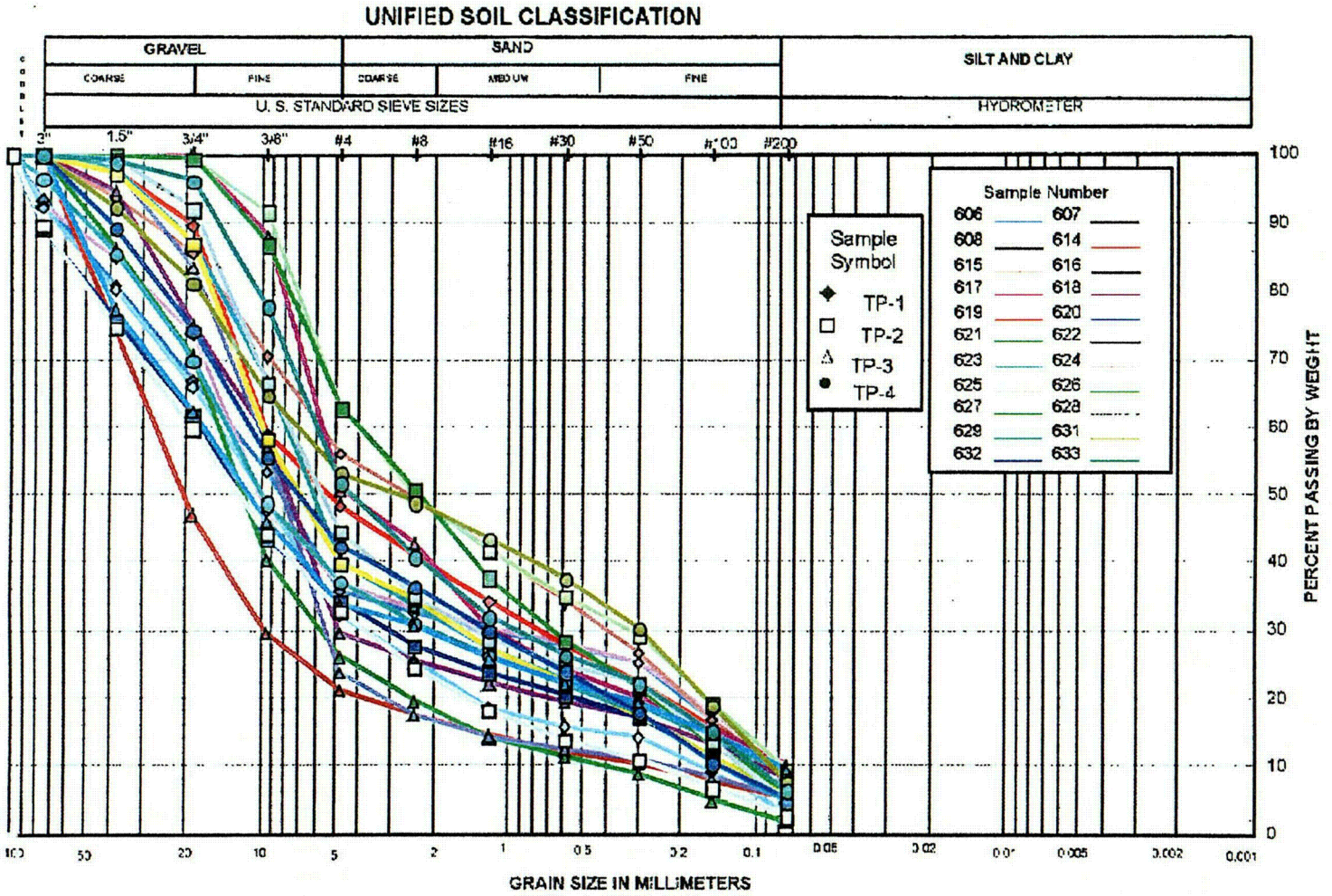

DTN: GS020783114233.005

Figure 102. Particle-Size Distribution Curves for TP-WHB-1 to TP-WHB-4

C01

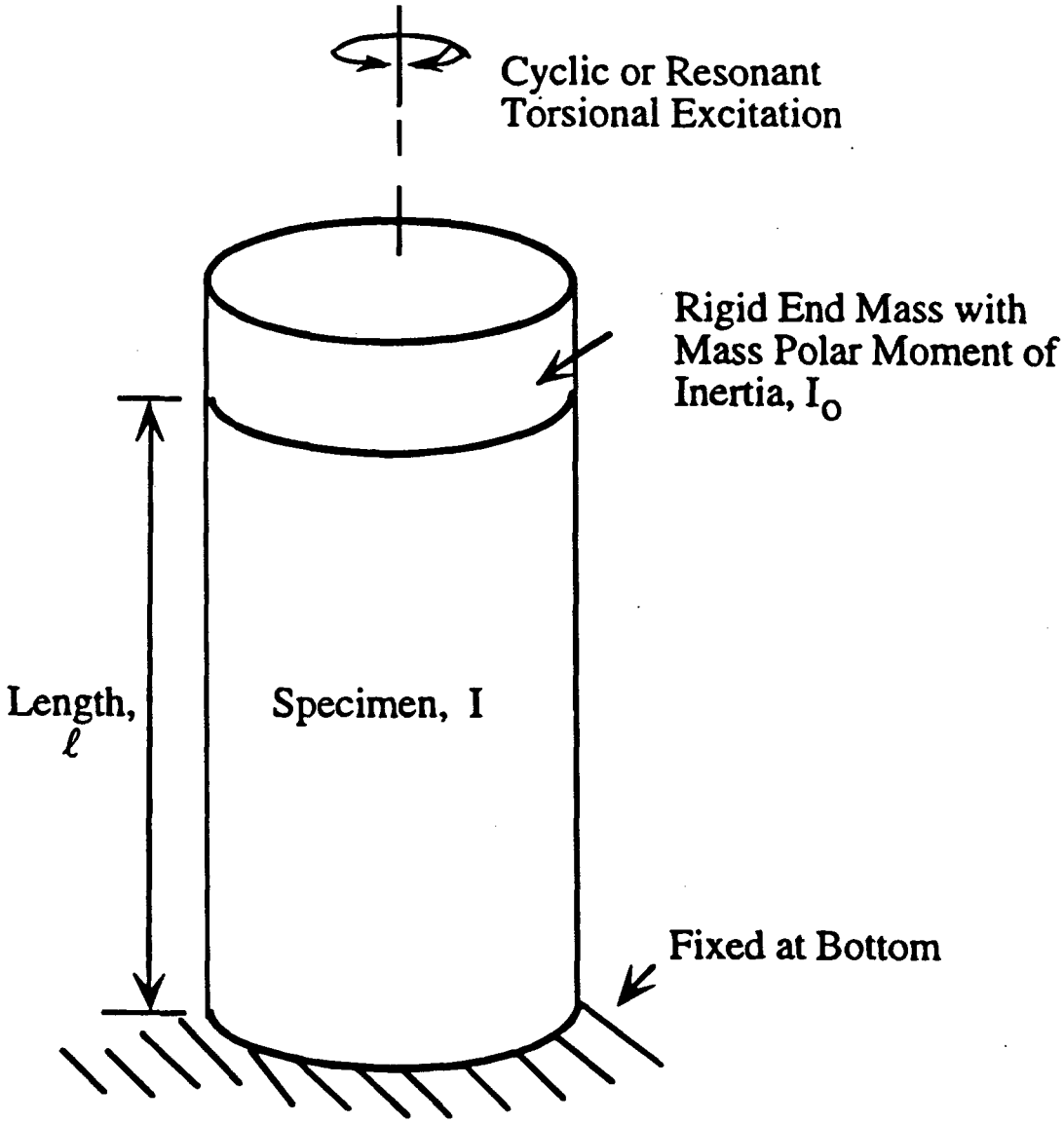

Source: PBRCTS-1 Rev 4 (page 2)

Figure 103. Idealized Fixed-Free RCTS Equipment

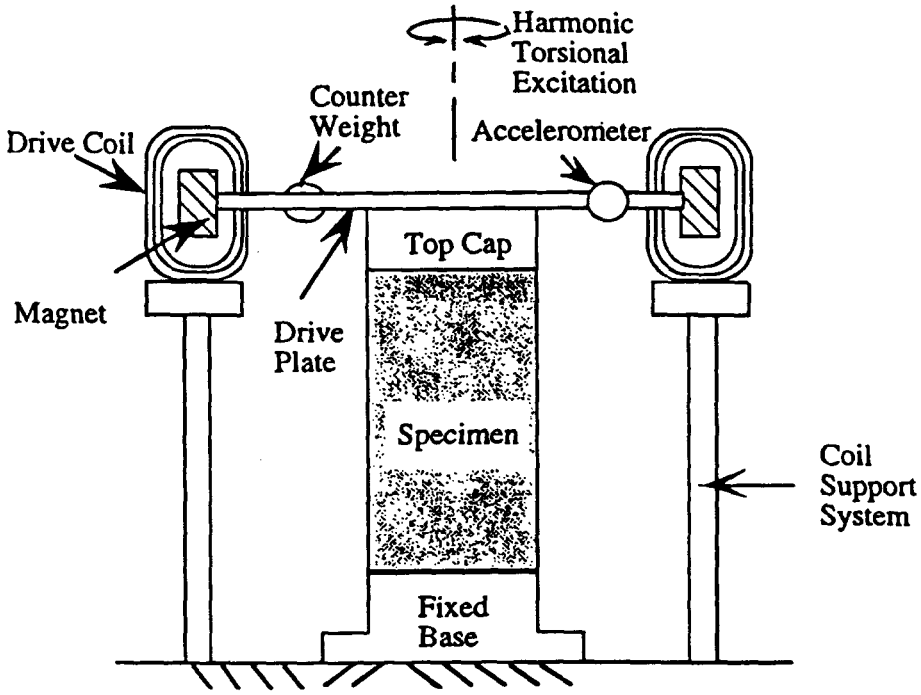

a) Specimen in the Resonant Column Apparatus
(Confinement Chamber Not Shown)

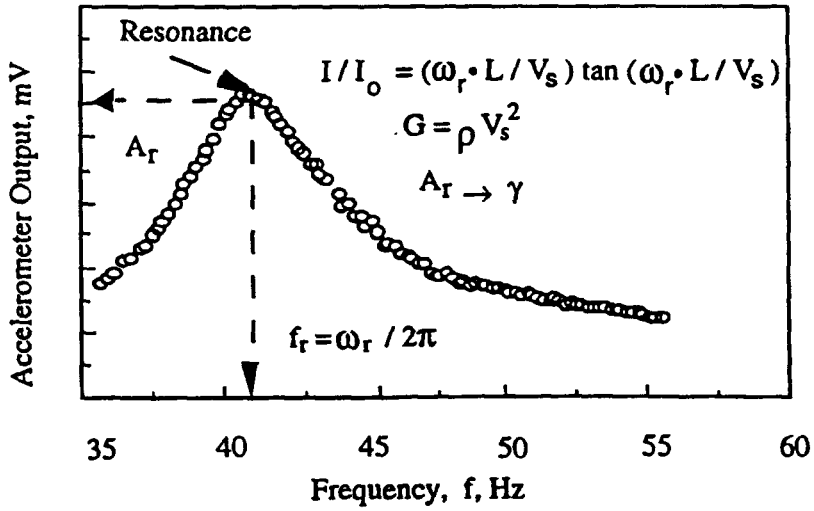

b) Typical Frequency Response Curve

Source: PBRCTS-1 Rev 4 (page 4)

Figure 104. (a) Simplified Diagram of a Fixed-Free Resonant Column Test and (b) an Associated Frequency Response Curve

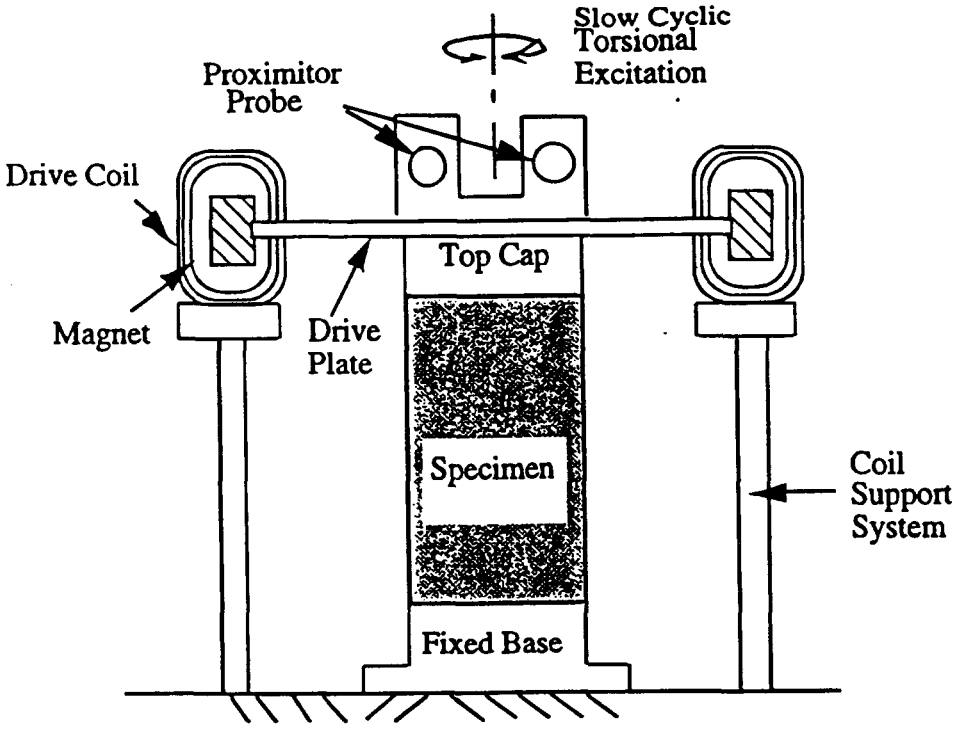

a) Specimen in the Torsional Shear Test Apparatus
(Confinement Chamber Not Shown)

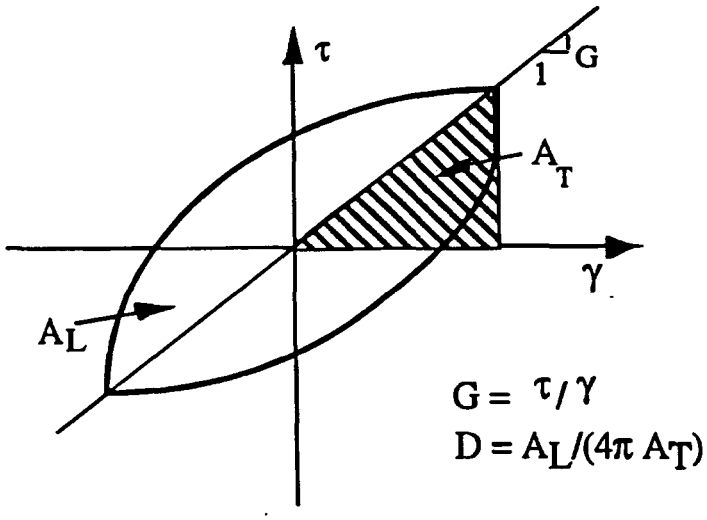

b) Measurement of Shear Modulus and Damping Ratio

Source: PBRCTS-1 Rev 4 (page 5)

Figure 105. (a) Configuration of a Torsional Shear Test and (b) Evaluation of Shear Modulus (G) and Material Damping Ratio (D)

Method of Analysis in the Resonant Column Test

The resonant column test is based on the one-dimensional wave equation derived from the theory of elasticity. The shear modulus is obtained by measuring the first-mode resonant frequency while material damping is evaluated from either the free-vibration decay curve or the width of the frequency response curve using viscous damping principles.

Shear Modulus

The governing equation of motion for the fixed-free torsional resonant column test is (PBRCTS-1, Rev 4, page 12):

$$\frac{\sum I}{I_o} = \frac{\omega_n \ell}{V_S} \tan\left(\frac{\omega_n \ell}{V_S}\right) \qquad \text{(Eq. 11)}$$

where $\Sigma I = I_s + I_m + \ldots$

I_s = mass moment of inertia of specimens,

I_m = mass moment of inertia of membrane,

I_o = mass moment of inertia of rigid end mass at the top of the specimen,

ℓ = length of the specimen,

V_S = shear-wave velocity of the specimen, and

ω_n = undamped natural circular frequency of the system.

The value of I_o is known from the calibration of the drive plates (Figures 106 and 107). Two individual drive plates (UTACED Number 4 and 5) were used during the testing program. The values of I_s and ℓ are easily determined from the specimen size and weight. Once the first-mode resonant frequency is determined, the shear-wave velocity can be calculated by solving Eq. 11 for ω_n with the resonant circular frequency, ω_r, equal to ω_n.

As noted above and shown on Figure 104b, the resonant circular frequency, ω_r, is measured instead of the undamped natural frequency, ω_n, and ω_r is used to calculate shear-wave velocity. If the damping in the system is zero, ω_n and ω_r are equal. The relationship between ω_r and ω_n is (PBRCTS-1 Rev 4, page 12):

$$\omega_r = \omega_n \sqrt{1 - 2D^2} \qquad \text{(Eq. 12)}$$

where D is the material damping ratio. If the damping in the system is zero, ω_n and ω_r are equal.

A typical damping ratio encountered in the resonant column test is less than 20 percent, which corresponds to a difference of less than 5 percent between ω_r and ω_n. In this study, the damping measured in the resonant column test was usually less than 10 percent, and ω_r can be used instead of ω_n with less than a two-percent error.

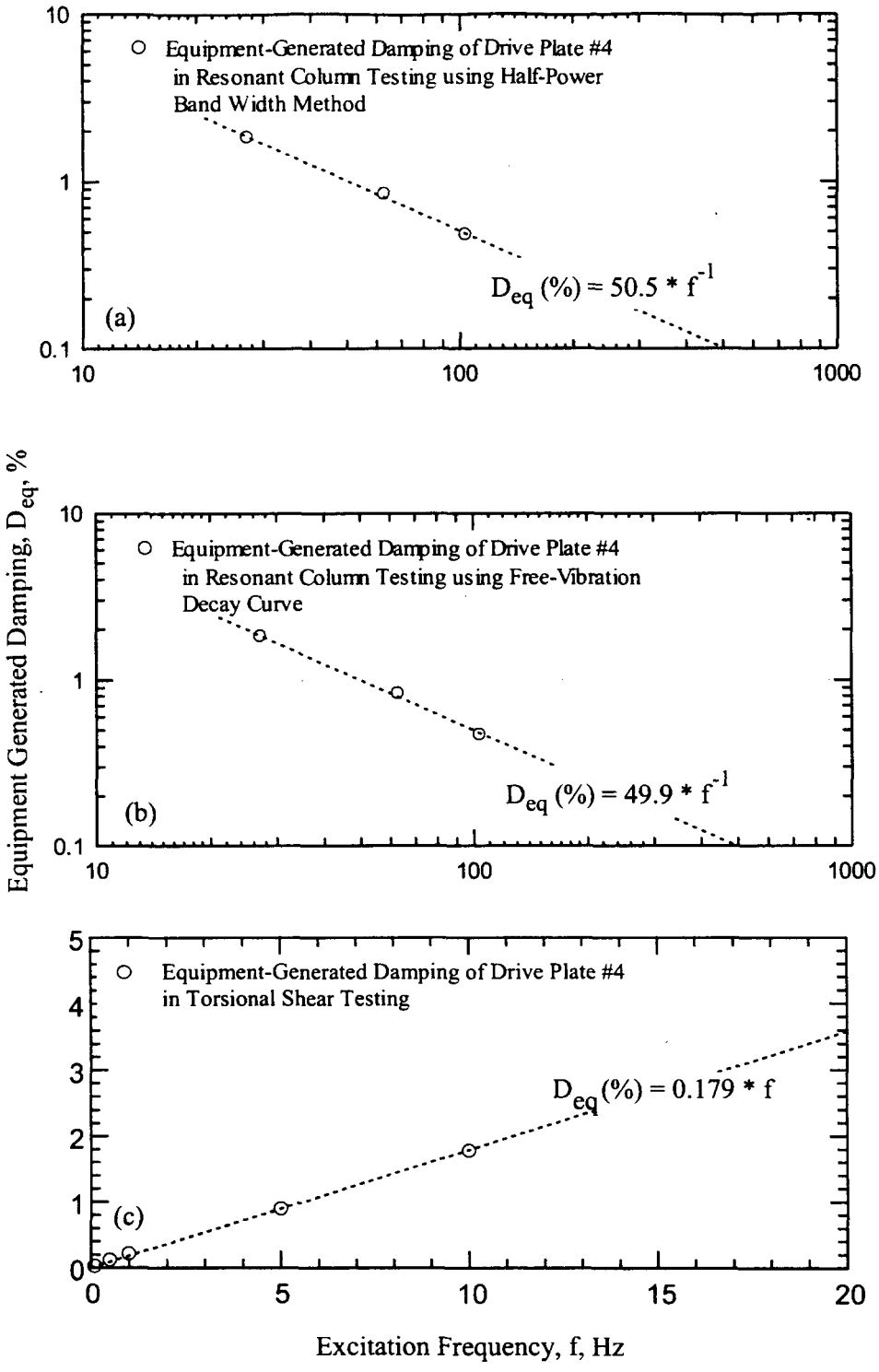

Source: Wong (2002e, Appendix 42, p. 25)

Figure 106. Calibration Curves of Equipment-Generated Damping for Drive Plate #4

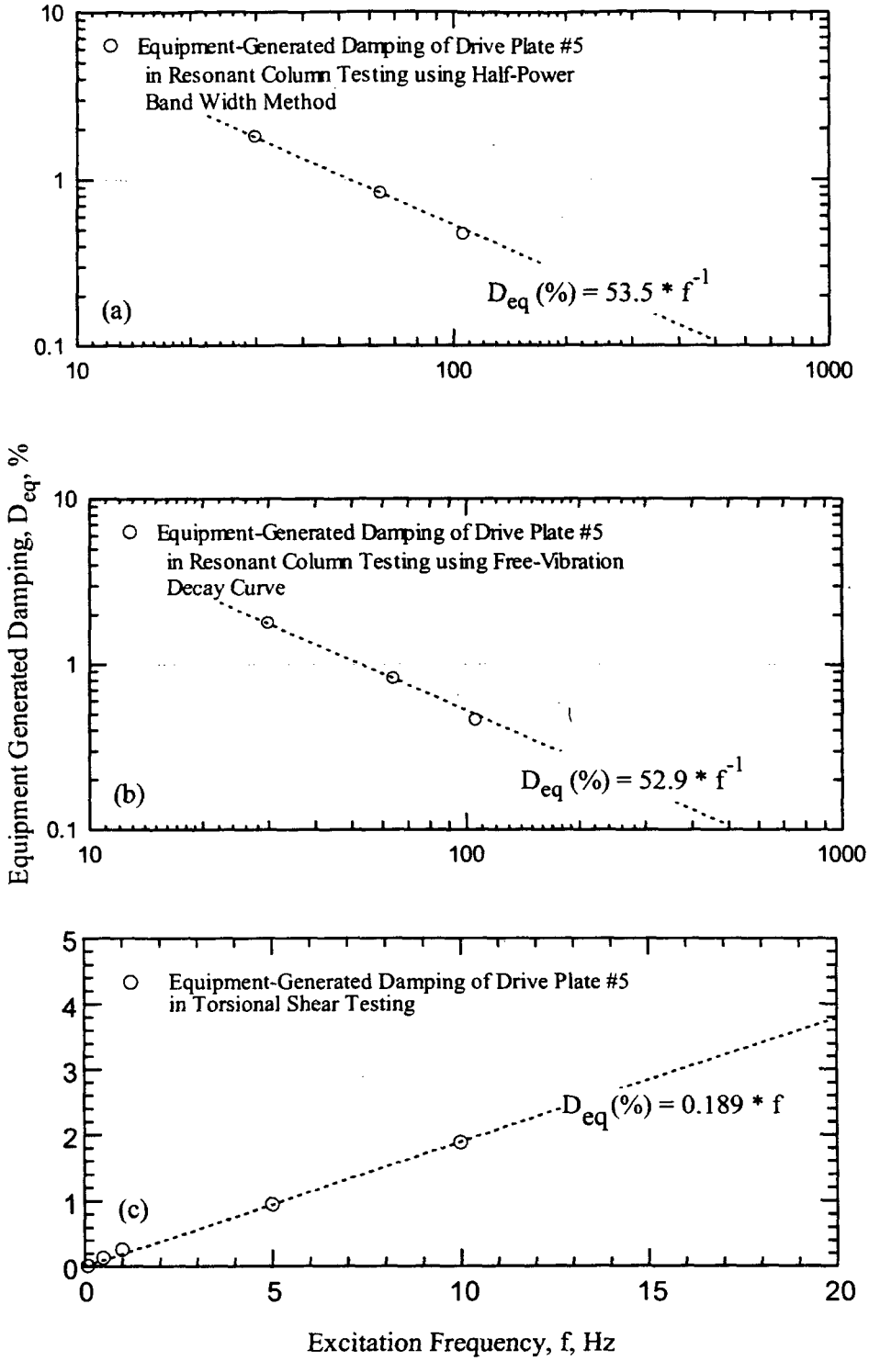

(Wong 2002e, Appendix 42, p. 26)

Figure 107. Calibration Curves of Equipment-Generated Damping for Drive Plate #5

Once the shear-wave velocity is determined, shear modulus is calculated from the relationship (PBRCTS-1 Rev 4, page 13):

$$G = \rho V_S^2 \qquad \text{(Eq. 13)}$$

where ρ is the total mass density of the specimen (total unit weight divided by gravity).

Shearing Strain

The shearing strain varies radially within the specimen and may be expressed as a function of the distance from the longitudinal axis as illustrated on Figure 108. The equivalent shearing strain, γ_{eq} or γ, is represented by (PBRCTS-1 Rev 4, page 13):

$$\gamma = r_{eq}\, \theta_{max} / \ell \qquad \text{(Eq. 14)}$$

where r_{eq} = equivalent radius,

θ_{max} = angle of twist at the top of the specimen, and

ℓ = length of the specimen.

Chen and Stokoe (1979) studied the radial distribution in shearing strain to find a value of r_{eq} for the specimen tested in the RCTS equipment to evaluate an effective strain. They found that the value of r_{eq} for a solid specimen varied from $0.82r_o$ for a peak shearing strain amplitude below 0.001% (Chen and Stokoe 1979, page 41) to $0.79r_o$ for a peak shearing strain of 0.1% (Chen and Stokoe 1979, page 21), where r_o is the initial specimen radius. These values of r_{eq} have been adopted in this study.

In the resonant column test, the resonant period (T_r, seconds), and output voltage of accelerometer (A_c, volts (RMS)) at resonance are measured. Accelerometer output is changed to displacement by using the accelerometer calibration factor (CF, volts (RMS)/in/sec^2) and using the principles of harmonic motion. The accelerometer displacement is divided by the distance (D_{ac}, inches) between the location of accelerometer and the axis of the specimen to calculate the angle of twist at the top of the specimen (θ_{max}). The shearing strain is then calculated by Eq. 15 (PBRCTS-1 Rev 4, page 13):

$$\gamma = r_{eq} \frac{A_c T_r^2}{4\pi^2 CF} \frac{1}{D_{ac}} \frac{1}{\ell} \qquad \text{(Eq. 15)}$$

Material Damping

In the resonant column test, the material damping ratio can be evaluated from either the free-vibration decay method or from the half-power bandwidth method (PBRCTS-1 Rev 4, pages 13-17). Each of these methods is discussed below. It is important to note that, in these measurements, the damping measurement includes material damping in the specimen plus any damping in the equipment.

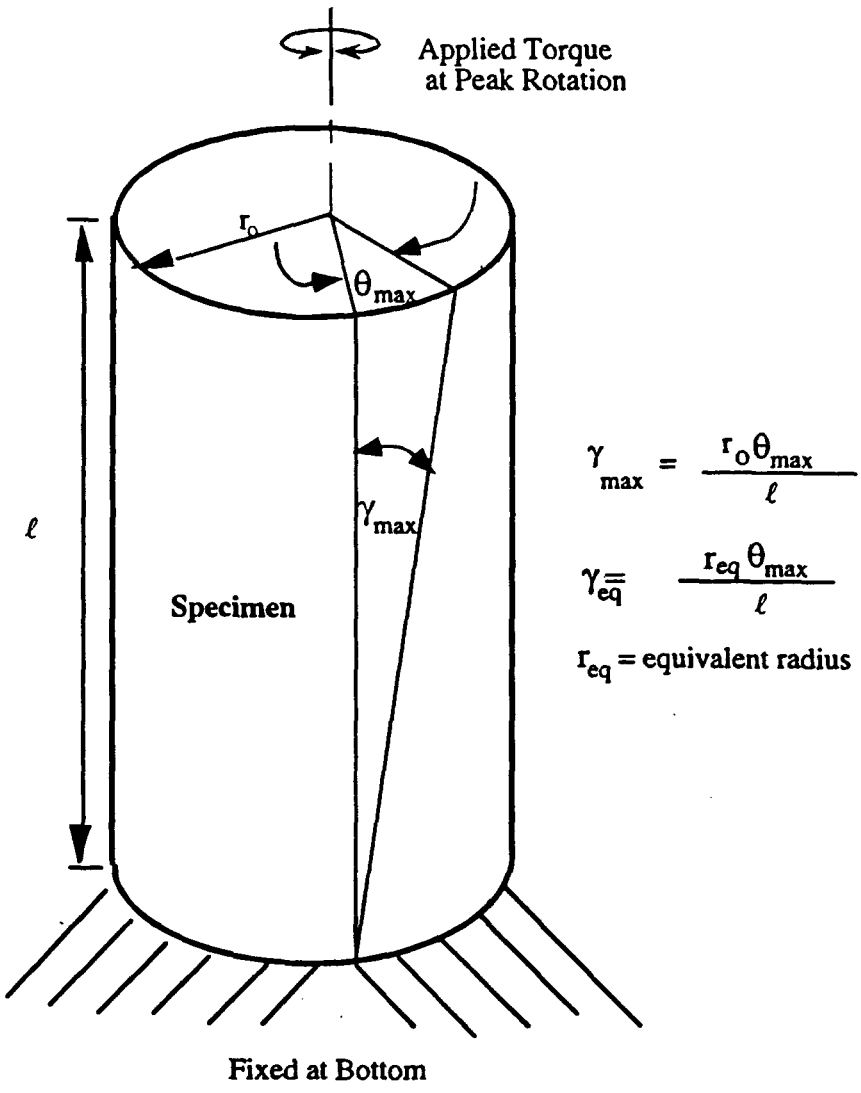

Source: PBRCTS-1 Rev 4 (page 14)

Figure 108. Shearing Strain in RCTS Specimen Column

Free-Vibration Decay Method – Material damping in soil and rock specimens can be quite complex to define. However, the theory for a single-degree-of-freedom system with viscous damping is an appropriate framework for describing the effect of damping that occurs in soil (Richart et al. 1970, page 15). The decay of free vibrations of a single-degree-of-freedom system with viscous damping is described by the logarithmic decrement, δ, which is the ratio of the natural logarithm of two successive amplitudes of motion (PBRCTS-1 Rev 4, page 15):

$$\delta = \ln\left(\frac{Z_1}{Z_2}\right) = \frac{2\pi D}{\sqrt{1-D^2}} \qquad \text{(Eq. 16)}$$

where Z_1 and Z_2 = two successive strain amplitudes of motion, and

D = material damping ratio.

The free-vibration decay curve is recorded using an oscilloscope by shutting off the driving force while the specimen is vibrating at the resonant frequency. The amplitude of each cycle is measured from the decay curve, and the logarithmic decrement is then calculated using Eq. 16. The material damping ratio is calculated from the logarithmic decrement according to:

$$D = \sqrt{\frac{\delta^2}{4\pi^2 + \delta^2}} \qquad \text{(Eq. 17)}$$

A typical damping measurement from a free-vibration decay curve (from a metal calibration specimen) is shown on Figure 109.

In this method, the selection of which strain amplitude is a representative strain for the damping ratio calculated by Eq. 17 is uncertain because strain amplitude decreases during free-vibration decay. In this study, a representative strain amplitude was selected as the peak strain amplitude during steady-state vibration for shearing strains below 0.001%. However, at larger strains, the representative strain is smaller than the peak strain, and the average strain determined for the first three cycles of free vibration was selected as the representative strain amplitude.

Half-Power Bandwidth Method – Another method of measuring damping in the resonant column test is the half-power bandwidth method, which is based on measurement of the width of the frequency response curve near resonance. From the frequency response curve, the logarithmic decrement can be calculated from (PBRCTS-1 Rev 4, page 15):

$$\delta = \frac{\pi}{2} \frac{f_2^{\,2} - f_1^{\,2}}{f_r^{\,2}} \sqrt{\frac{A^2}{A_{max}^{\,2} - A^2}} \frac{\sqrt{1 - 2D^2}}{1 - D^2} \qquad \text{(Eq. 18)}$$

where A_{max} = maximum strain amplitude or strain amplitude at resonance,

f_1 = frequency below the resonance where the strain amplitude is A,

f_2 = frequency above the resonance where the strain amplitude is A,

f_r = resonant frequency, and

D = material damping ratio.

If the damping ratio is small and A is chosen as $\sqrt{2}\, A_{max}/2$, which is called the half-power point, Eq. 18 can be simplified as:

$$\delta \cong \pi \frac{f_2 - f_1}{f_r} \qquad \text{(Eq. 19)}$$

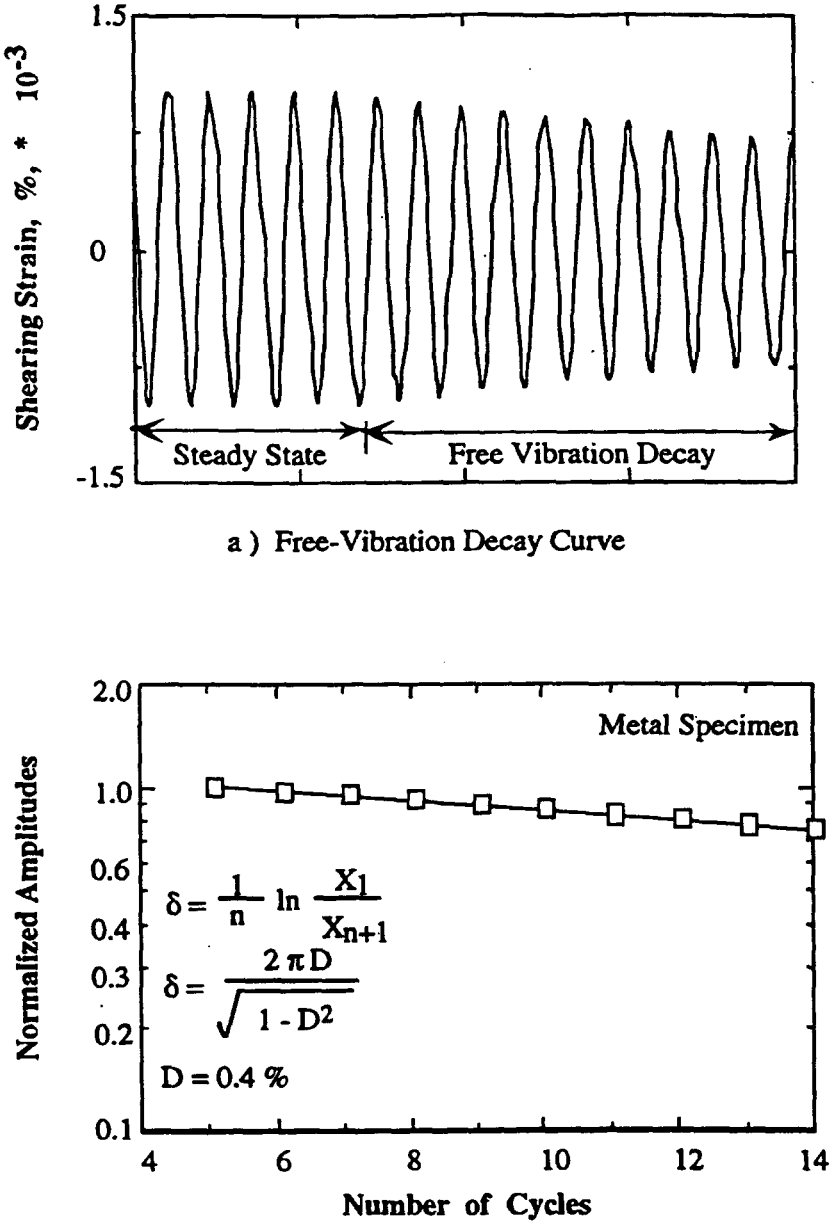

Source: PBRCTS-1 Rev 4 (page 16)

Figure 109. Determination of Material Damping Ratio from the Free-Vibration Decay Curve Using Metal Specimen

Therefore, the damping ratio can be expressed as:

$$D \cong \frac{f_2 - f_1}{2f_r} \qquad \text{(Eq. 20)}$$

A typical damping measurement by the half-power bandwidth method (for a metal calibration specimen) is shown on Figure 110.

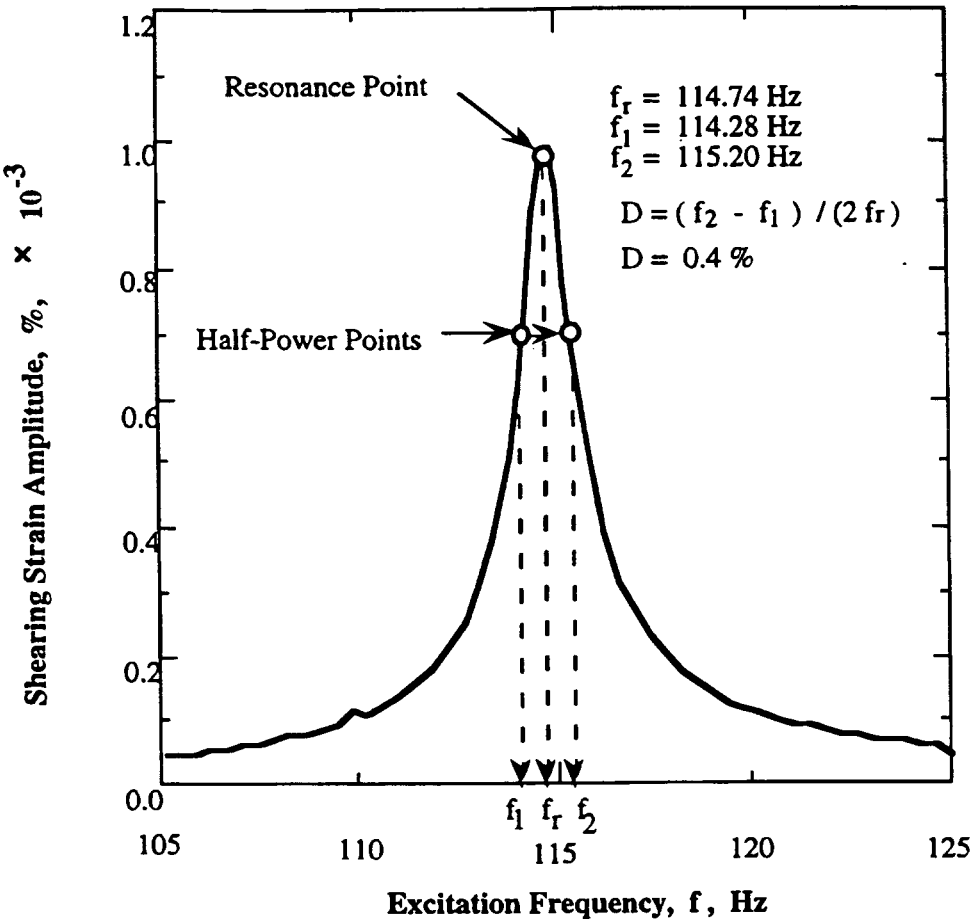

Source: PBRCTS-1 Rev 4 (page 18)

Figure 110. Determination of Material Damping from the Half-Power Bandwidth Method Using a Metal Specimen

Background noise can be a problem in measuring material damping using the free-vibration decay method at strains less than about 0.001%. On the other hand, background noise generally has a smaller effect on the frequency response curve at strains below 0.001%. Therefore, the half-power bandwidth method is preferred to the free-vibration decay method for making small-strain damping measurements. However, at large strains, symmetry in the frequency response curve is no longer maintained, and a serious error can be introduced in the half-power

bandwidth method. In this study, both types of damping measurements were made at small strains in an attempt to obtain good data sets, while only the free-vibration decay method was used at larger strains (above 0.001%).

Method of Analysis in the Torsional Shear Test

The torsional shear test is another method of determining the deformational characteristics (modulus and damping) of soil or rock specimens using the same RCTS device (PBRCTS-1 Rev 4, pages 17-20). Rather than measuring the dynamic response of the specimen, the actual stress-strain hysteresis loop is determined by means of measuring the torque-twist curve. Shear modulus is calculated from the slope of the hysteresis loop, and the hysteretic damping ratio is calculated using the area of the hysteresis loop.

Shear Modulus

Because shear modulus is calculated from the stress-strain hysteresis loop, shearing stress and shearing strain in the torsional shear test need to be defined.

Shearing Stress – Determination of shearing stress in the torsional shear test is based on the theory of elasticity for circular or tubular rods in pure torsion. For the case where pure torque, T, is applied to the top of the specimen, the torque can be calculated from:

$$T = \int_{r_i}^{r_o} \tau_r (2\pi r) r \, dr \qquad \text{(Eq. 21)}$$

where τ_r is the shearing stress at a distance r from the axis of specimen and, r_o and r_i are outside and inside radii, respectively. For a shearing stress that varies linearly across the radius:

$$\tau_r = \tau_m \, (r / r_o) \qquad \text{(Eq. 22)}$$

where τ_m is the maximum shearing stress at $r = r_o$.

Substituting Eq. 22 into Eq. 21 and integrating yields:

$$T = \frac{\tau_m}{r_o} \frac{\pi}{2} (r_o^4 - r_i^4) = \frac{\tau_m}{r_o} J_p \qquad \text{(Eq. 23)}$$

where J_p is the area polar moment of inertia. From Eq. 23, one can write:

$$\tau_m = r_o \frac{T}{J_p} \qquad \text{(Eq. 24)}$$

For the shearing stress varying linearly across the radius, the average torsional shearing stress is defined as:

$$\tau_{avg} = r_{eq} \frac{T}{J_p} \qquad \text{(Eq. 25)}$$

The value of r_{eq} is the same value as used in the resonant column analysis for calculation of shearing strain.

The value of applied torque, T, is calculated from the input voltage applied to the drive system, V_T (volts), and the torque calibration factor, K_T (torque/volts). Thus, average shearing stress is:

$$\tau_{avg} = r_{eq} K_T V_T / J_P \qquad \text{(Eq. 26)}$$

Shearing Strain – Calculation of shearing strain in the torsional shear test follows the same procedure used in the resonant column test. The proximitor system directly measures the displacement (instead of the acceleration measured in the resonant column test). Hence, the angle of twist (θ) is calculated from the proximitor output voltage V_P (volts), and the proximitor calibration factor, K_P (rad/volt). Shearing strain, γ, is then calculated from:

$$\gamma = r_{eq} \sum K_P V_P / \ell \qquad \text{(Eq. 27)}$$

Shear Modulus – Once the stress-strain hysteresis loop is measured, the shear modulus, G, is calculated from the slope of a line through the end points of the hysteresis loop, as shown on Figure 111.

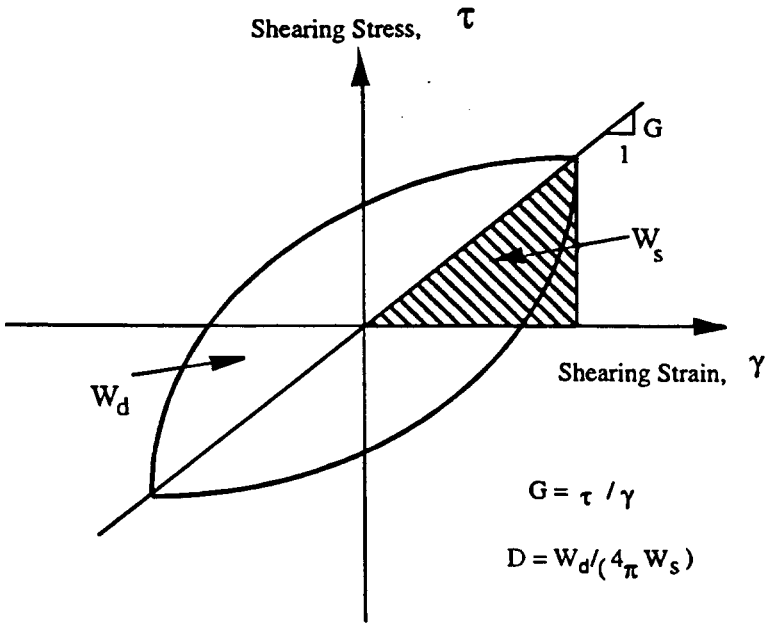

Source: PBRCTS-1 Rev 4 (page 20)

Figure 111. Determination of Shear Modulus and Damping Ratio in the Torsional Shear Test

Thus, the shear modulus is calculated from:

$$G = \tau / \gamma \qquad \text{(Eq. 28)}$$

where τ is peak shearing stress and γ is peak shearing strain.

Hysteretic Damping Ratio

Hysteretic damping ratio in the torsional shear test is measured using the amount of energy dissipated in one complete cycle of loading and the peak strain energy stored in the specimen during the cycle.

In the torsional shear test, the dissipated energy is measured from the area of the stress-strain hysteresis loop. The energy per cycle, W_d, due to a viscous damping force, F_d, is:

$$W_d = \int_o^T F_d \dot{x}\, dt \qquad \text{(Eq. 29)}$$

where $\dot{x}$ is a velocity and T is a period. For simple harmonic motion with frequency ω, i.e., $x = A\cos(\omega t - \phi)$, W_d becomes:

$$W_d = \pi C \omega A^2 \qquad \text{(Eq. 30)}$$

where the constant of integration, C, is referred to as the viscous damping coefficient. From the Eq. 30, the viscous damping coefficient can be expressed as:

$$C = W_d / (\pi \omega A^2) \qquad \text{(Eq. 31)}$$

The peak strain energy, W_s, stored by the spring is equal to the area under the secant modulus line on Figure 109 and can be written as:

$$W_s = k A^2 / 2 \qquad \text{(Eq. 32)}$$

The critical damping coefficient, C_c, is:

$$C_c = 2\sqrt{k m} = 2k / \omega_n \qquad \text{(Eq. 33)}$$

where k is an elastic spring constant, m is a mass, and ω_n is a natural frequency of a system. Solving Eq. 32 for k and substituting the resulting expression into Eq. 33 yields:

$$C_c = \frac{4 W_s}{\omega_n A^2} \qquad \text{(Eq. 34)}$$

Therefore, the damping ratio, D, can be expressed as:

$$D \equiv \frac{C}{C_c} = \frac{W_d}{4\pi W_s}\frac{\omega_n}{\omega} \qquad \text{(Eq. 35)}$$

For soil or rock materials, damping is commonly taken as being frequency-independent. Therefore, ω_n / ω is ignored and hysteretic damping is written as:

$$D = \frac{W_d}{4\pi W_s} \qquad \text{(Eq. 36)}$$

where W_d is the area of the hysteresis loop and W_s is the area of the triangle, as shown on Figure 109.

6.2.10.2 Measurements

Rock specimens were selected to represent the range of tuff types present. However, core samples had to be of sufficient size and quality to be tested. Individual intact core samples could not contain fractures, xenocrysts, or lithophysae larger than 0.5 centimeters in diameter, which would cause the specimen to fail prematurely during testing. Also, several attempts were made to obtain intact alluvial specimens without success. The material failed during the sampling process. Only one alluvial sample (not intact) was collected. Additional alluvial samples were not collected because reconstituted alluvial specimens are not as representative of in-situ conditions and previous reconstituted alluvial samples had been tested (CRWMS M&O 1999b, Appendix Q; DTN: MO9905LABDYNRS.000). All specimens were shipped as core samples from the Sample Management Facility (SMF) to the Geotechnical Engineering Center at the University of Texas at Austin. All core samples were contained in cardboard shipping containers, with each core individually wrapped in plastic and surrounded by packing material.

Of the 19 specimens, 18 were intact tuff specimens and one was a alluvial specimen. Fourteen of the tuff specimens were derived by carefully wet-coring specimens with a nominal diameter of 3.97 cm (1.56 inches) from each larger-diameter core sample. The ends of the cylindrical specimens were trimmed with a rock saw so that the specimens had the shape of a right circular cylinder. The remaining 4 tuff specimens were wet cored from 4 of the above 14 tested specimens. In this case, the re-tested, smaller tuff specimens had a nominal diameter of 2.11 cm (0.83 inches). The one alluvial specimen was reconstituted in the laboratory because this material was disturbed upon sampling in the field and could not be tested intact. The alluvial specimen was reconstituted using the standard under-compaction method by Ladd (1978).

The initial properties of the 18 intact tuff specimens are presented in Tables 14 to 16. Photographs of the specimens are presented on Figures 112 to 114. As shown in Tables 14 to 16, the 14 tuff specimens with a nominal diameter of 3.97 cm (1.56 inches) have heights that ranged from about 2 to 2.5 times the diameter. The 4 tuff specimens with a nominal diameter of 2.11 cm (0.83 inches) have heights that ranged from about 2.2 to 4.8 times the diameter. These 18 tuff specimens are divided into three groups based on their dry unit weight, γ_d: Group 1: γ_d from 133 pcf to 147 pcf; Group 2: γ_d from 117 pcf to 132 pcf; and Group 3: γ_d from 78 pcf to 94 pcf. This grouping was chosen because of the relationship between V_s and dry unit weight (see further discussion in this section).

INTENTIONALLY LEFT BLANK

Table 14. Initial Properties of Intact Tuff Specimens with a Dry Unit Weight Between 133 pcf and 147 pcf from WHB Boreholes (Group 1)

UTACED[a] Designation	SMF Designation	Borehole	Depth (ft)	Stratigraphic Unit	Height[c] (cm)	Diameter[c] (cm)	Mass[c] (g)	Water Content[c] (%)	Dry Unit Weight (pcf)	Total Unit Weight[c] (pcf)
UTA-23-C	01012518	RF#14	361.0	Tpcpul	11.38	3.98	305.1	0.65	133.5	134.4
UTA-23-D	01012519	RF#14	397.0	Tpcpmn	11.26	3.97	329.1	1.00	146.0	147.5
UTA-23-G	01012525	RF#15	192.5	Tpcpul	11.12	3.95	317.9	0.43	144.9	145.5
UTA-23-T[b]	01012525	RF#15	192.5	Tpcpul	10.30	2.15	87.0	0.43	144.5	145.1
UTA-23-H	01012527	RF#15	322.0	Tpcpln	11.53	3.96	332.9	0.53	145.4	146.2
UTA-23-J	01012538	RF#17	575.6	Tpcpul	10.98	3.96	304.8	0.27	140.2	140.6

Sources: DTN: MO0203DHRSSWHB.001, [c] Wong (2002e, Appendix 42, page 12)

Notes: [a] UTACED means University of Texas at Austin, Civil Engineering Department
[b] UTA-23-T was cored from UTA-23-G after RCTS testing was completed

Table 15. Initial Properties of Intact Tuff Specimens with a Dry Unit Weight between 117 pcf and 132 pcf from WHB Boreholes (Group 2)

UTACED[a] Designation	SMF Designation	Borehole	Depth (ft)	Stratigraphic Unit	Height[d] (cm)	Diameter[d] (cm)	Mass[d] (g)	Water Content[d] (%)	Dry Unit Weight (pcf)	Total Unit Weight[d] (pcf)
UTA-20-B	01012372	RF#16	189.5	Tpcrn	11.46	3.97	275.1	0.38	120.9	121.4
UTA-20-C	01012373	RF#16	235.5	Tpcpul	10.22	3.96	258.4	2.30	125.3	128.1
UTA-23-B	01012516	RF#14	241.5	Tpcrn	11.18	3.96	278.6	1.54	124.5	126.4
UTA-23-R[b]	01012516	RF#14	241.5	Tpcrn	5.75	2.11	38.7	1.50	118.2	120.0
UTA-23-E	01012520	RF#15	27.3	Tpcrn	11.70	3.96	273.6	1.02	117.2	118.4
UTA-23-F	01012522	RF#15	88.7	Tpcpul	11.45	3.98	302.7	0.68	131.5	132.4
UTA-23-S[c]	01012522	RF#15	88.7	Tpcpul	10.66	2.03	73.8	4.55	127.4	133.2

Sources: DTN: MO0203DHRSSWHB.001, [d] Wong (2002e, Appendix 42, page 13)

Notes: [a] UTACED means University of Texas at Austin, Civil Engineering Department
[b] UTA-23-R was cored from UTA-23-B after RCTS testing was completed
[c] UTA-23-S was cored from UTA-23-F after RCTS testing was completed

Table 16. Initial Properties of Intact Tuff Specimens with a Dry Unit Weight between 78 pcf and 94 pcf from WHB Boreholes (Group 3)

UTACED[a] Designation	SMF Designation	Borehole	Depth (ft)	Stratigraphic Unit	Height[c] (cm)	Diameter[c] (cm)	Mass[c] (g)	Water Content[c] (%)	Dry Unit Weight (pcf)	Total Unit Weight[c] (pcf)
UTA-20-A	01012371	RF#16	126.8	Tpki	11.56	3.96	201.2	9.28	80.8	88.3
UTA-23-Q[b]	01012371	RF#16	126.8	Tpki	4.73	2.10	21.7	5.10	78.8	82.8
UTA-20-D	01012370	RF#16	80.5	Tpki	11.47	3.97	225.4	8.30	91.5	99.1
UTA-23-A	01012512	RF#14	104.5	Tpki	10.95	3.94	209.4	4.82	93.5	98.0
UTA-23-I	01012535	RF#17	400.2	Tpcrn	10.67	3.96	181.4	0.32	86.0	86.2

Sources: DTN: MO0203DHRSSWHB.001, [c] Wong (2002e, Appendix 42, page 14)

Notes: [a] UTACED means University of Texas at Austin, Civil Engineering Department
[b] UTA-23-Q was cored from UTA-23-A after RCTS testing was completed

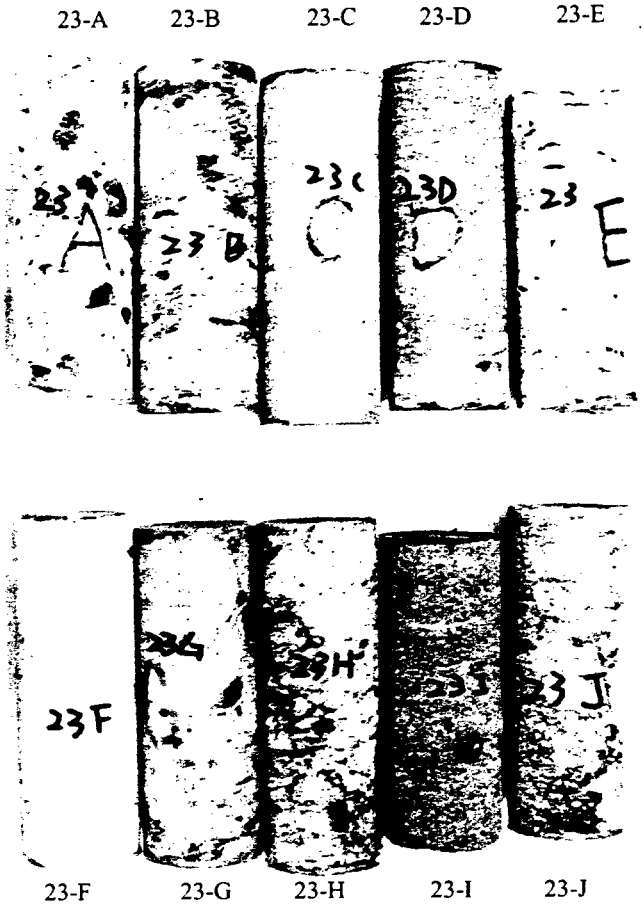

Source: Modified from Wong (2002e, Appendix 42, page 60)

Figure 112. Specimens UTA-23-A to 23-J

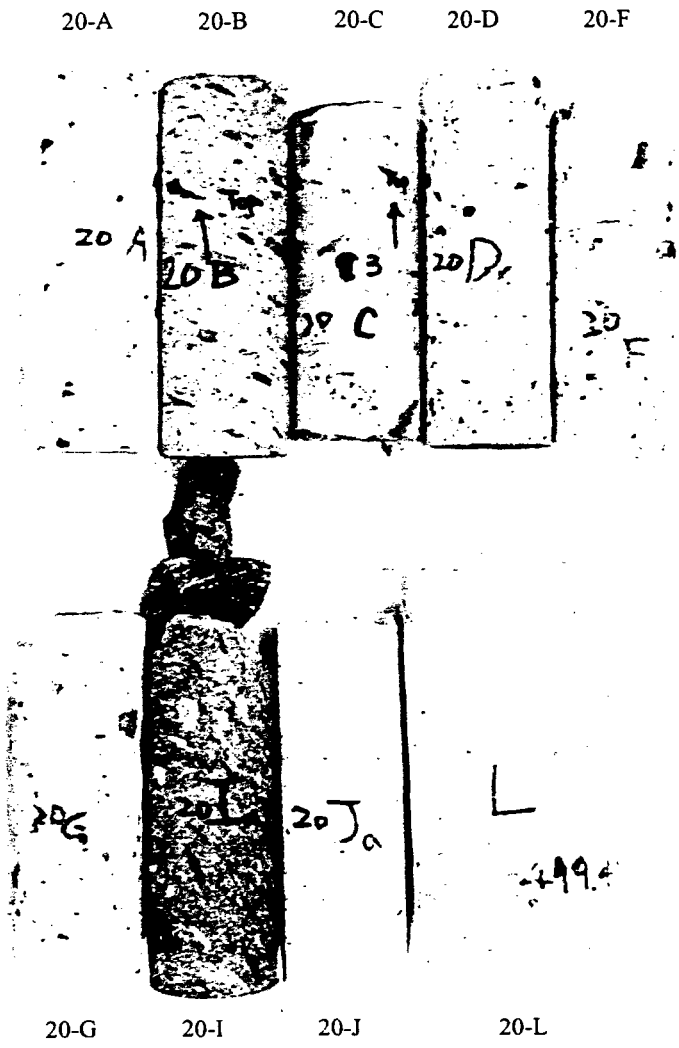

Source: Modified from Wong (2002e, Appendix 42, page 61)

Figure 113. UTA-20 Group: Specimens 20-A, 20-B, 20-C, and 20-D are from the WHB Boreholes. Specimens 20-F, 20-G, 20-I, 20-J, and 20-L are from the ESF (Section 6.3.3)

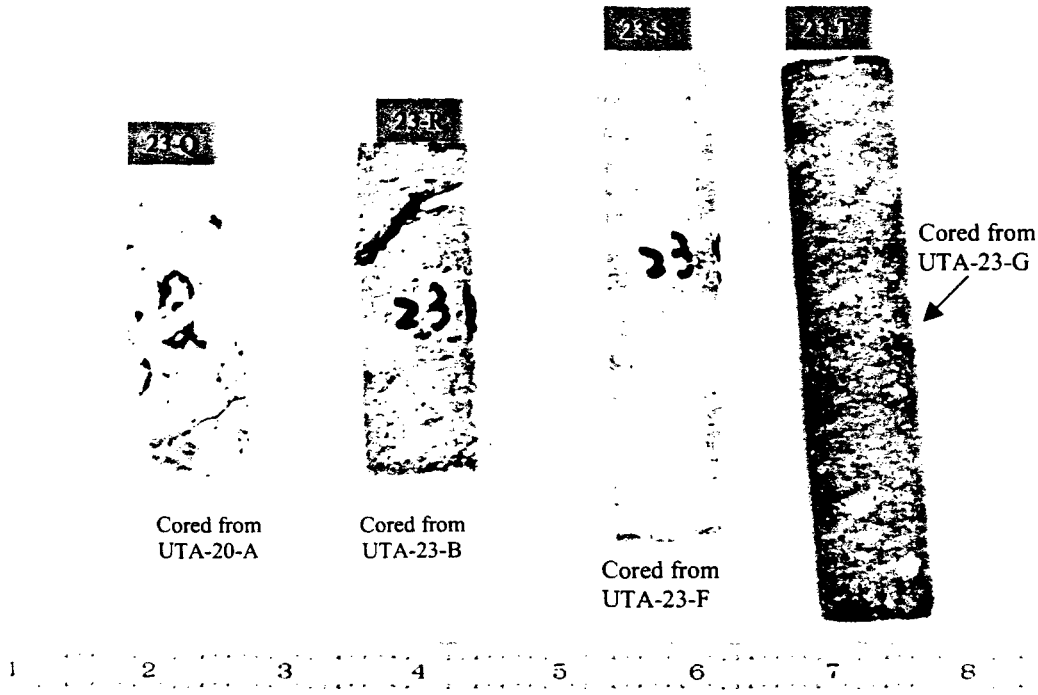

Source: Modified from Wong (2002e, Appendix 42, page 62)

Figure 114. Specimens UTA-23-Q, UTA-23-R, UTA-23-S, and UTA-23-T, which were Cored from Larger Test Specimens

The initial properties of the reconstituted alluvial specimen are presented in Table 17. The alluvial specimen had a diameter of 6.96 cm and a height just slightly larger than 2 times the diameter. The 19 specimens were generally observed to contain some moisture and the water contents measured in the laboratory ranged from 0.27 to 9.28 % for the tuff specimens and 18.04% for the alluvial specimen (Tables 14 to 17). The water contents of the specimens are not representative of in-situ conditions due to the use of drilling mud in the borehole drilling.

RCTS testing was performed on each specimen. All testing was conducted in accordance with either Nevada Work Instruction NWI-SPO-004Q, *Laboratory Dynamic Rock/Soil Testing*, or Line Procedure LP-GEO-002Q-BSC, *Laboratory Dynamic Rock/Soil Testing*. LP-GEO-002Q-BSC superceded NW1-SPO-004Q during the testing program. The equipment, software, data collection procedures and data reduction procedures are given in PBRCTS-1, Rev. 4, which is contained in Appendix 1 of Scientific Notebook SN-M&O-SCI-033-V1 (Wong 2002e). The resonant column testing was conducted with software RCTEST Version 2.1. The torsional shear testing was conducted with software TSTEST Version 3.1. Table 18 lists the test pressures and types of tests performed on the specimens.

Table 17. Initial Properties of Reconstituted Alluvial Specimen

UTACED Designation	SMF Designation	Borehole	Depth (ft)	Stratigraphic Unit	Height[a] (cm)	Diameter[a] (cm)	Mass[a] (g)	Water Content[a] (%)	Dry Unit Weight (pcf)	Total Unit Weight[a] (pcf)
UTA-23-X	01012646	RF#17	59.0	Qal	14.10	6.96	924.3	18.04	91.1	107.5

Sources: DTN: MO0203DHRSSWHB.001, [a] Wong (2002e, Appendix 42, page 15)

Table 18. Confining Pressures at Which RCTS Tests were Performed on Intact Tuff and Reconstituted Qal Specimens from WHB Boreholes

UTACED Designation	SMF Designation	Borehole	Depth (ft)	Stratigraphic Unit	Estimated Mean Total Stress (psi)	Low-Amplitude RC Test Pressures (psi)	High-Amplitude RC Test Pressures (psi)	Low- and High-Amplitude TS Test Pressures (psi)
UTA-23-C	01012518	RF#14	361.0	Tpcpul	280	0, 70, 140, 280, 450	280, 450	280, 450
UTA-23-D	01012519	RF#14	397.0	Tpcpmn	340	0, 70, 170, 340, 450	340, 450	340, 450
UTA-23-G	01012525	RF#15	192.5	Tpcpul	120	0, 30, 60, 120, 240, 450	120, 450	120, 450
UTA-23-T	01012525	RF#15	192.5	Tpcpul	120	0, 30, 60, 120, 240, 450	120, 450	120, 450
UTA-23-H	01012527	RF#15	322.0	Tpcpln	200	0, 50, 100, 200, 400, 450	200, 450	200, 450
UTA-23-J	01012538	RF#17	575.6	Tpcpul	360	0, 90, 180, 360, 450	360, 450	360, 450
UTA-20-B	01012372	RF#16	189.5	Tpcrn	115	0. 29, 58, 115, 230, 460	115, 460	115, 460
UTA-20-C	01012373	RF#16	235.5	Tpcpul	150	0, 38, 75, 150, 300, 450	150, 450	150, 450
UTA-23-B	01012516	RF#14	241.5	Tpcrn	176	0, 44, 88, 176, 352, 450	176, 450	176, 450
UTA-23-R	01012516	RF#14	241.5	Tpcrn	176	0, 44, 88, 176	176	176
UTA-23-E	01012520	RF#15	27.3	Tpcrn	18	0, 5, 9, 18, 36, 72	18, 72	18, 72
UTA-23-F	01012522	RF#15	88.7	Tpcpul	68	0,17, 34, 68, 136, 272	68, 272	68, 272
UTA-23-S	01012522	RF#15	88.7	Tpcpul	68	0,17, 34, 68, 136, 272	68, 272	68, 272
UTA-20-A	01012371	RF#16	126.8	Tpki	70	0, 18, 35, 70, 140, 280	70, 280	70, 280
UTA-23-Q	01012371	RF#16	126.8	Tpki	70	0, 18, 35, 70	70	70
UTA-20-D	01012370	RF#16	80.5	Tpki	56	0, 14, 28, 56, 110, 220	56, 220	56, 220
UTA-23-A	01012512	RF#14	104.5	Tpki	66	0, 16, 33, 66, 132, 264	66, 264	66, 264
UTA-23-I	01012535	RF#17	400.2	Tpcrn	250	0, 62, 125, 250, 450	250, 450	250, 450
UTA-23-X	01012646	RF#17	59.0	Qal	32	8, 16,32	32	32

Sources: Wong (2002e, Appendix 42, page 18)

The RCTS equipment is described in detail in PBRCTS-1 Rev. 4, including a listing of the equipment model names and serial numbers and a discussion of the testing and analysis methodologies. The measured dynamic properties were shear-wave velocity, shear modulus (G), and the material damping ratio in shear (D). These parameters were evaluated to determine the effect of the following variables:

1) Magnitude of isotropic state of stress (isotropic confining pressure), σ_o. Four to five isotropic pressures that ranged from below to above the estimated in-situ mean total stress were generally used, where the in-situ mean total stress was estimated using an earth pressure coefficient (σ_h/σ_v) of either 0.5 or 0.75, as discussed in Scientific Notebook SN-M&O-SCI-033-V1 (Wong 2002e, page 139).

2) Time of confinement at each isotropic state of stress, *t*. Times at each pressure ranged from 1 hour to 1 day or more.

3) Shearing strain amplitude, γ. Shearing strains ranged from the small-strain range, less than 0.0003% for the tuff specimens and 0.001% for the reconstituted specimen, to medium strain amplitudes, ranging from 0.003% to about 0.1%.

4) Numbers of cycles of loading, N. Ten cycles of loading were used in the torsional shear test followed by about 1000 cycles in the resonant column test.

5) Excitation frequencies (*f*) ranging from 0.1 to about 10 Hz were used in the torsional shear test, while the frequency associated with resonance in the resonant column test varied with stiffness of the specimen and ranged from 21 to 458 Hz.

A summary of the tests performed on the specimens is given in Tables 19 to 22 (note that ksf means kips per square foot). Results from individual tests are plotted on Figures XII-1 to XII-19.

It should also be noted that all material damping values reported herein have been corrected to remove equipment-generated damping, as discussed in PBRCTS-1, Rev. 4. This correction involves subtracting equipment-generated damping, which was determined in the initial calibration phase of this work. The values of equipment-generated damping are shown on Figures 106 and 107 for drive plates #4 and #5, respectively.

Table 19. Fixed-Free, Small-Strain RCTS Test Results of Group 1 Intact Tuff Specimens at Estimated In-Situ Stress State

UTACED Designation	Stratigraphic Unit	Resonant Column			Torsional Shear[a]	
		Vs (ft/s)	Gmax (ksf)	Dmin (%)	Gmax (ksf)	Dmin (%)
UTA-23-C	Tpcpul	7632	276820	1.27	251000	1.36
UTA-23-D	Tpcpmn	7263	243190	0.63	229000	0.44
UTA-23-G	Tpcpul	7426	249540	0.53	232900	0.43
UTA-23-T	Tpcpul	8763	345320	0.21	282900	0.43
UTA-23-H	Tpcpln	7271	240740	1.07	189900	1.11
UTA-23-J	Tpcpul	6987	208720	1.14	185000	1.16

DTN: MO0203DHRSSWHB.001

Note: [a] from tenth loading cycle

Table 20. Fixed-Free, Small-Strain RCTS Test Results of Group 2 Intact Tuff Specimens at Estimated In-Situ Stress State

UTACED Designation	Stratigraphic Unit	Resonant Column			Torsional Shear[a]	
		Vs (ft/s)	Gmax (ksf)	Dmin (%)	Gmax (ksf)	Dmin (%)
UTA-20-B	Tpcrn	5539	115670	0.64	107000	0.66
UTA-20-C	Tpcpul	5251	109810	0.43	100800	0.45
UTA-23-B	Tpcrn	6174	150100	1.30	127600	1.55
UTA-23-R	Tpcrn	6235	145370	0.27	124800	0.27
UTA-23-E	Tpcrn	5024	92275	0.44	80900	0.32
UTA-23-F	Tpcpul	6405	168870	0.34	147500	0.27
UTA-23-S	Tpcpul	7136	210880	0.34	199999	0.24

DTN: MO0203DHRSSWHB.001

Note: [a] from tenth loading cycle

Table 21. Fixed-Free, Small-Strain RCTS Test Results of Group 3 Intact Tuff Specimens at Estimated In-Situ Stress State

UTACED Designation	Stratigraphic Unit	Resonant Column			Torsional Shear[a]	
		Vs (ft/s)	Gmax (ksf)	Dmin (%)	Gmax (ksf)	Dmin (%)
UTA-20-A	Tpki	3419	32094	0.72	30210	0.57
UTA-23-Q	Tpki	3753	36283	1.00	34210	1.00
UTA-20-D	Tpki	4072	51035	0.52	46200	0.52
UTA-23-A	Tpki	4645	65697	0.89	54700	0.91
UTA-23-I	Tpcrn	4560	55766	0.21	53450	0.19

DTN: MO0203DHRSSWHB.001

Note: [a] from tenth loading cycle

Table 22. Fixed-Free, Small-Strain RCTS Test Results of Reconstituted Quaternary Alluvial Specimen

UTACED Designation	Stratigraphic Unit	Resonant Column			Torsional Shear[a]	
		Vs (ft/s)	Gmax (ksf)	Dmin (%)	Gmax (ksf)	Dmin (%)
UTA-23-X	Qal	923	2854	1.04	2499	0.98

DTN: MO0203DHRSSWHB.001

Note: [a] from tenth loading cycle

6.2.10.3 Results

The shear-wave velocities, shear moduli, and material damping values from the RCTS tests are presented in tabular and graphical forms in Attachment XII. In this section, the principal results from these measurements are presented in summary tables and graphs and are briefly discussed.

Small-Strain Behavior of Intact Tuff Specimens

The values of shear-wave velocity (V_s), shear modulus (G_{max}), and material damping ratio (D_{min}) measured at small shearing strains (strains less than 0.0003%) are summarized in Tables 19 to 21 for intact tuff specimens from Groups 1, 2 and 3, respectively. The values presented were measured at the estimated in-situ mean total stress ($\sigma_{in\text{-}situ}$). The in-situ mean total stress was

estimated using an earth pressure coefficient (σ_h/σ_v) of either 0.5 or 0.75, as discussed in Scientific Notebook SN-M&O-SCI-033-V1 (Wong 2002e, page 139). D_{min} and G_{max} in Tables 19-22 are determined by fitting a curve through the data. Four to five isotropic pressures that ranged from below to above the estimated in-situ mean total stress were generally used, where the in-situ mean total stress was estimated using an earth pressure coefficient of either 0.5 or 0.75.

The variations in small-strain shear modulus, G_{max}, with confining pressure, σ, that were measured by resonant column testing are presented in a normalized form (G_{max} at σ_{cell} / G_{max} at $\sigma_{in\text{-}situ}$ versus σ_{cell} / $\sigma_{in\text{-}situ}$) on Figures 115 to 117 for the three groups of tuff specimens. As shown, all intact tuff specimens, except one (UTA-23-C; Figure 115), exhibit only small increases in G_{max} as confining pressure ranges from 0.25 to 4 times σ_{cell} / $\sigma_{in\text{-}situ}$. In fact, the small increases in G_{max} with increasing σ occur mainly at confining pressures less than $\sigma_{in\text{-}situ}$. This behavior is interpreted as the closing of micro-cracks in the specimens in this pressure range.

The variation in V_S measured at $\sigma_{in\text{-}situ}$ with dry unit weight, γ_{dry}, of the tuff specimens is shown on Figure 118. As shown, there is a general trend of increasing V_S with increasing γ_{dry}. This general relationship formed the basis for subdividing the intact tuff specimens into three groups based on dry unit weight. The following general relationships are observed:

Group 1: 8,800 ft/s > V_S > 6,900 ft/s
Group 2: 6,500 ft/s > V_S > 5,000 ft/s
Group 3: 4,700 ft/s > V_S > 3,400 ft/s

The one exception is specimen UTA-23-S in Group 2, which has γ_d = 127.4 pcf and V_S = 7,136 ft/s. This specimen was cored from specimen UTA-23-F and exhibits a shear-wave velocity about 10% greater than the parent specimen. In fact, all four specimens that were cored from larger specimens show slightly higher velocities than the parent specimens (UTA-23-T, UTA-23-R, UTA-23-S, and UTA-23-Q). This difference might be attributed to an increase in micro-cracking (possibly caused by the field sampling process) that increases with radial distance from the center of the original core sample.

The general relationship shown on Figure 118 between dry unit weight and shear-wave velocity is also found between total unit weight and shear-wave velocity, as shown on Figure 119.

The variations in small-strain material damping ratio, D_{min}, with normalized confining pressure (σ_{cell} / $\sigma_{in\text{-}situ}$) that were measured by resonant column testing are shown on Figures 120 to 122 for Groups 1, 2 and 3, respectively. As with G_{max}, D_{min} shows little effect of σ. The values of D_{min} range from about 0.2 to 2.0% at $\sigma_{in\text{-}situ}$ and are not correlated with γ_d as was found with shear-wave velocity (and hence G_{max}).

The effects on G_{max} and D_{min} of the intact tuff specimens of two other parameters were also studied. These parameters are time of confinement at a constant isotropic stress state, *t*, and excitation frequency, *f*. The effect of *t* on G_{max} and D_{min} was inconsequential in these tests (less than a 1% change over the testing time). The effect of *f* was investigated in two ways.

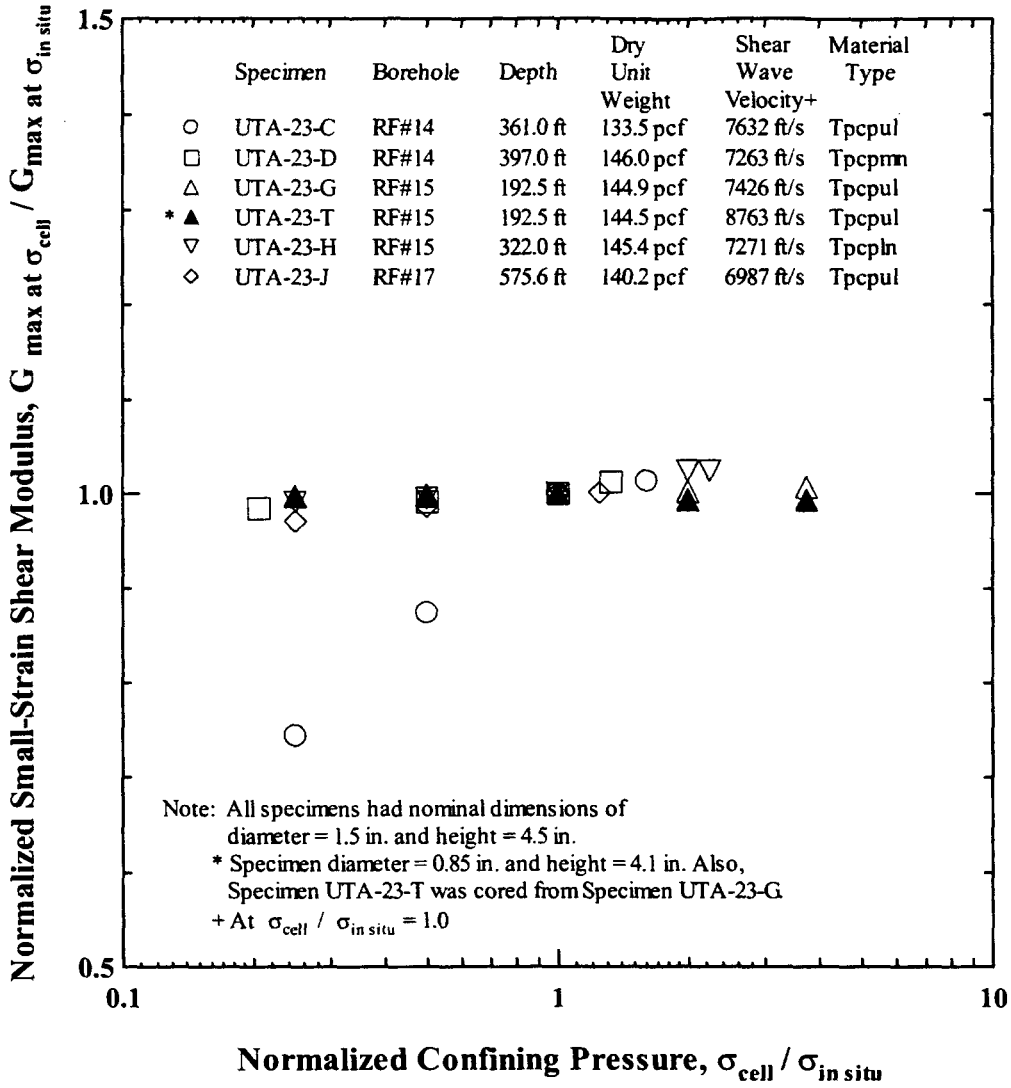

Source: Wong (2002e, Appendix 42, page 27)

Figure 115. *Variation in Normalized Small-Strain Shear Modulus with Normalized Confining Pressure of Group 1 Intact Tuff Specimens*

First, in torsional shear testing at the estimated $\sigma_{in\text{-}situ}$, G_{max} and D_{min} were measured over a frequency range of 0.1 to about 10 Hz. The effect of frequency on G_{max} over this range was very small, less than 2%.

Second, the effect of changing the excitation frequency from 1 Hz in the torsional shear test to the range of several 100 Hz in the resonant column test was evaluated. In this case, G_{max} increased about 11% (ranging from 1 to 27%) for the 18 intact tuff specimens, as can be seen in Tables 19 to 21. (All results over the complete frequency range are shown on Figures XII-20 to XII-25.) G_{max} increased 14% for the reconstituted alluvium specimen (Table 22). This increase can be attributed to both excitation frequency and limitations in each testing technique, as

discussed in Section 6.2.10.4. An average increase in G_{max} of 11% is approximately equivalent to a 5.4% increase in shear-wave velocity over this frequency range. This variation in values is considered small and within the range of typical variability to be expected in such measurements.

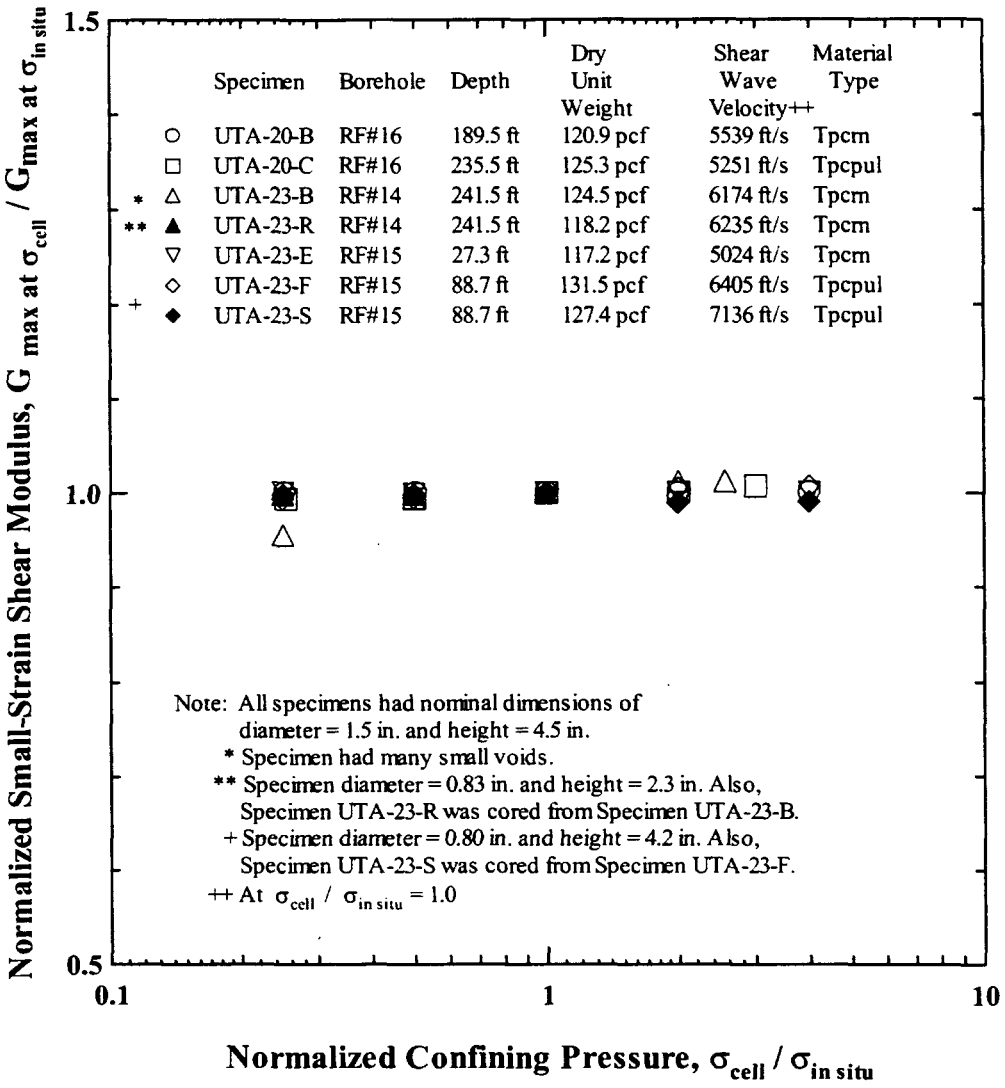

Source: Modified from Wong (2002e, Appendix 42, page 28)

Figure 116. Variation in Normalized Small-Strain Shear Modulus with Normalized Confining Pressure of Group 2 Intact Tuff Specimens

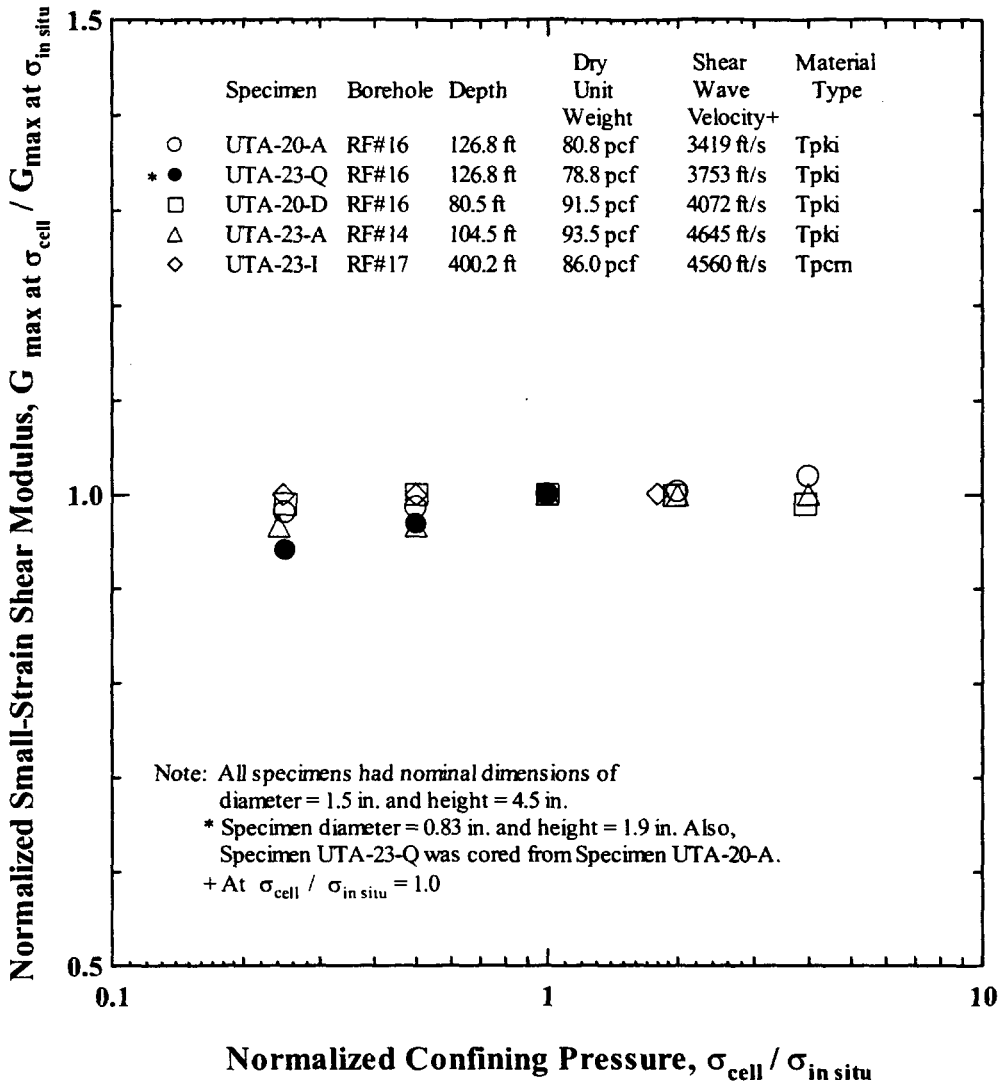

Source: Modified from Wong (2002e, Appendix 42, page 29)

Figure 117. Variation in Normalized Small-Strain Shear Modulus with Normalized Confining Pressure of Group 3 Intact Tuff Specimens

Nonlinear Behavior of Intact Tuff Specimens

The influence of shearing strain, γ, on G as measured by resonant column testing is shown on Figures 123 to 125 for the intact tuff specimens in Groups 1, 2 and 3, respectively. The influence of γ on normalized shear modulus, G/G_{max} is presented for the same groups on Figures 126 to 128, respectively. Typical nonlinear curves proposed for sands by Seed et al. (1986, Figure 2) are also shown on Figures 126 to 128 for comparison purposes. As shown, the intact tuff specimens exhibited only a small amount of nonlinearity at γ = 0.01%, with G/G_{max} generally greater than 0.9. However, two of the small-diameter specimens (UTA-23-R and UTA-23-Q) failed at γ around 0.1%.

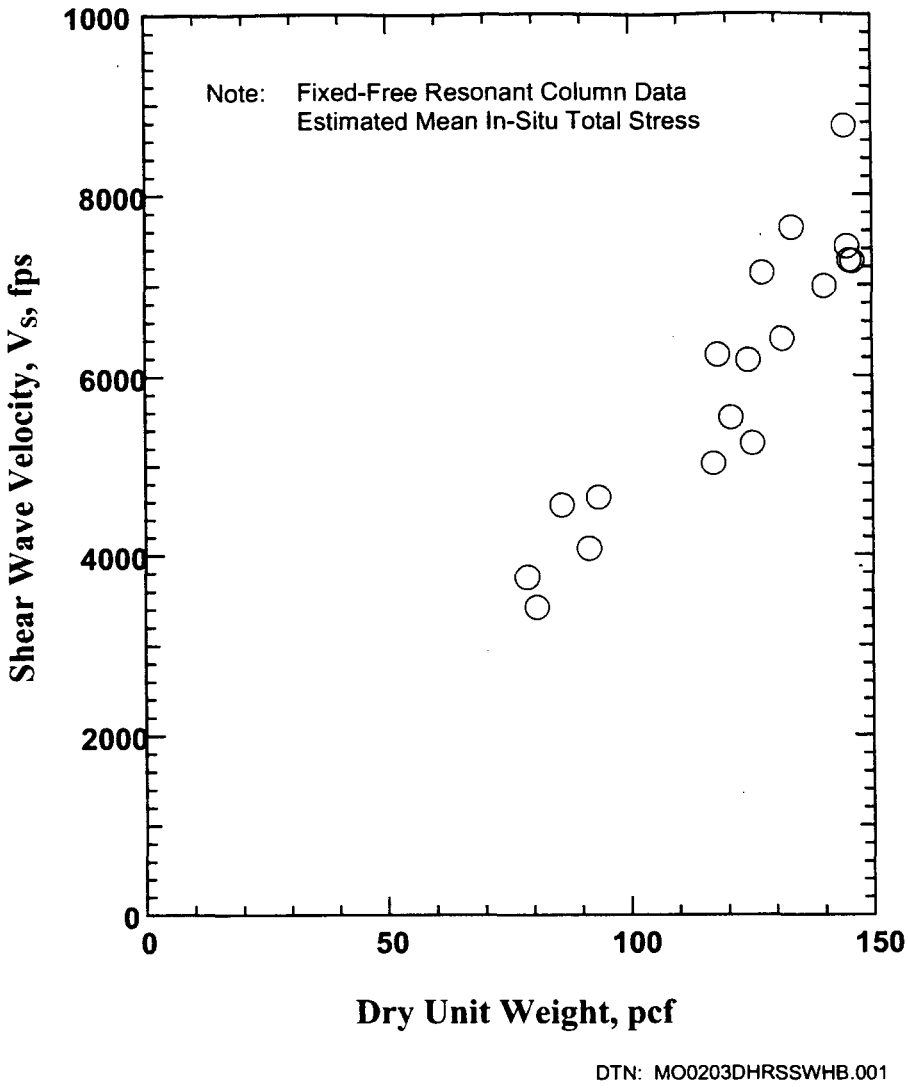

Figure 118. Variation of Shear-Wave Velocity Measured in the Laboratory at In-Situ Mean Total Stress with Dry Unit Weight of Intact Tuff Specimens

The influence of shearing strain on D as measured by resonant column testing is shown on Figures 129 to 131 for the tuff specimens in Groups 1, 2 and 3, respectively. In general, the intact tuff specimens exhibit a rather linear response, with D at $\gamma = 0.01\%$ generally less than $2D_{min}$. This response is more linear than typically exhibited by sands, as seen by comparing the results with the D-log γ curves proposed by Seed et al. (1986, Figure 6) for sands. There are, however, three obvious exceptions, UTA-23-C (Figure 129), UTA-23-B (Figure 130), and UTA-23-A (Figure 131). These specimens exhibited significant increases in D as γ increases above 10^{-4} percent.

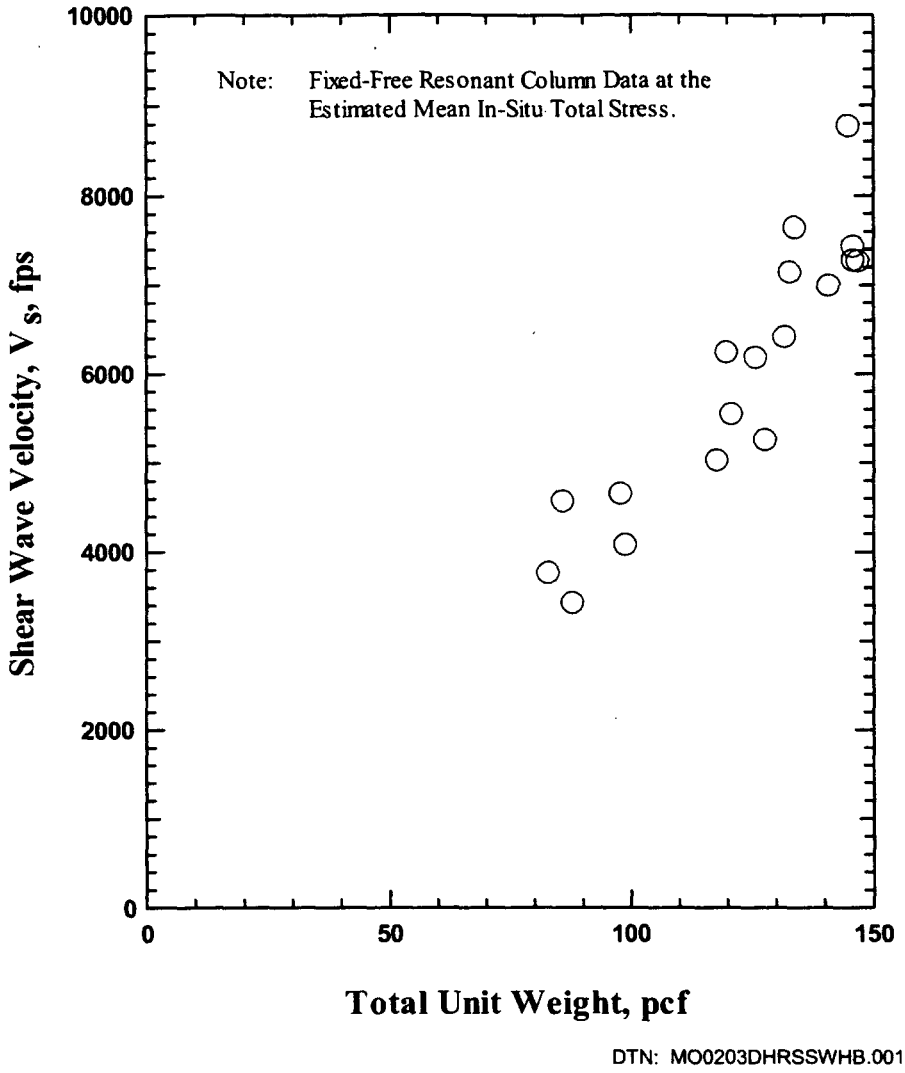

DTN: MO0203DHRSSWHB.001

Figure 119. Variation of Shear-Wave Velocity Measured in the Laboratory at In-Situ Mean Total Stress with Total Unit Weight of Intact Tuff Specimens

In addition to grouping the samples by unit dry weight, the specimens were grouped by lithostratigraphic unit: Tpcpmn, Tpcpln, Tpcpul, Tpcrn, and Tpki (see Section 6.6.2 for a review of lithostratigraphic units). The influence of shearing strain on normalized G and damping ratio for the five types of tuff are shown on Figures 132 to 136. As shown, the units of Tiva Canyon Tuff exhibit only a small amount of nonlinearity in normalized G except for UTA-23-B. The discordant behavior of the same specimens noted earlier (e.g., UTA-23-A on Figure 136) are also apparent in the plots of D versus shearing strain (Figures 129 to 131).

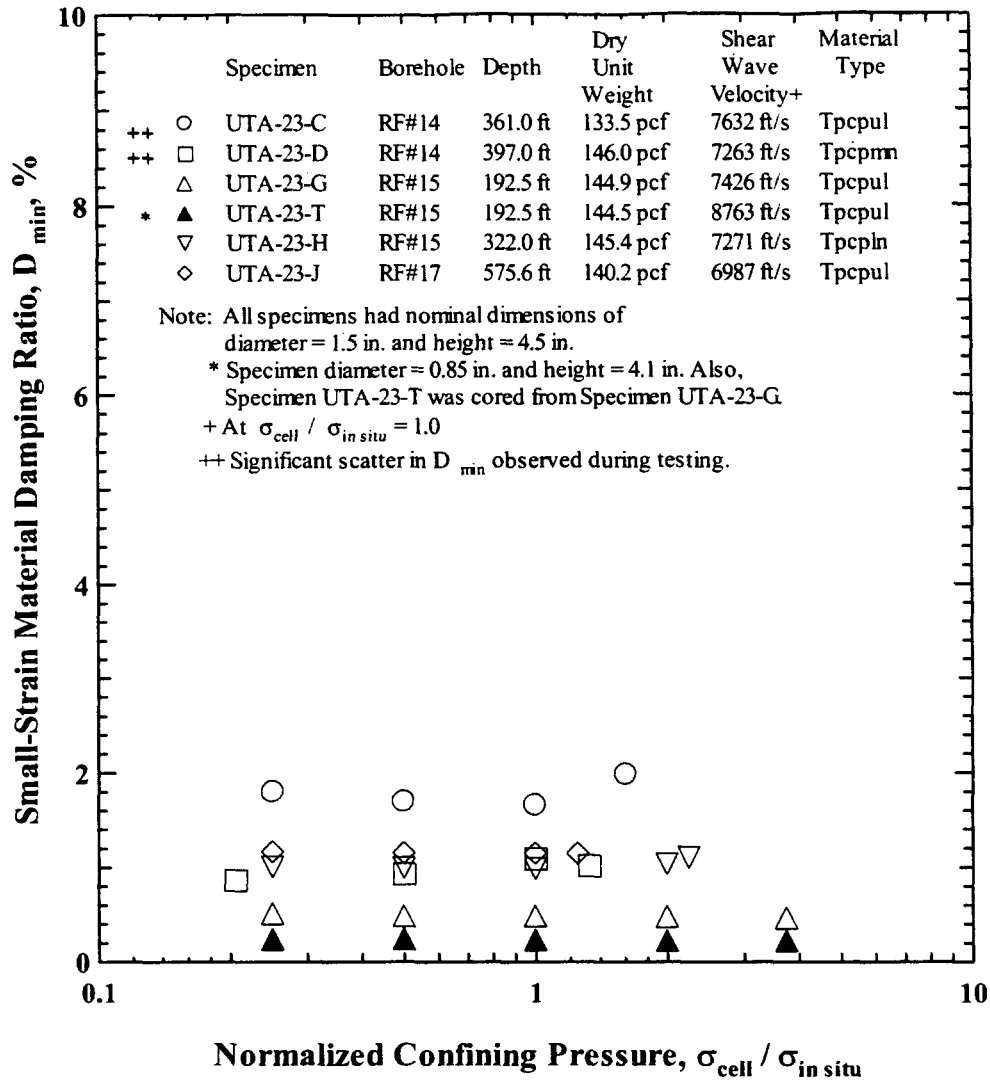

Source: Wong (2002e, Appendix 42, page 32)

Figure 120. Variation in Small-Strain Material Damping Ratio with Normalized Confining Pressure of Group 1 Intact Tuff Specimens

On Figures 137 and 138, Tpki is separated out from the Tiva Canyon Tuff units (Tpcpmn, Tpcpul, and Tpcrn) and the effects of shearing stress on normalized G and D are shown. The results from the 1999 testing (DTN: MO9905LABDYNRS.000) are also shown on Figures 137 and 138. In general, the 2000 tests of the Tpcrn show more nonlinear behavior in terms of normalized G and D at higher strains than was observed for the welded Tiva Canyon Tuff results in 1999 (Figure 137). The 2000 Tpki test results are consistent with the 1999 results in the behavior of normalized G. However, the 2000 test results show significant nonlinear behavior in material damping at strains of only 0.001% for one specimen (Figure 138).

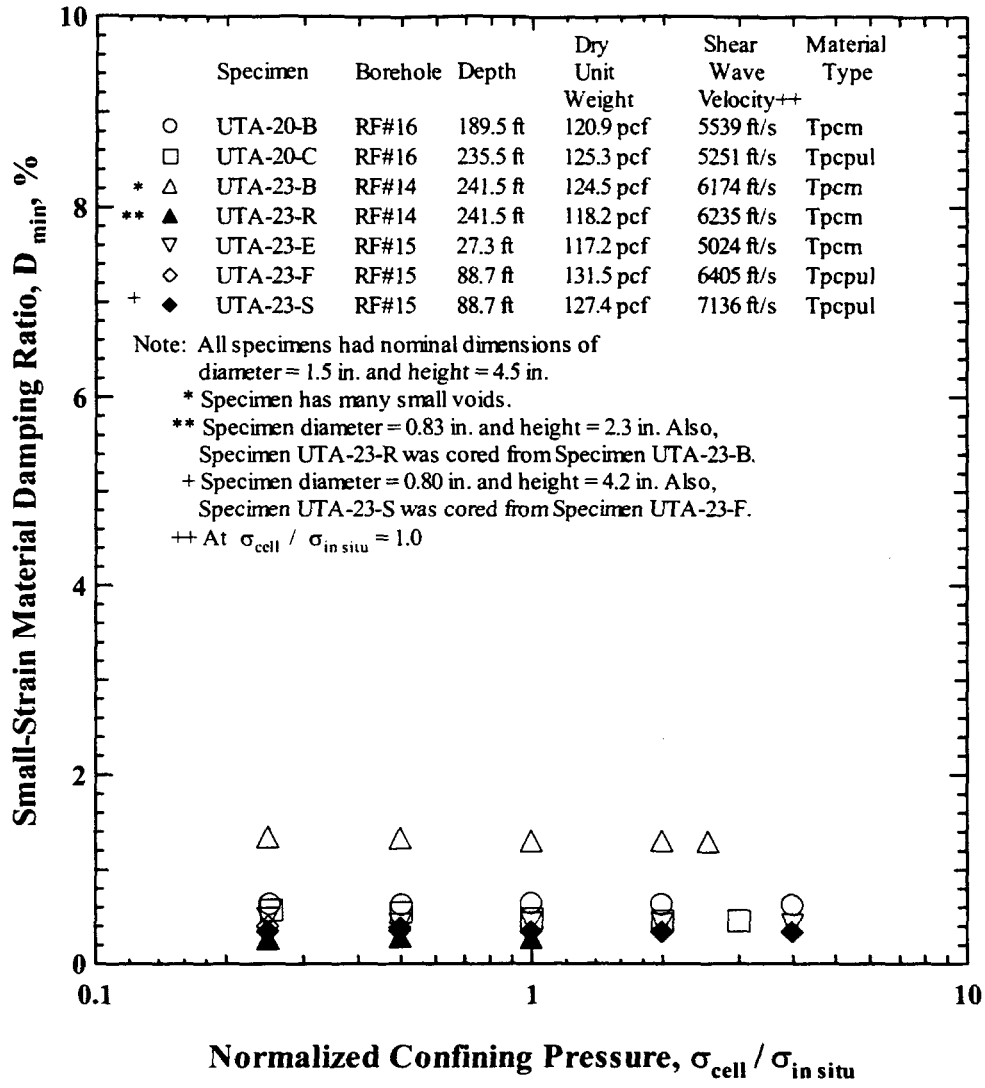

Source: Modified from Wong (2002e, Appendix 42, page 33)

Figure 121. Variation in Small-Strain Material Damping Ratio with Normalized Confining Pressure of Group 2 Intact Tuff Specimens

Small- and Large-Strain Behavior of Reconstituted Alluvial Specimens

The effects of σ on G_{max} and D_{min} of the reconstituted specimen of Quaternary alluvium are shown on Figures 139 and 140, respectively. This reconstituted material is behaving like a granular soil, as expected. The effects of f on G_{max} and D_{min} are small (Figures XII-26 and XII-27). The effects of γ on G, G/G_{max} and D are shown on Figures 141 to 143, respectively. Again, the material is behaving like a sandy soil, as shown by the comparisons with the curve for sand in Seed et al. (1986, Figures 2 and 6) on Figures 142 and 143.

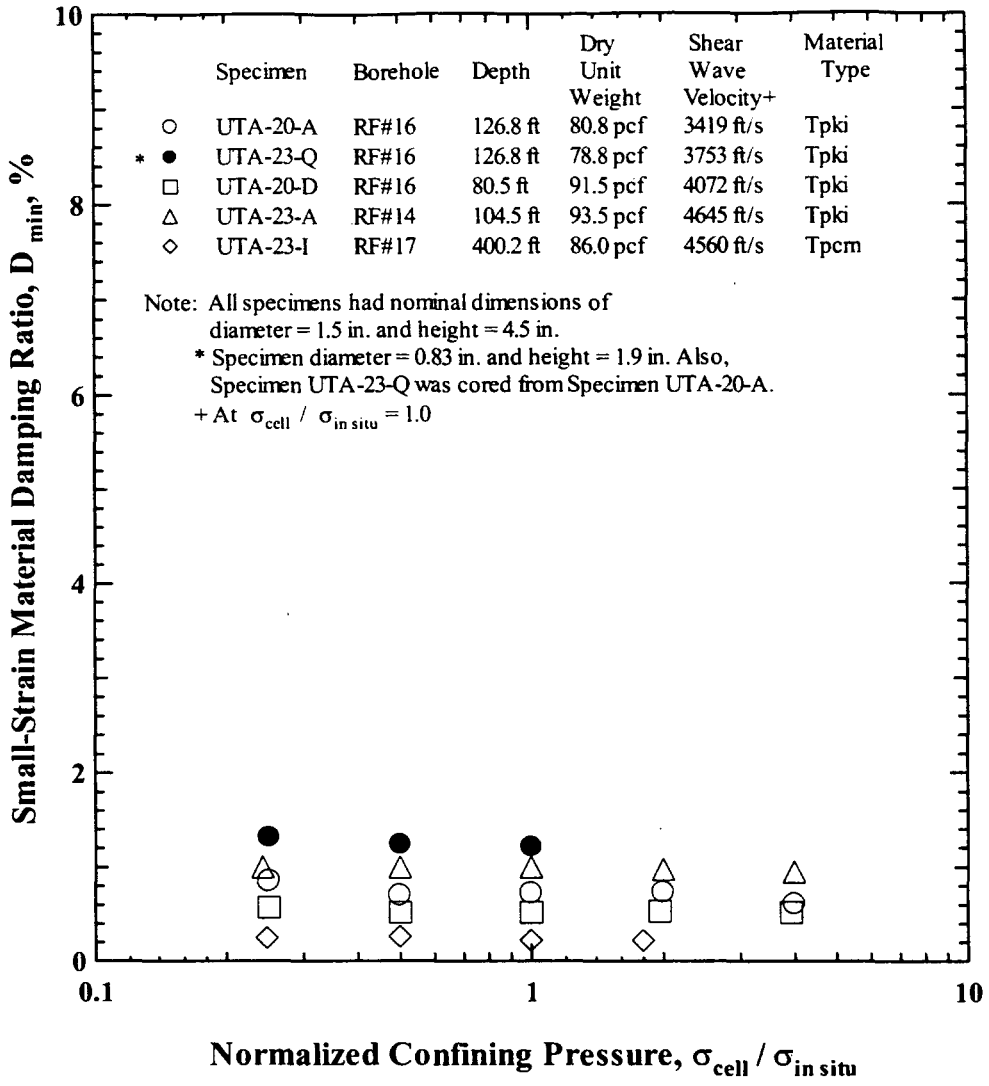

Source: Modified from Wong (2002e, Appendix 42, page 34)

Figure 122. Variation in Small-Strain Material Damping Ratio with Normalized Confining Pressure of Group 3 Intact Tuff Specimens

6.2.10.4 Limitations of Test Equipment

The RCTS equipment has several limitations, which are apparent from the test results. The limitations include the confining pressure range over which testing can be performed and the shearing strain range that can be excited in the test specimens.

The maximum test pressure of the confinement chamber is around 500 psi (3.4 MPa). Therefore, a slightly lower pressure of 460 psi (3.1 MPa) was the maximum pressure used to confine the tuff specimens from the greatest depths, which would have in-situ mean stresses greater than or equal to 460 psi.

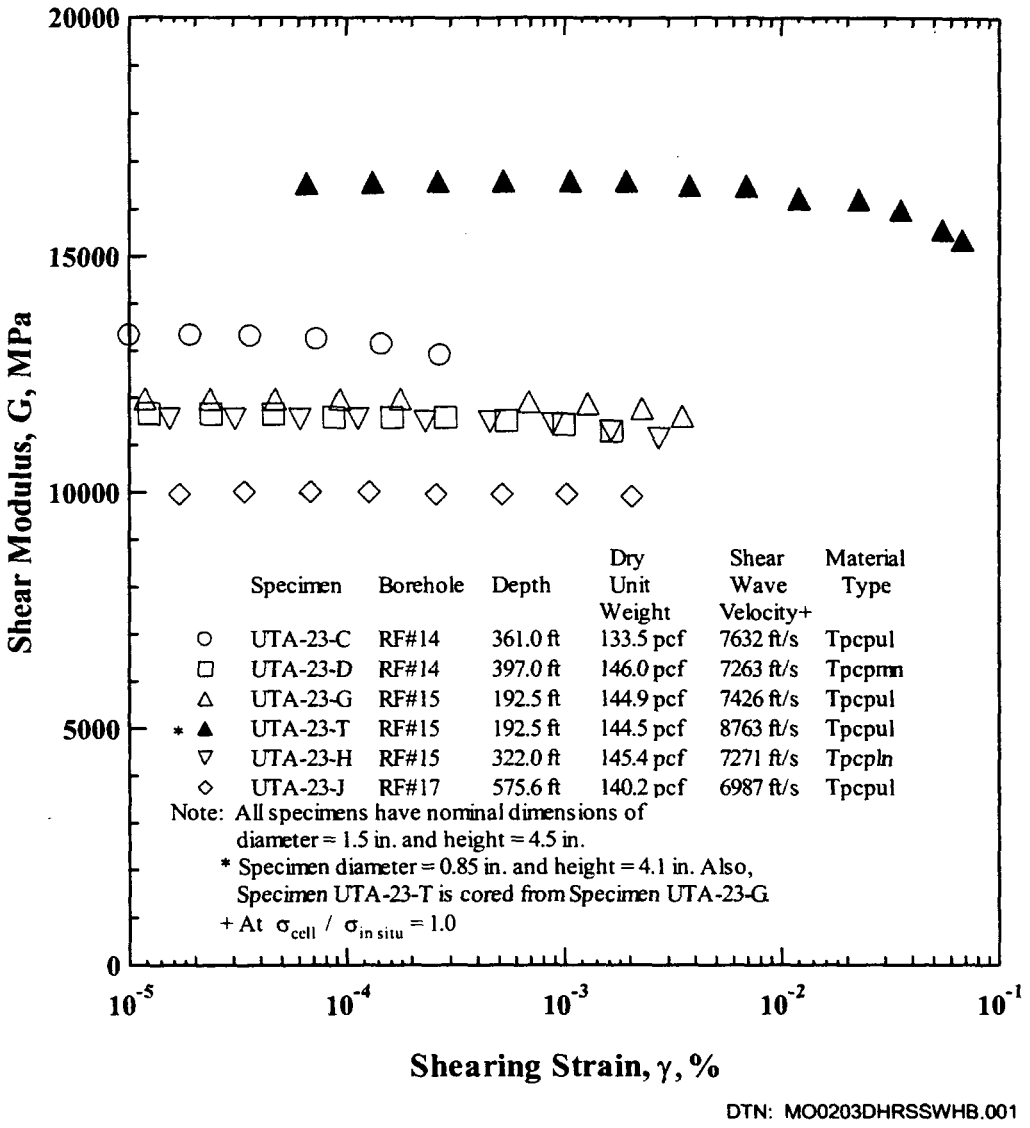

Figure 123. Variation in Shear Modulus with Shearing Strain of Group 1 Intact Tuff Specimens

The maximum shearing strain of about 0.1% was generated in the granular fill specimens because these were the least stiff specimens (discussed in Section 6.5.3). The maximum strain was generated in resonance, not in torsional shear, because of the dynamic amplification associated with resonating a specimen.

It is important to note that the limitation on torque generated by this equipment in the torsional shear testing combined with the large stiffness of the tuff specimens resulted in very small strains being generated in the tests. Sometimes the strains were below 5 x 10^{-4}%, which is around the threshold resolution level in torsional shear testing with this equipment (Kim and Stokoe 1994,

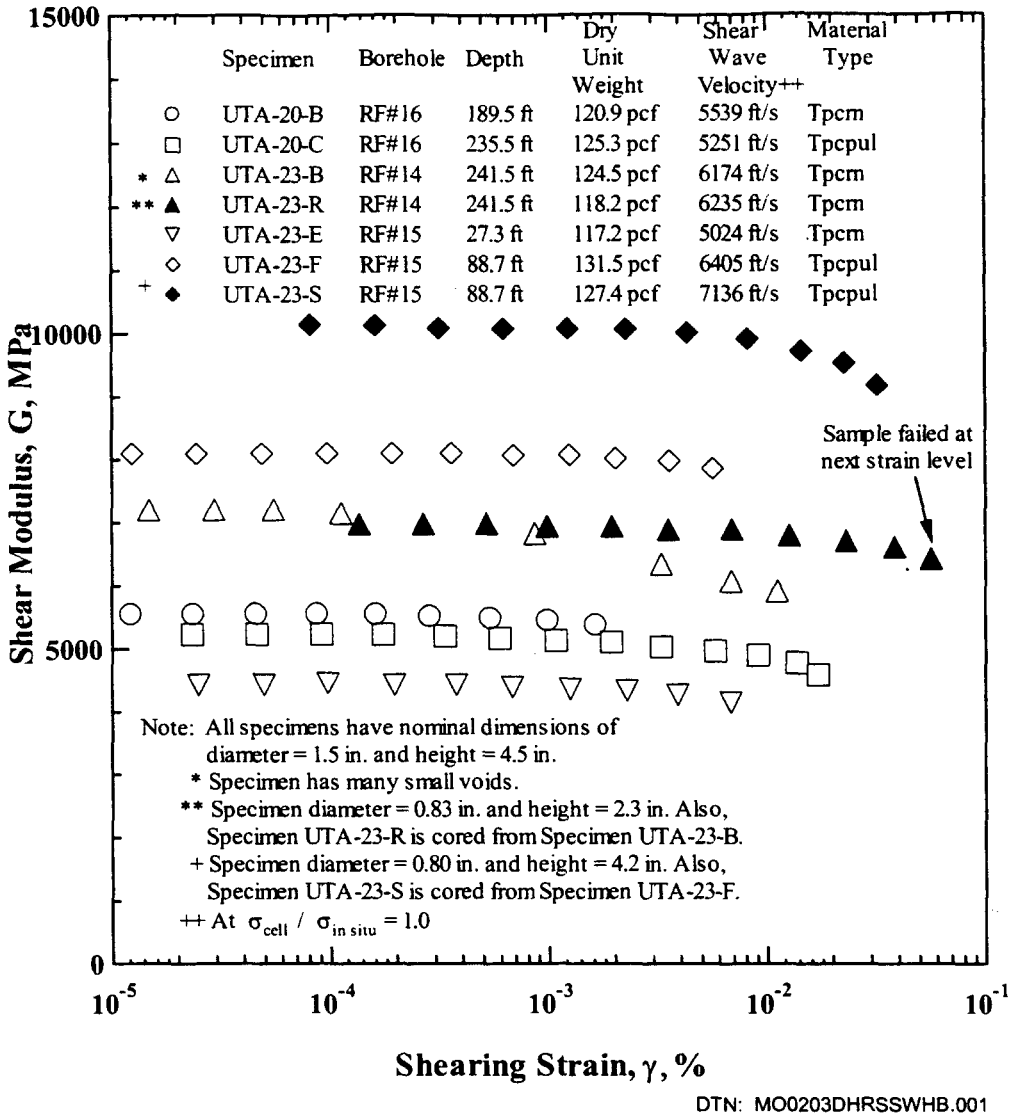

Figure 124. Variation in Shear Modulus with Shearing Strain of Group 2 Intact Tuff Specimens

page 25, Figure 10). Therefore, considerable scatter occurred in the very small strain measurements, especially in evaluations of D_{min}.

Two other limitations that could have potentially impacted the results are: 1) the highly nonlinear behavior in resonant column testing that occurs at strains greater than about 0.5% in specimens, and 2) extremely stiff specimens, which result in straining or movement in the base pedestal and top cap. The first limitation did not occur in these tests, as determined by all strain measurements which were less than 0.2%. The second limitation was checked by independent testing. This was done by testing several tuff specimens with free-free resonant column equipment (Wong 2002e, Appendix 42, page 11). The general free-free test set-up is described in Stokoe, Hwang et al. (1994). In these tests there are no end plates and both ends of the

specimen are free to move. Although these tests are unqualified (i.e., were not conducted in accordance with the YMP quality assurance procedures), the same calibrated waveform analyzer as used to verify the RCTS equipment was used to perform the free-free tests. Comparison of the results in terms of shear-wave velocities measured in each type of resonant column test is shown on Figure XII-28. As shown, the shear-wave velocities measured in the fixed-free test are generally equal to or slightly greater than the velocities measured in the free-free resonant column test, verifying the proper functioning of the RCTS equipment (fixed-free resonant column) and showing that base fixity was not a limitation in these results.

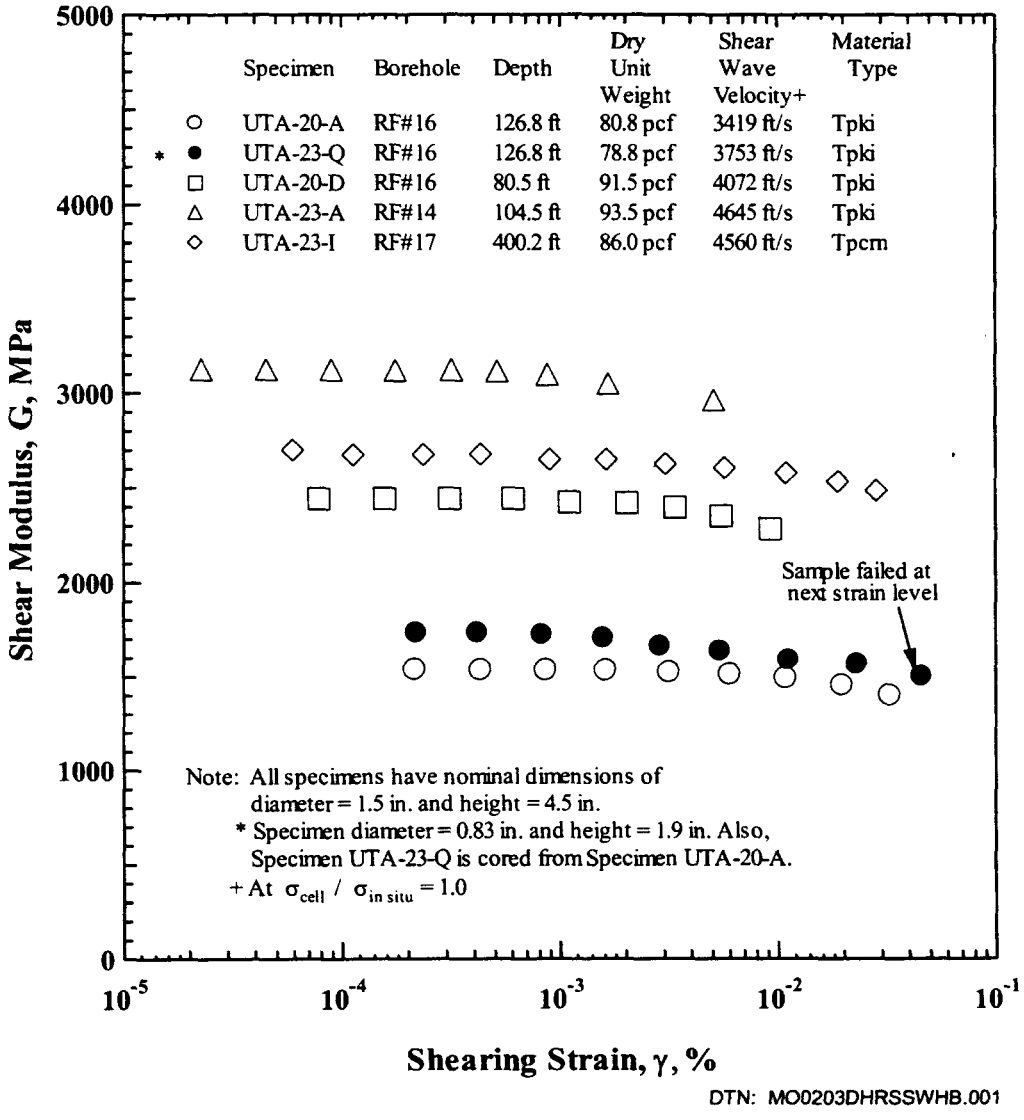

Figure 125. Variation in Shear Modulus with Shearing Strain of Group 3 Intact Tuff Specimens

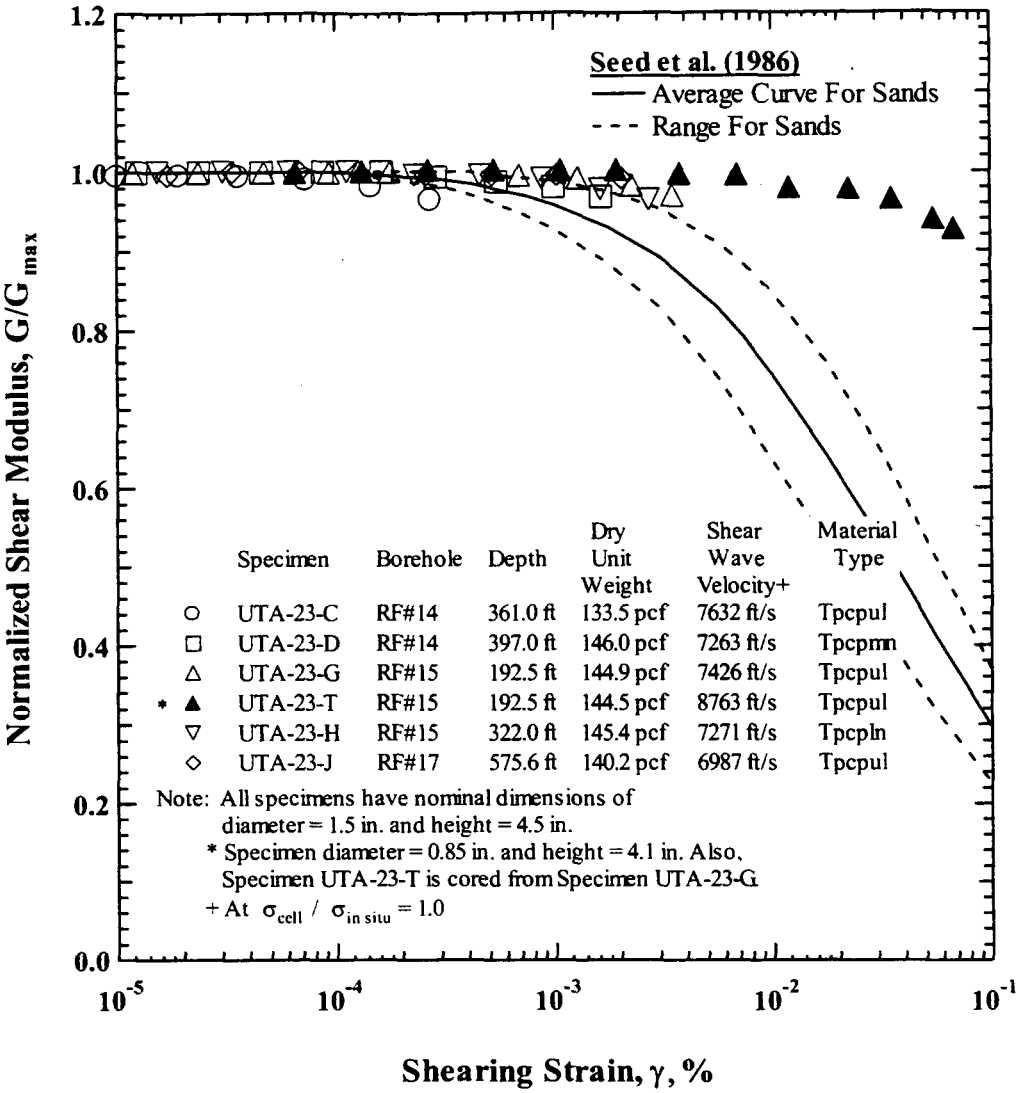

DTN: MO0203DHRSSWHB.001

Figure 126. Variation in Normalized Shear Modulus with Shearing Strain of Group 1 Intact Tuff Specimens

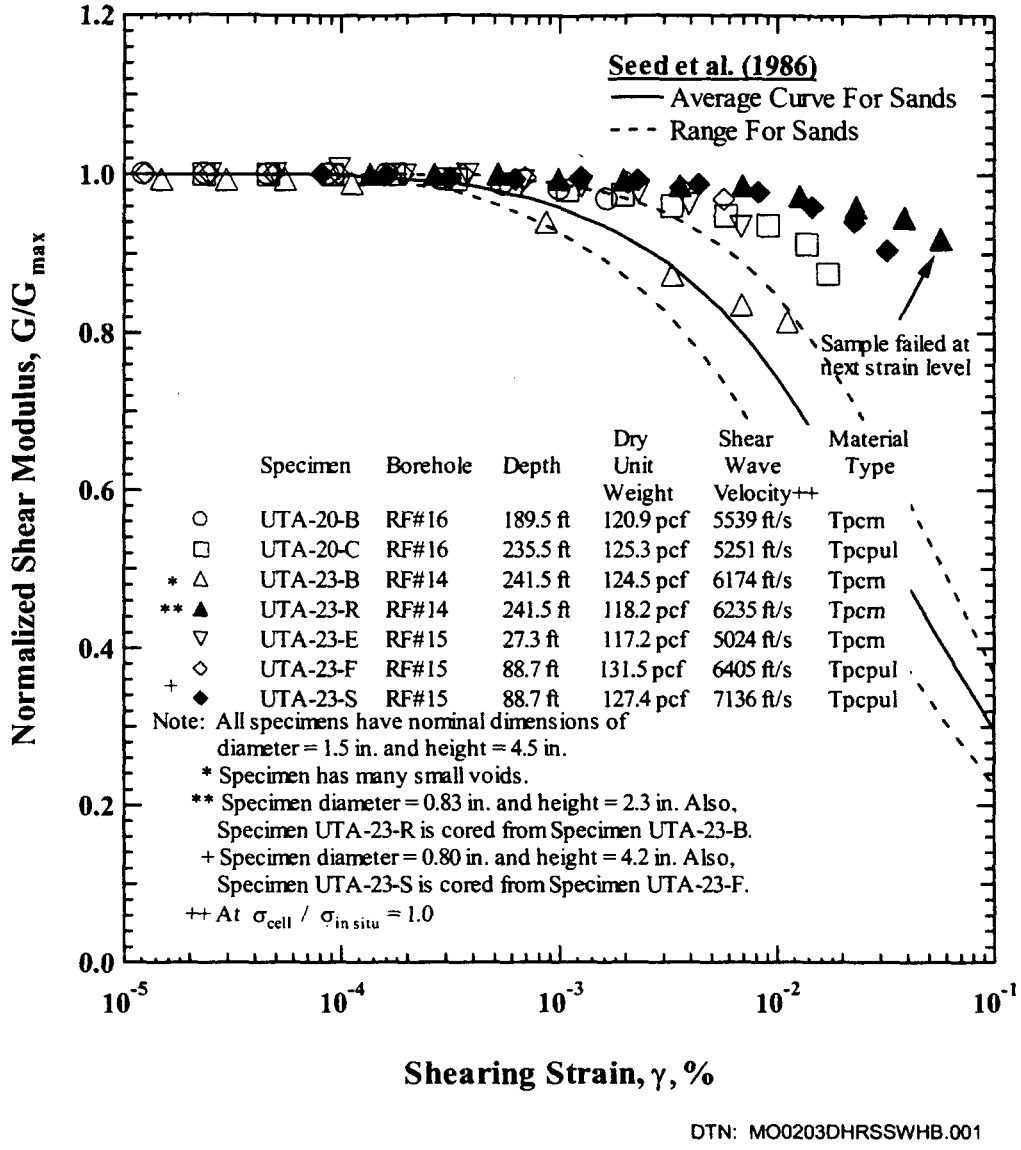

DTN: MO0203DHRSSWHB.001

Figure 127. Variation in Normalized Shear Modulus with Shearing Strain of Group 2 Intact Tuff Specimens

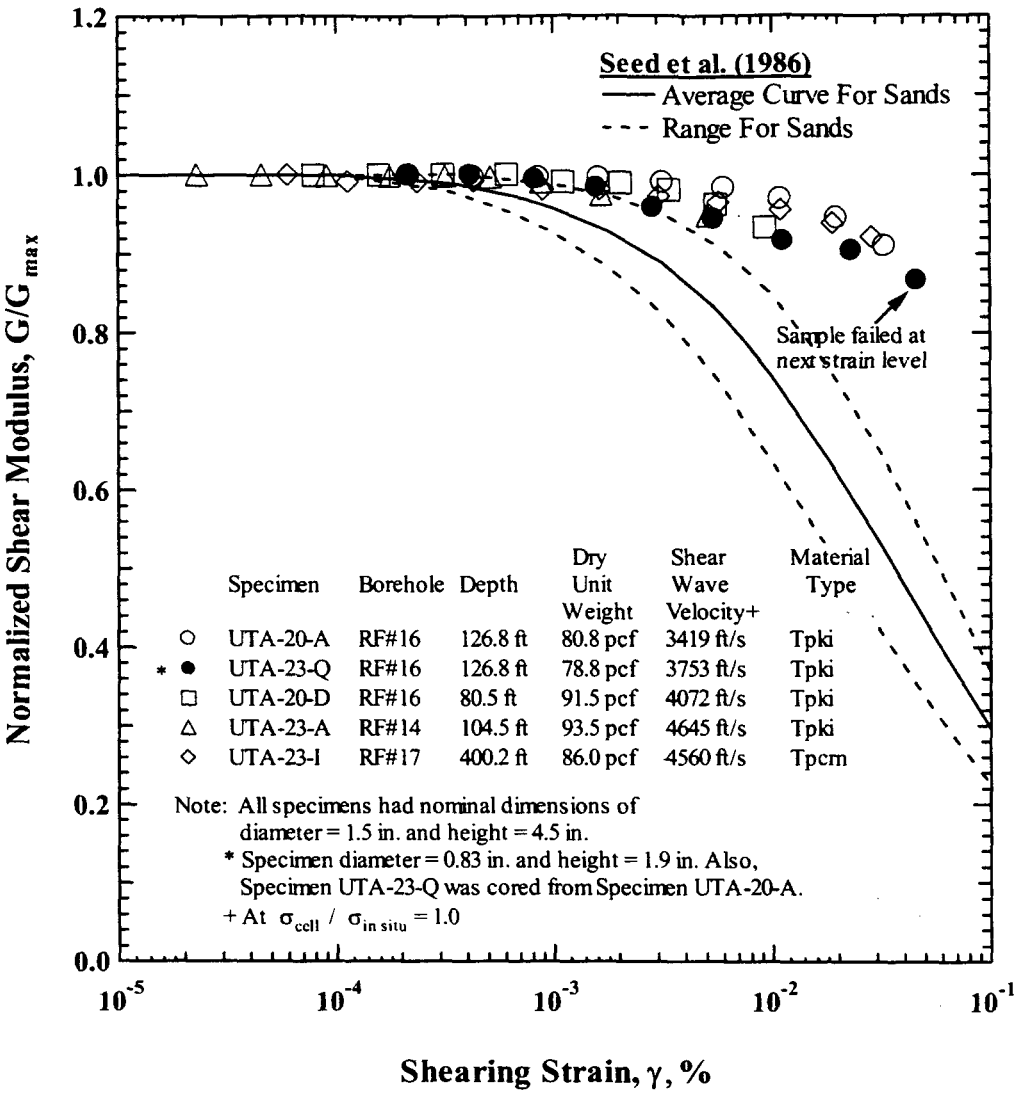

DTN: MO0203DHRSSWHB.001

Figure 128. Variation in Normalized Shear Modulus with Shearing Strain of Group 3 Intact Tuff Specimens

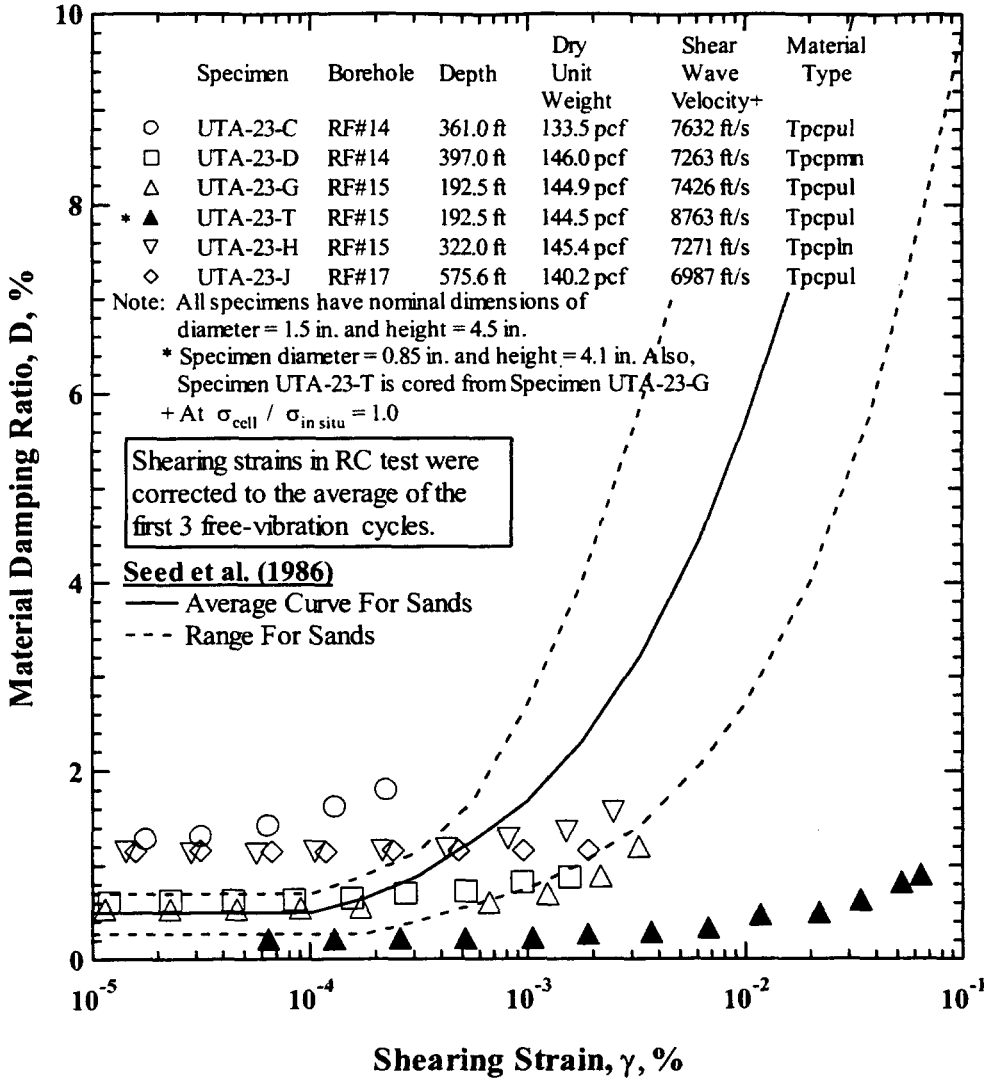

DTN: MO0203DHRSSWHB.001

Figure 129. Variation in Material Damping Ratio with Shearing Strain of Group 1 Intact Tuff Specimens

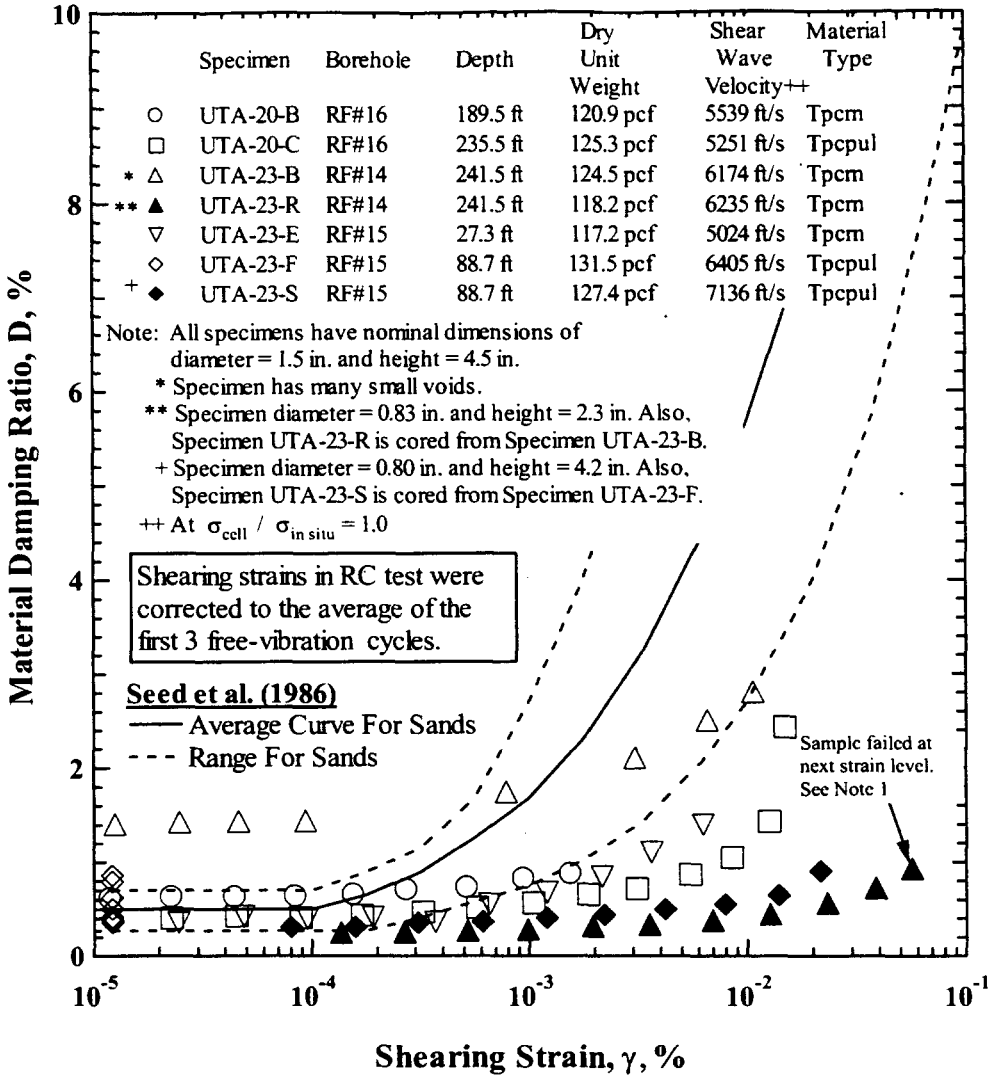

DTN: MO0203DHRSSWHB.001

Note: (1) Wong (2002e, Appendix 42, page 42)

Figure 130. Variation in Material Damping Ratio with Shearing Strain of Group 2 Intact Tuff Specimens

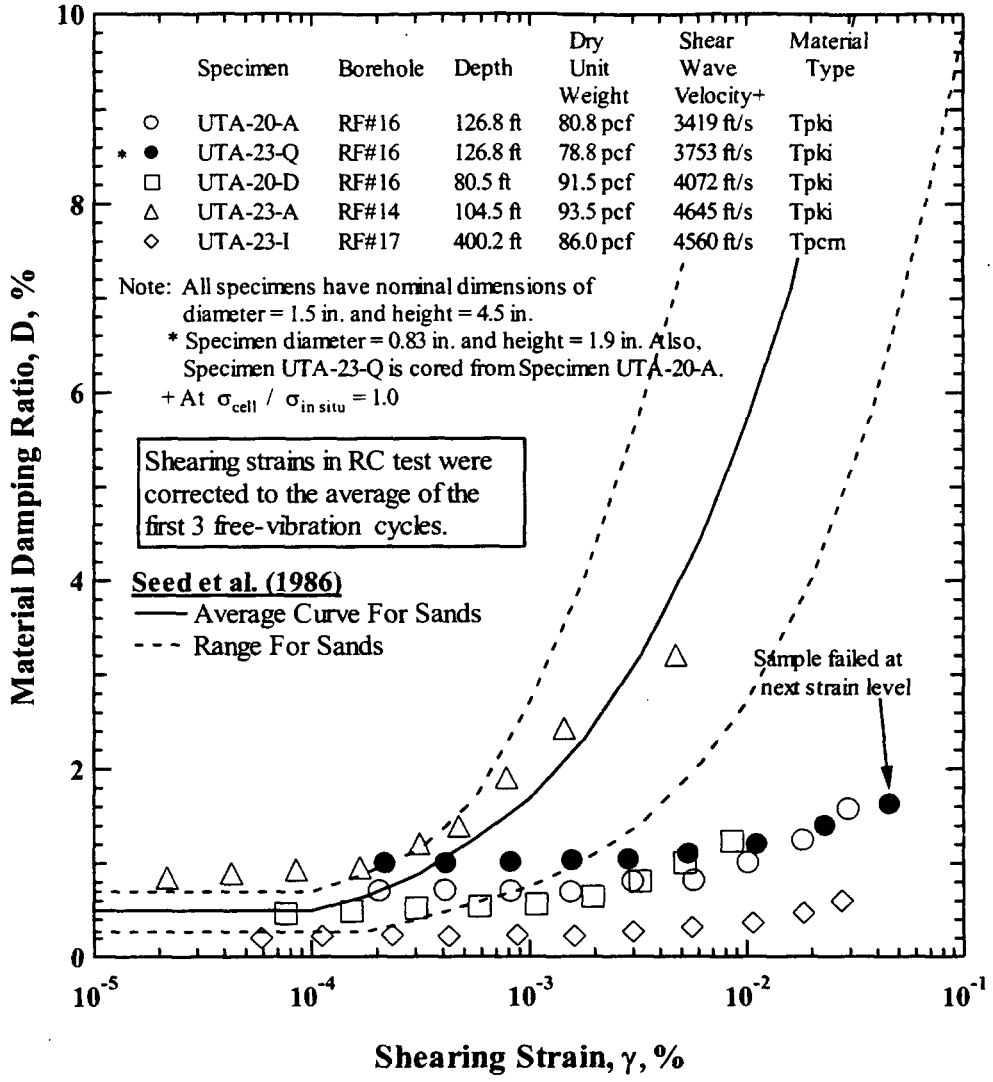

DTN: MO0203DHRSSWHB.001

Figure 131. Variation in Material Damping Ratio with Shearing Strain of Group 3 Intact Tuff Specimens

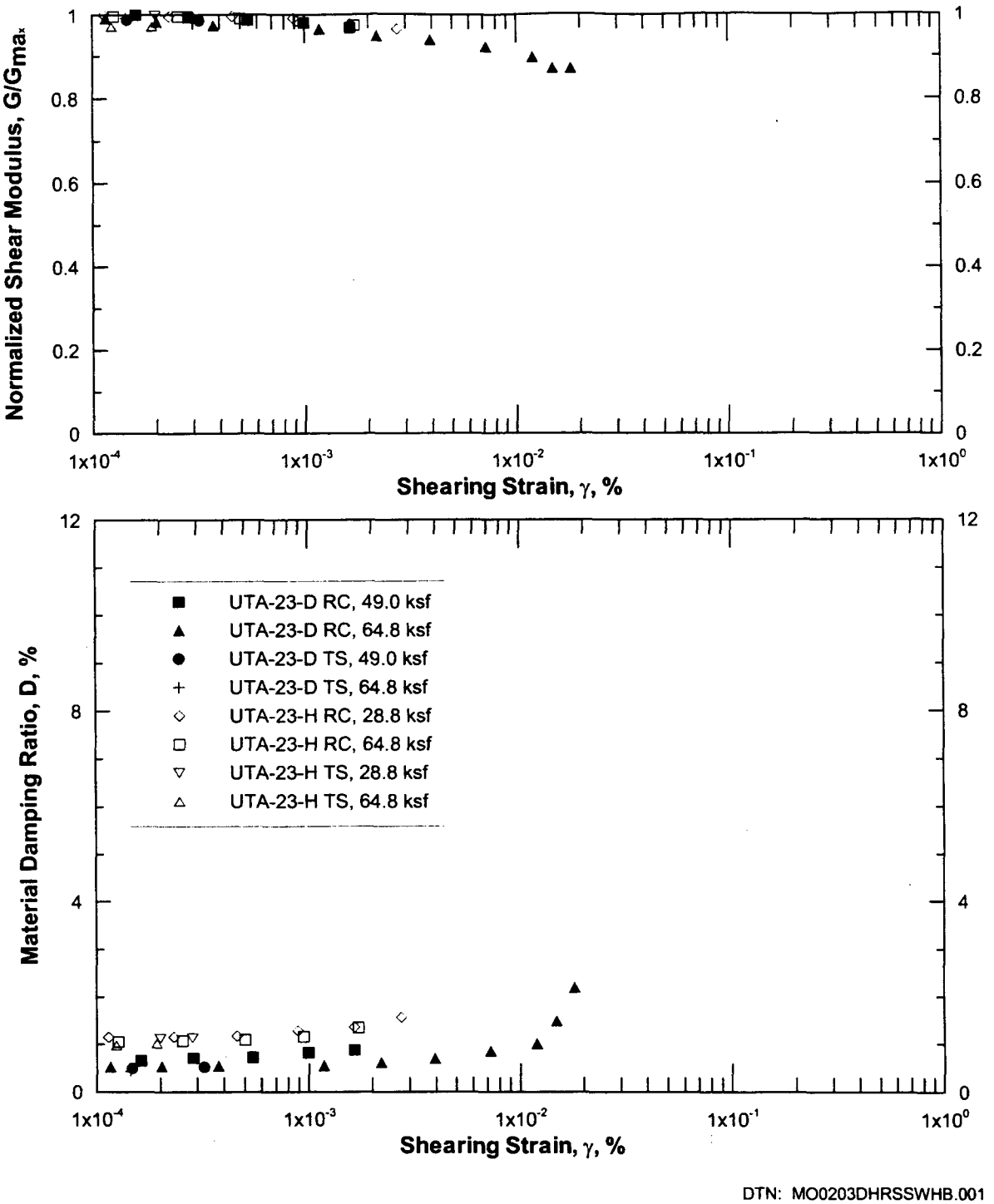

DTN: MO0203DHRSSWHB.001

Figure 132. Resonant Column and Torsional Shear Results for Tpcpmn and Tpcpln

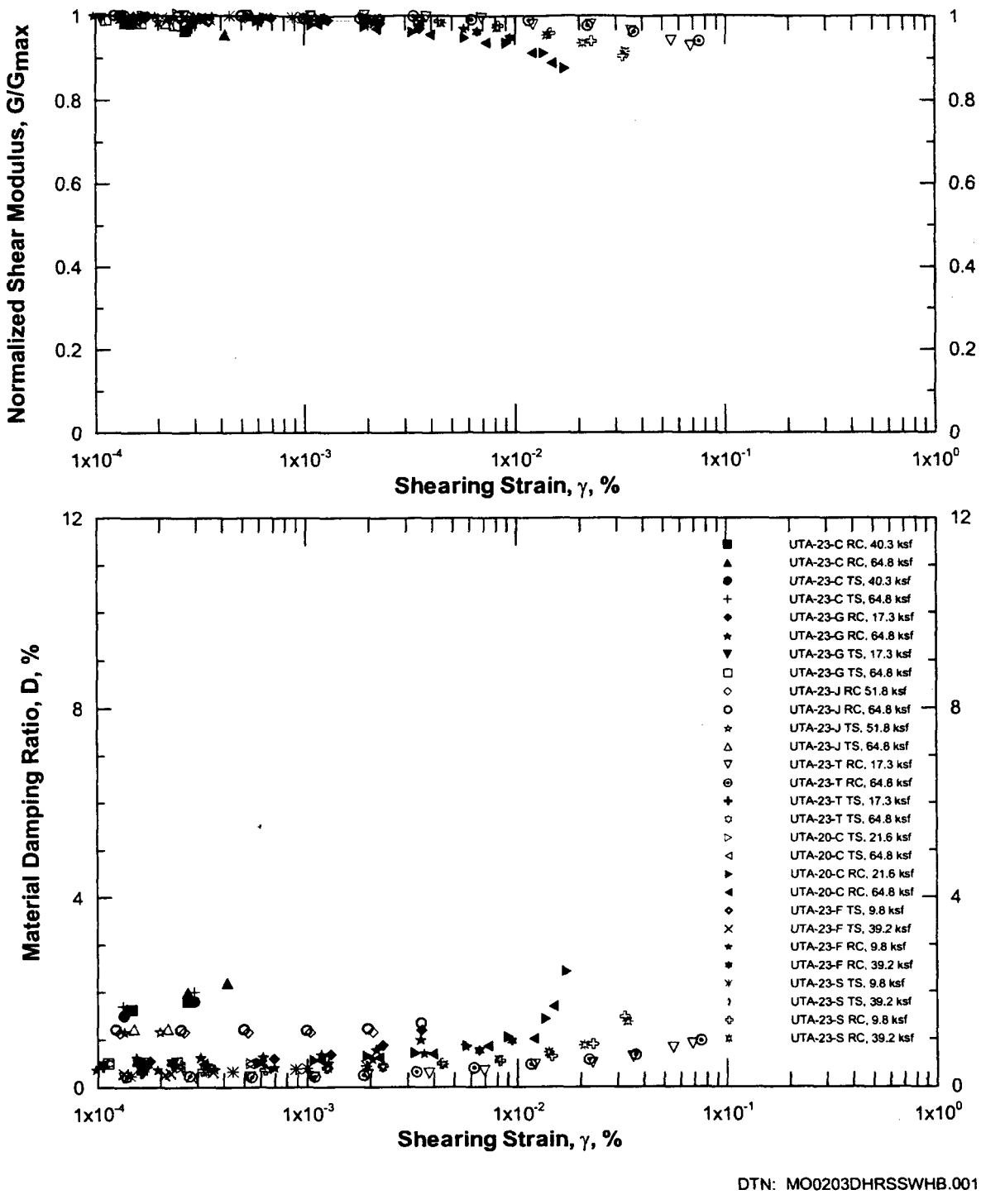

DTN: MO0203DHRSSWHB.001

Figure 133. Resonant Column and Torsional Shear Results for Tpcpul

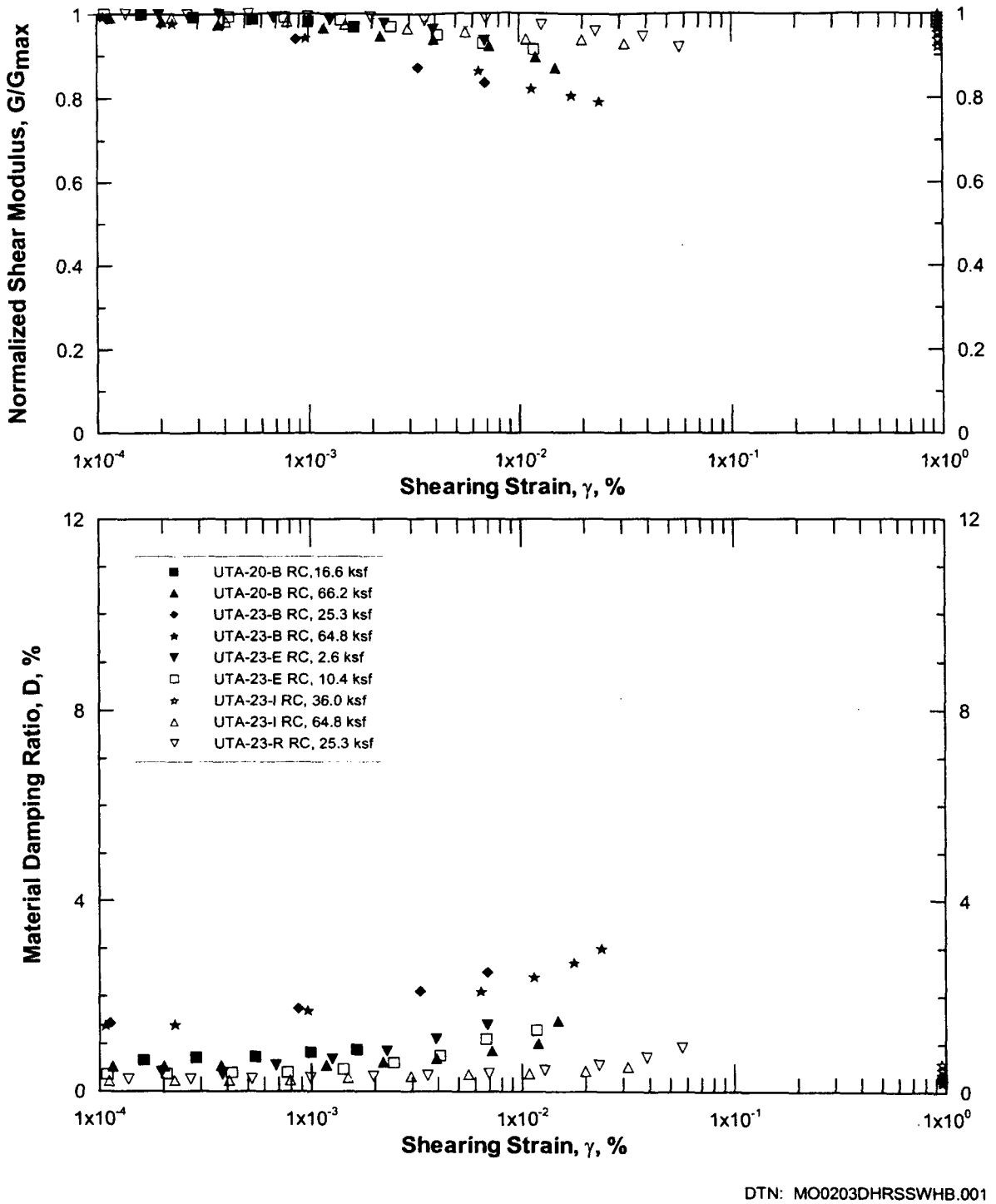

DTN: MO0203DHRSSWHB.001

Figure 134. Resonant Column Shear Results for Tpcm

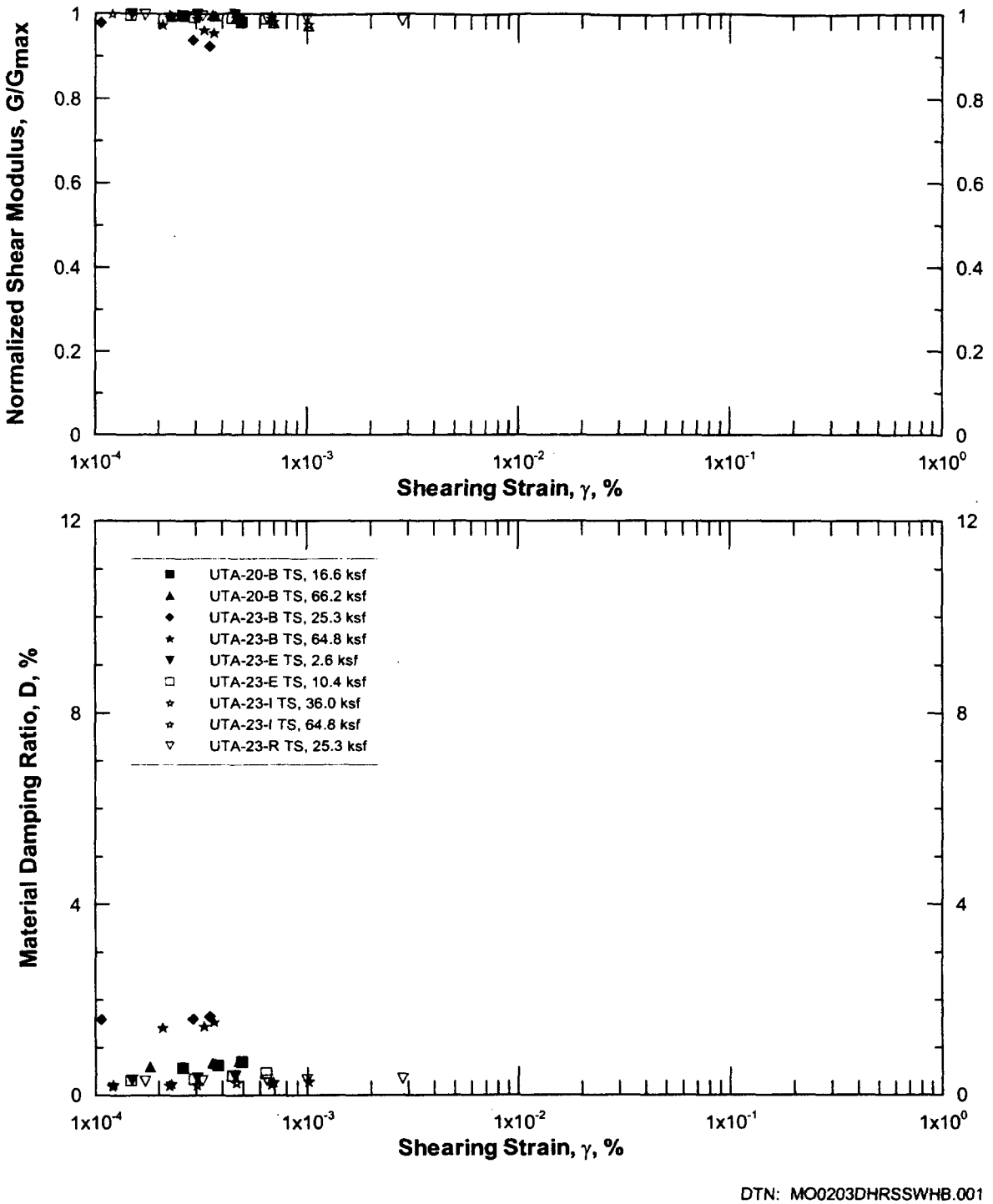

Figure 135. Torsional Shear Results for Tpcrn

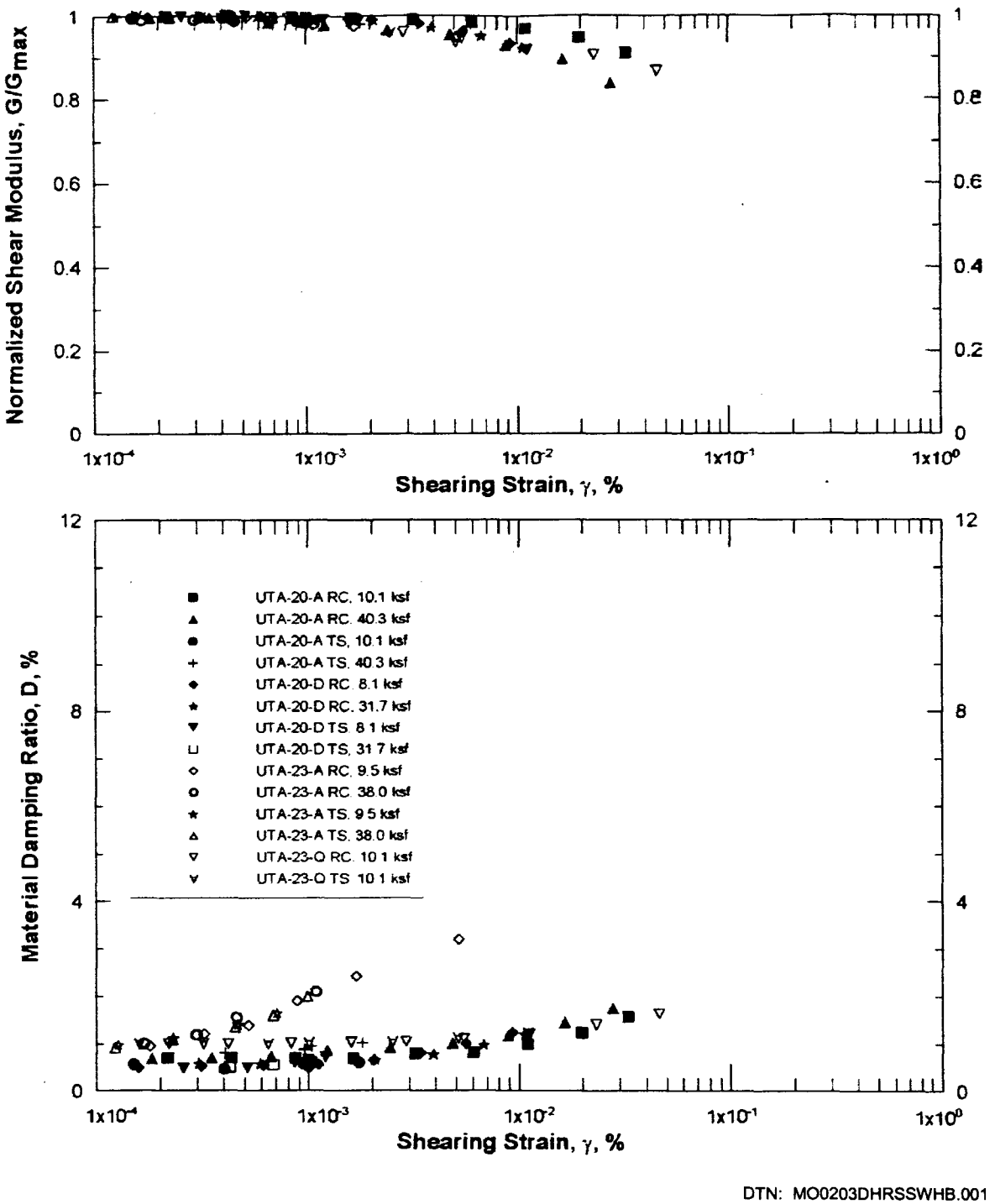

DTN: MO0203DHRSSWHB.001

Figure 136. Resonant Column and Torsional Shear Results for Tpki

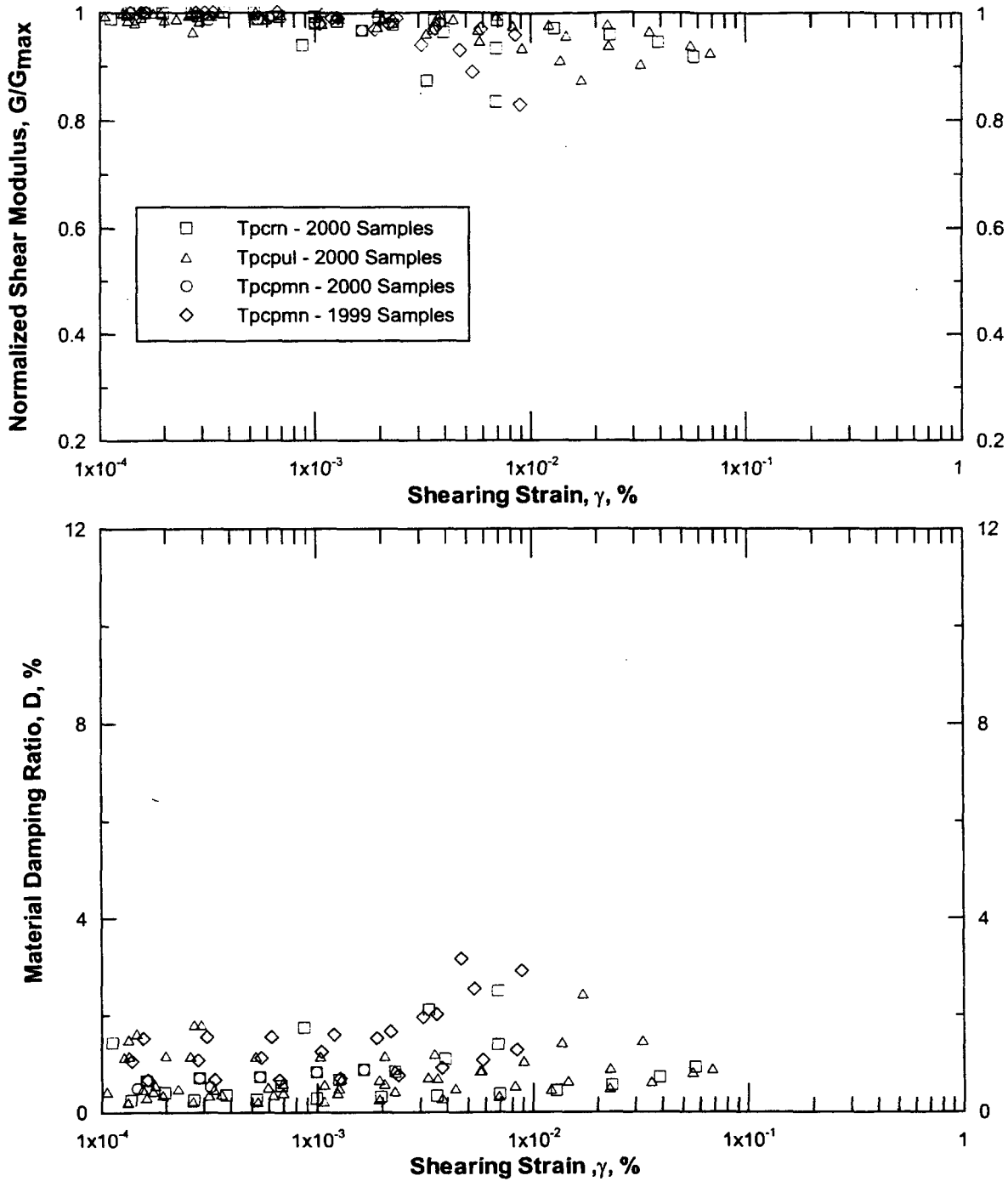

DTNS: MO0203DHRSSWHB.001, MO9905LABDYNRS.000

Figure 137. Resonant Column and Torsional Shear Results for Tiva Canyon Tuff from 1999 Study and This Study

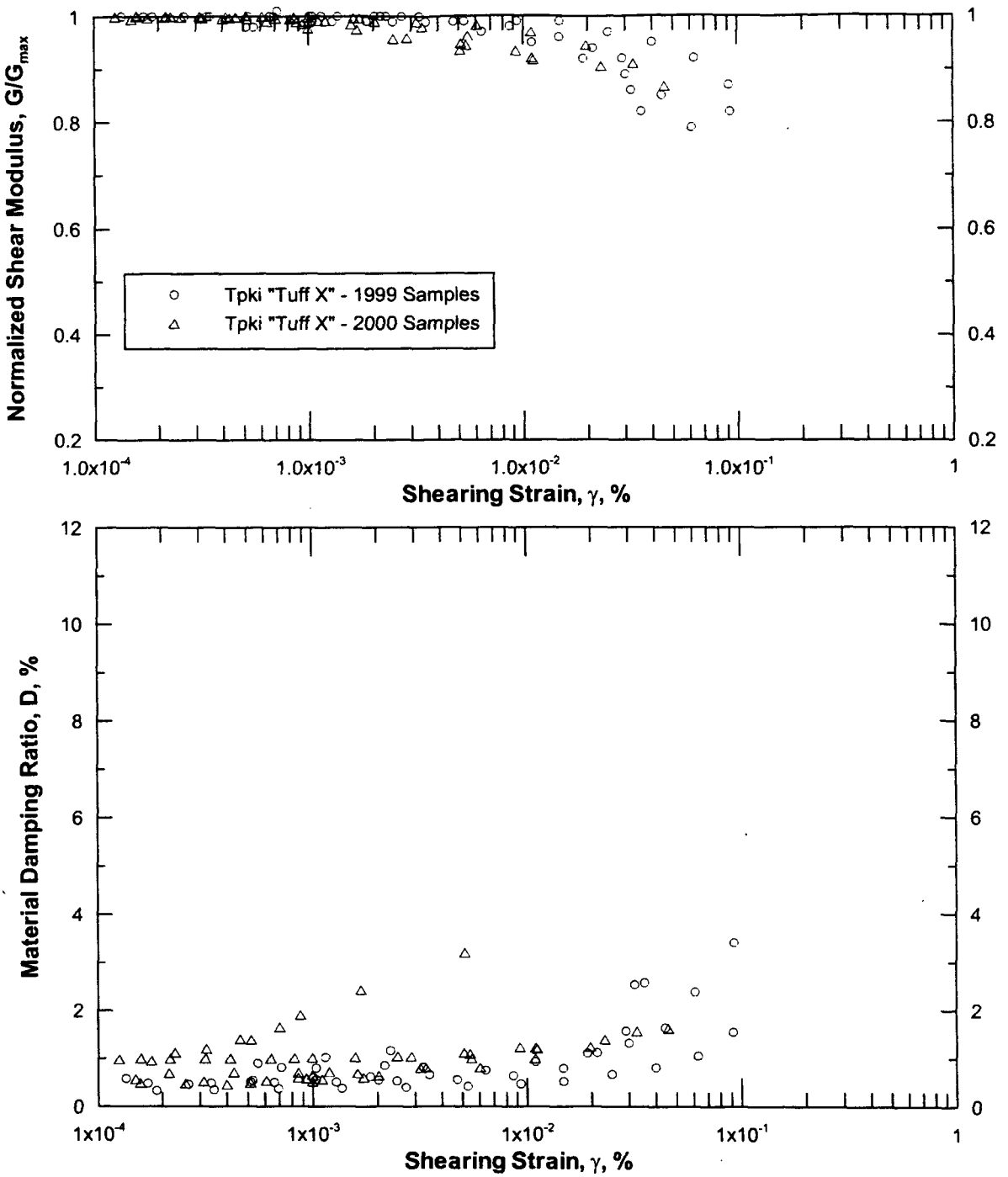

DTNS: MO0203DHRSSWHB.001, MO9905LABDYNRS.000

Figure 138. Resonant Column and Torsional Shear Results for Tpki from 1999 Study and This Study

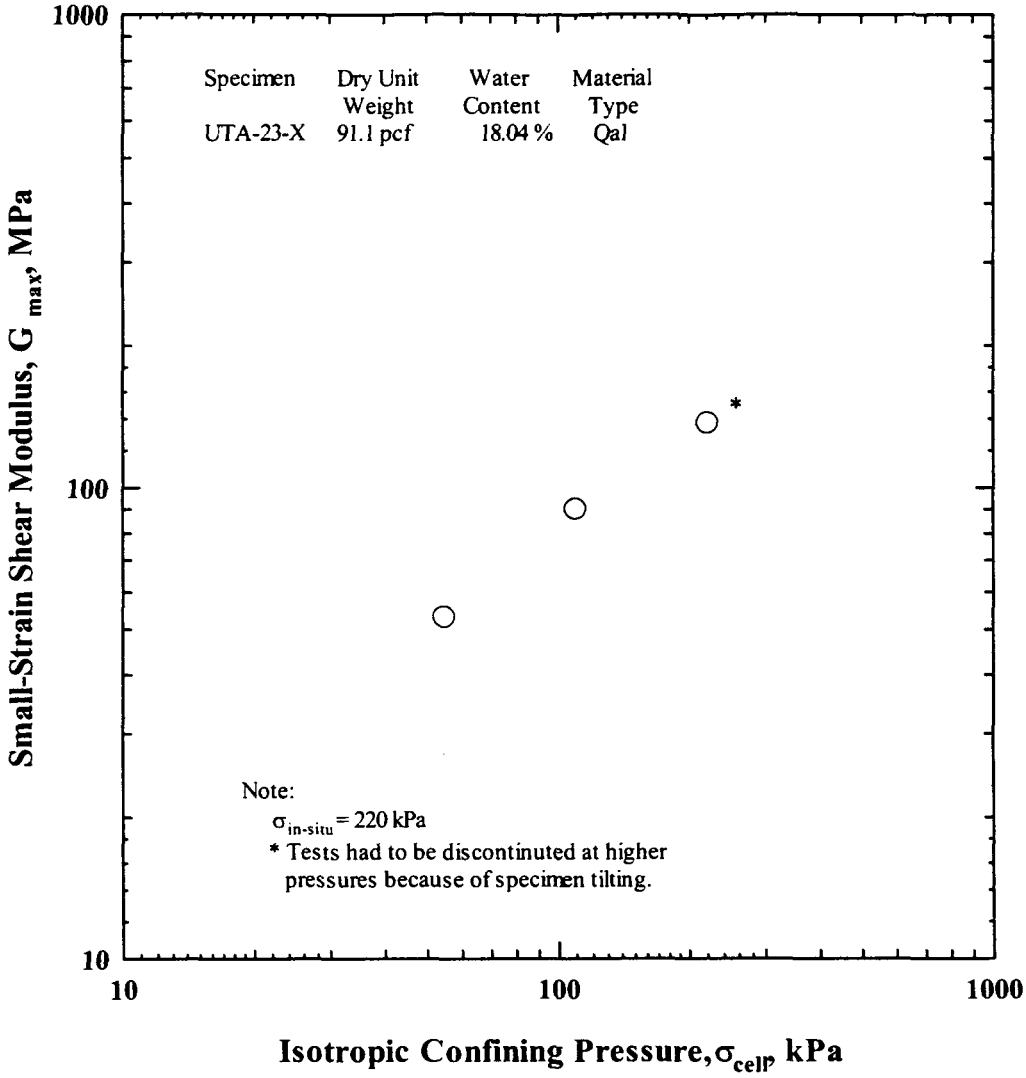

DTN: MO0203DHRSSWHB.001

Figure 139. Variation in Small-Strain Shear Modulus with Isotropic Confining Pressure of Reconstituted Quaternary Alluvium Specimen

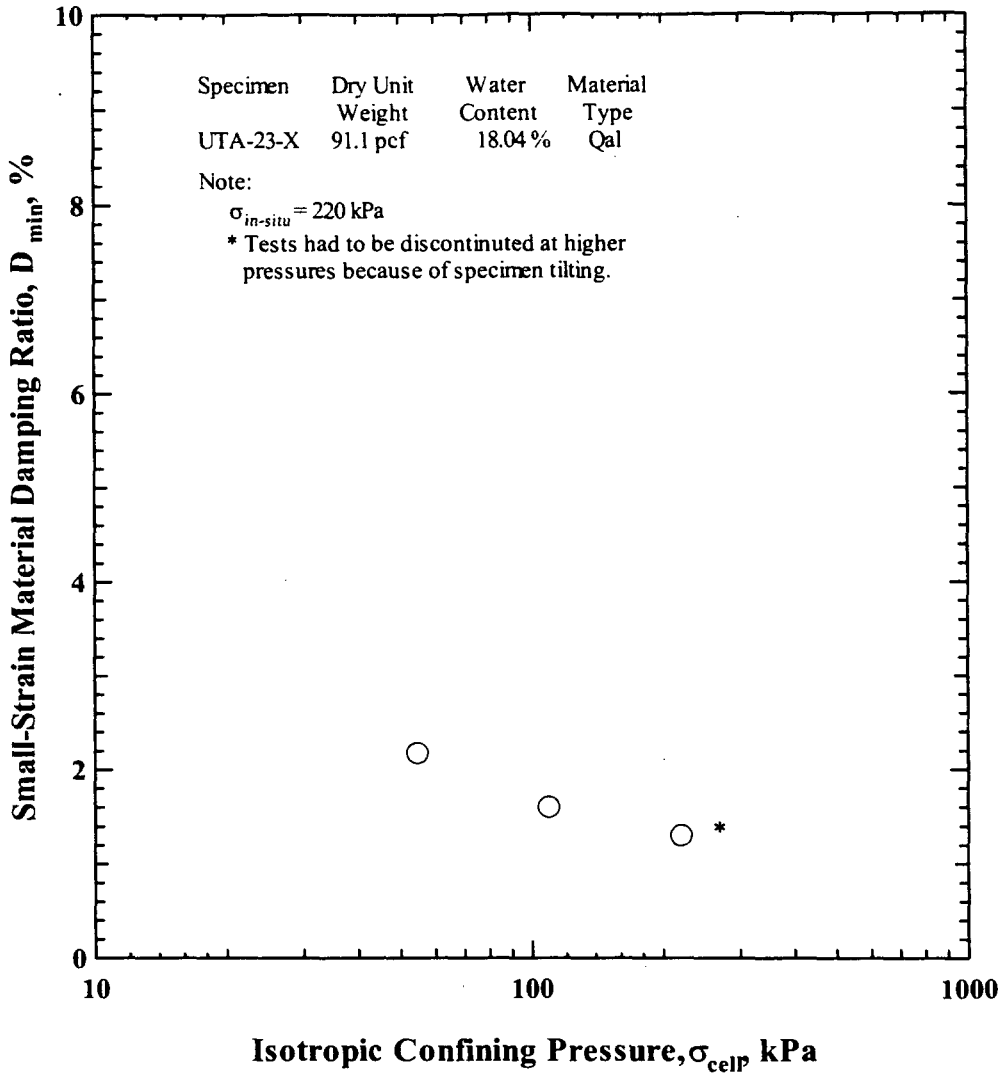

DTN: MO0203DHRSSWHB.001

Figure 140. Variation in Small-Strain Material Damping Ratio with Isotropic Confining Pressure of Reconstituted Quaternary Alluvium Specimen

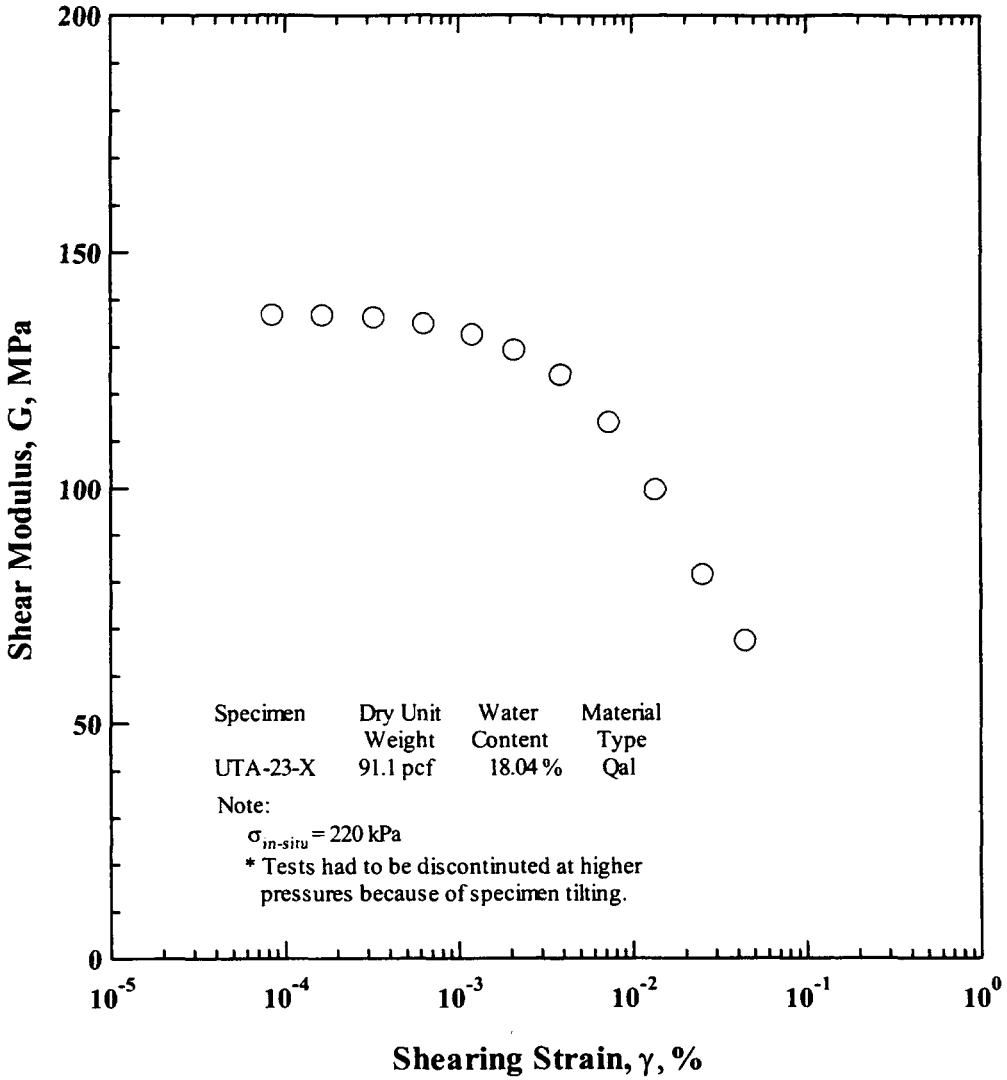

DTN: MO0203DHRSSWHB.001

Figure 141. Variation in Shear Modulus with Shearing Strain of Reconstituted Quaternary Alluvium Specimen

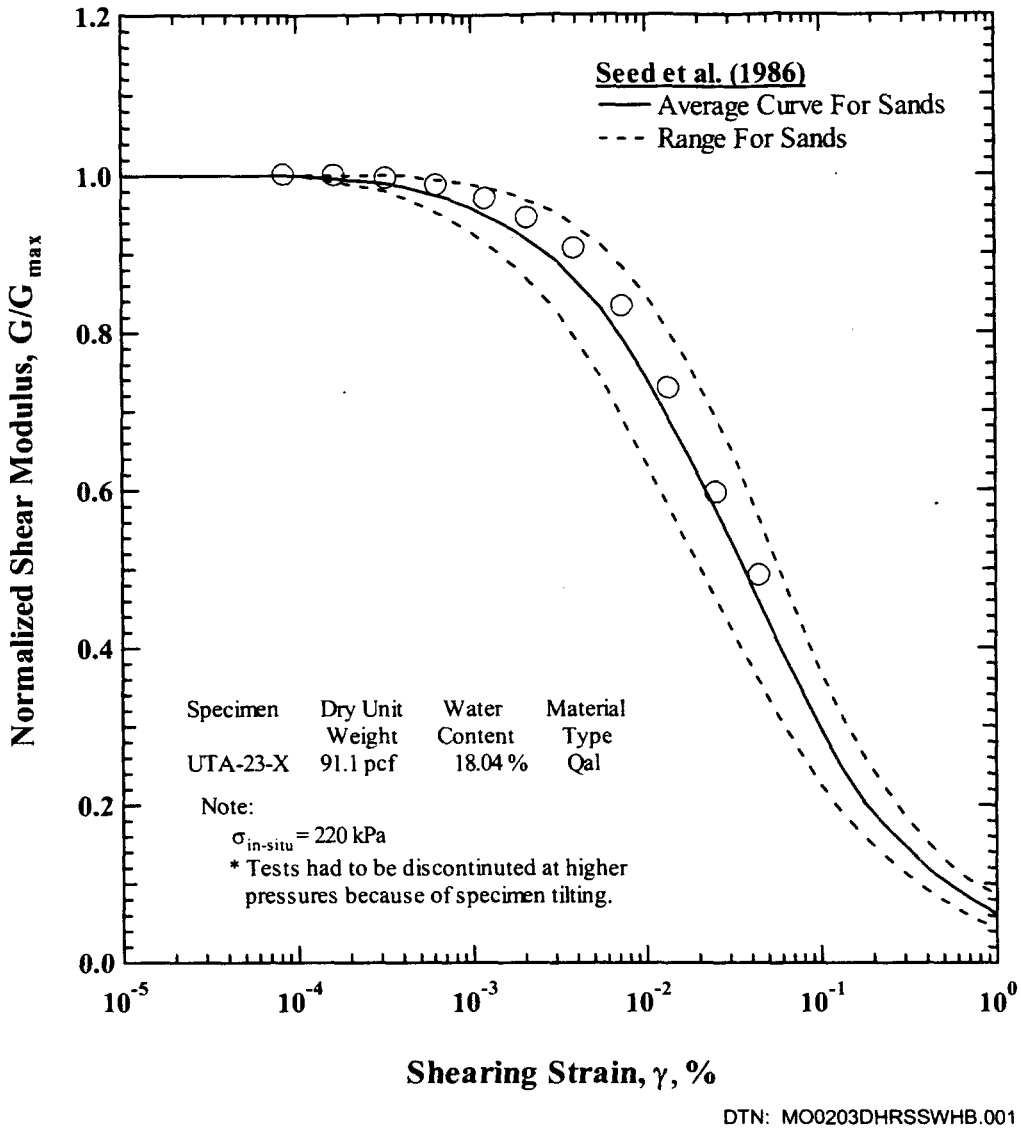

DTN: MO0203DHRSSWHB.001

Figure 142. Variation in Normalized Shear Modulus with Shearing Strain of Reconstituted Quaternary Alluvium Specimen

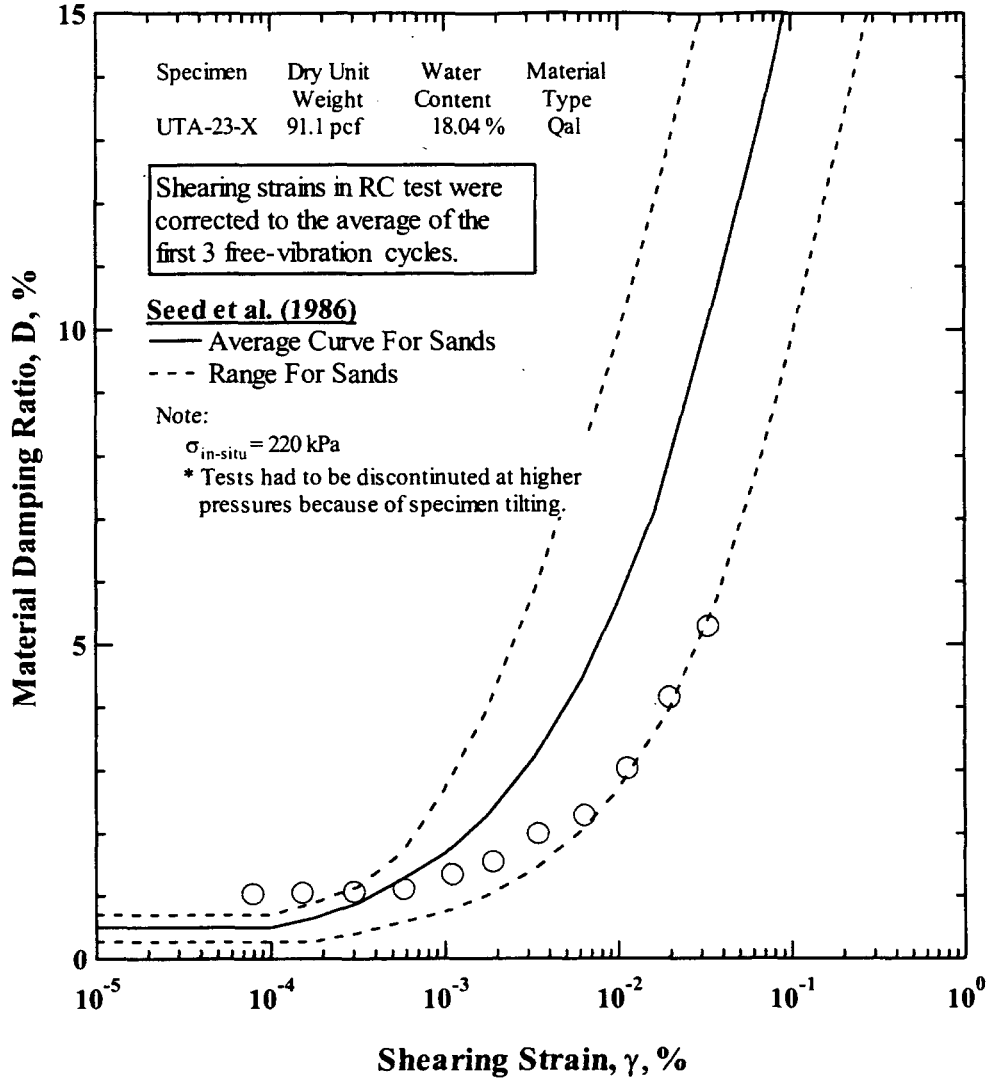

DTN: MO0203DHRSSWHB.001

Figure 143. Variation in Material Damping Ratio with Shearing Strain of Reconstituted Quaternary Alluvium Specimen

6.3 DATA ACQUIRED IN THE ESF MAIN DRIFT

6.3.1 Overview

SASW surveys were preformed in the ESF main drift tunnel and are discussed in Section 6.3.2. Samples were taken by coring into the tunnel wall; the results of laboratory RCTS tests on these samples are discussed in Section 6.3.3.

6.3.2 SASW Surveys

SASW surveys were performed in the ESF in July 2001 by UTA. A total of five surveys were performed along the north-south drift in the ESF (Figure 144). The purpose of these measurements was to provide information on the shear-wave velocity structure between the potential emplacement area and the crest of Yucca Mountain. As described later in Sections 6.4.2 and 6.4.3, SASW and downhole velocity surveys were performed on top of Yucca Mountain. However, data were only obtained to depths of about 700 ft and thus shear-wave velocity information was lacking for the depth range of 700 to 1,000 ft immediately above the emplacement area. To help constrain the deeper portion of the shear-wave velocity model, surveys were performed in the ESF.

6.3.2.1 Approach

Descriptions of the approach used in the SASW surveys are presented in Section 6.2.7.2 and in Section 6.4.2.1 and only differences from that approach are described below. Details of the investigations are described in Scientific Notebook SN-M&O-SCI-040-V1 (Wong 2002a).

Five locations along the main drift of the exploratory tunnel wall (rib) were surveyed using the SASW method. The five locations, denoted as T-1 through T-5, are shown on Figure 144. All surveys were performed on the west rib at a height of about 4 to 5 ft above the tunnel invert.

The sites were selected to represent a range in materials exposed along the main drift. T-1 and T-3 had highly fractured tuff at the surface. In addition, at T-1, the rock sounded "hollow" at many places along the rib. T-2, T-4, and T-5 exhibited much less fracturing, with T-2 showing only a few fractures over the maximum receiver spacing of 32 ft. It should be noted that there were locations where the rock was more fractured than at T-1 and T-3, but these sites were not surveyed due to time constraints and the increased difficulty in making measurements on fractured tuff. No area was surveyed where metal ground support was installed. Visually, such sites along the tunnel exhibited considerably more fracturing than any of the five SASW sites, which is consistent with the need for support.

Wilcoxon Model 736 accelerometers were used for receivers. They were coupled to the rock surface with magnets applied to nails inserted into drilled holes. Common receivers-midpoint geometry (Section 6.2.7.2) was used in the ESF. Receiver spacings of 6 inches and 1, 2, 4, 8, 16, and 32 ft were generally used. Various impact hammers ranging from a 4 oz. hammer to a 6 lb. sledgehammer were used to excite the surface wave energy along the tunnel wall.

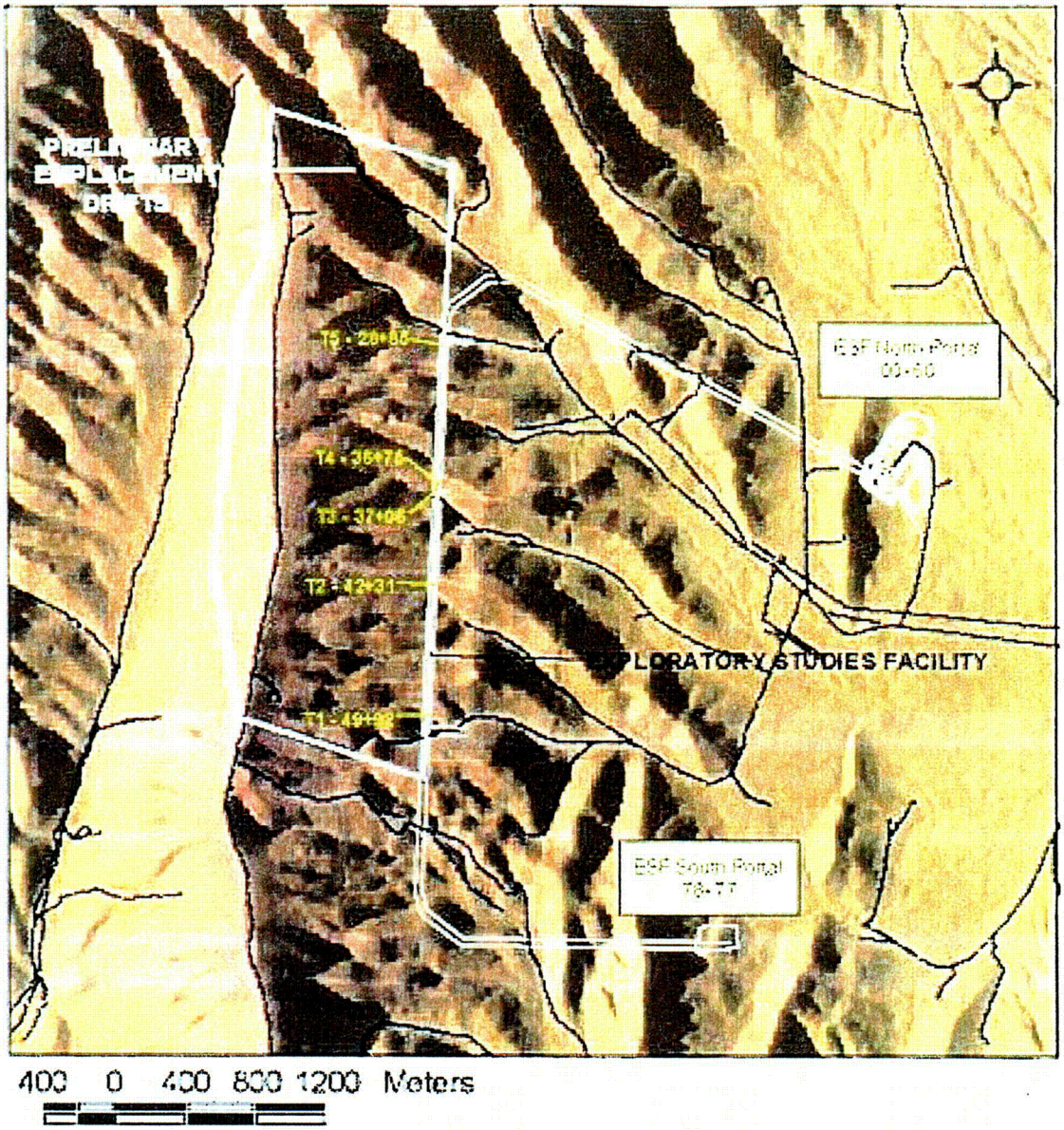

Source: Wong (2002a, Appendix 38, Figure 6)

Figure 144. Locations of SASW Surveys in the ESF

C02

6.3.2.2 Results

The shear-wave velocity profiles are shown on Figures 145 to 149. The dispersion curves are included in Attachment XIII. T-2 and T-5 show the highest shear-wave velocities (ranging from 6,000 to 7,000 ft/s) and these values begin within 0.5 ft of the exposed surface (Figures 146 and 149). T-3 and T-4 show a transitioning of shear-wave velocities from around 2,000 ft/s at the tunnel wall to values ranging from 5,100 to 6,250 ft/s at distances of 3 ft and greater into the tunnel wall (Figures 147 and 148). For T-3, T-4, and T-5, the low velocities at the shallow depths into the tunnel wall are probably due to the effects of fracturing from the tunneling process.

T-1 shows the most scatter in the dispersion curve, which is attributed to severe fracturing. As a result of the scattering, three dispersion curves (an upper-bound, a lower-bound, and an approximate mean curve) were fit to the data; hence the reason for the three profiles on Figure 145. The shear-wave velocity profiles at T-1 have the lowest velocities at distances of 3 ft and greater into the tunnel wall. Based on the test data, the fractured tuff at T-1 extends to at least 20 ft into the tunnel wall and has an average velocity of 3,500 ft/s (Figure 145).

Figure 150 shows all the shear-wave velocity profiles obtained in the ESF surveys and Figure 151 shows the mean, median, 16th and 84th percentile profiles for just T-2 to T-5. The SASW results in the tunnel demonstrate that the intact rock with few fractures exhibit shear-wave velocity values in the range of 6,000 to 7,000 ft/s. When the tuff is fractured near the tunnel walls, these values fall into the general range of 3,000 to 4,000 ft/s. Unfortunately, with the limited number of surveys, it is unlikely that the velocities of either the softest (highly fractured) tuff or the stiffest (unfractured) tuff were measured.

6.3.3 Geotechnical Laboratory Dynamic Testing

The dynamic properties of 5 tuff specimens from the North Portal area of the ESF were evaluated in the laboratory at the Geotechnical Engineering Center at the University of Texas at Austin using RCTS equipment. The procedures are described in Section 6.2.10.1. A detailed description of the testing is contained in Scientific Notebook SN-M&O-SCI-033-V1 (Wong 2002e). The results from the dynamic testing specimens are presented in this section. The specimens were taken from stratigraphic units that are also present beneath the WHB site (Table 23). Logistical constraints limited the collection sites to within 300 meters of the North Portal of the ESF.

6.3.3.1 Measurements

Five intact tuff specimens from the ESF (Figure 113) were dynamically tested. These specimens were constructed by carefully wet-coring specimens with a nominal diameter of either 1.56 in. (3.97 cm) or 2.48 in. (6.30 cm) from larger-diameter core samples. The same procedure was used to construct the intact tuff specimens from the WHB was used with these specimens (Section 6.2.10.2). The resulting height-to-diameter ratios ranged from about 2 to 3. The initial specimen properties are listed in Table 23. The test pressures and types of tests performed on the specimens are listed in Table 24.

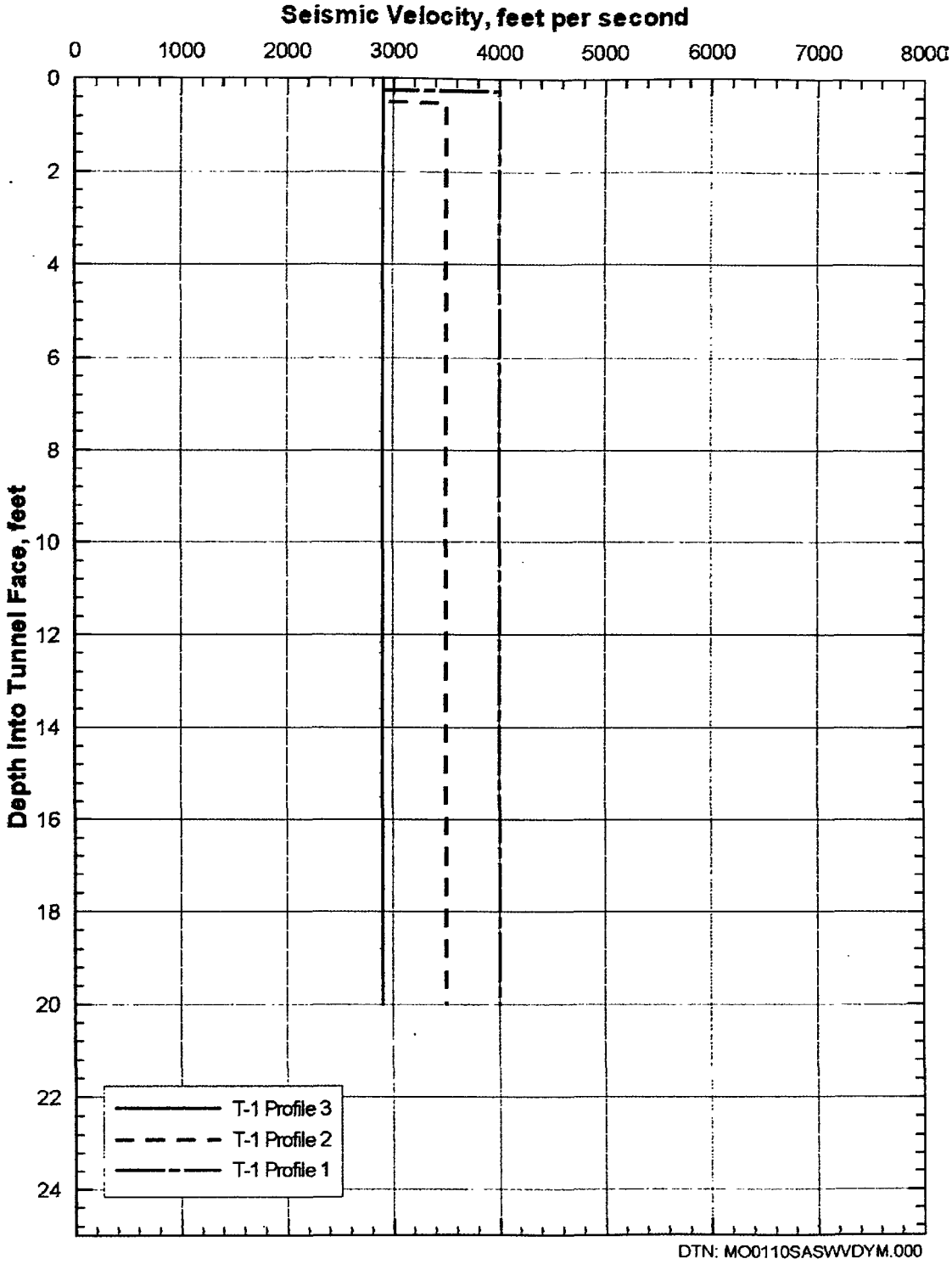

Figure 145. Shear-Wave Velocity Profiles from SASW T-1

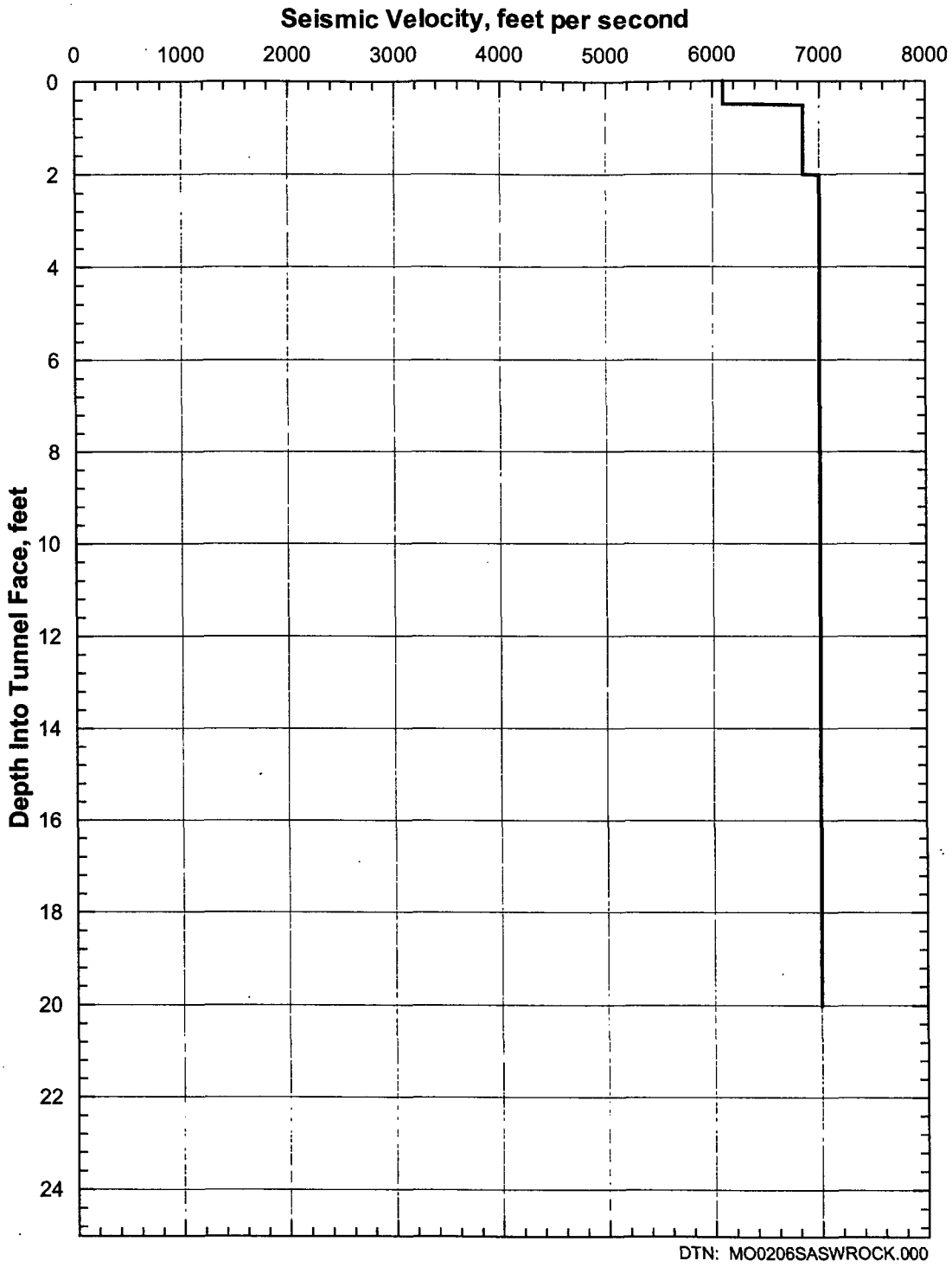

Figure 146. Shear-Wave Velocity Profile from SASW T-2

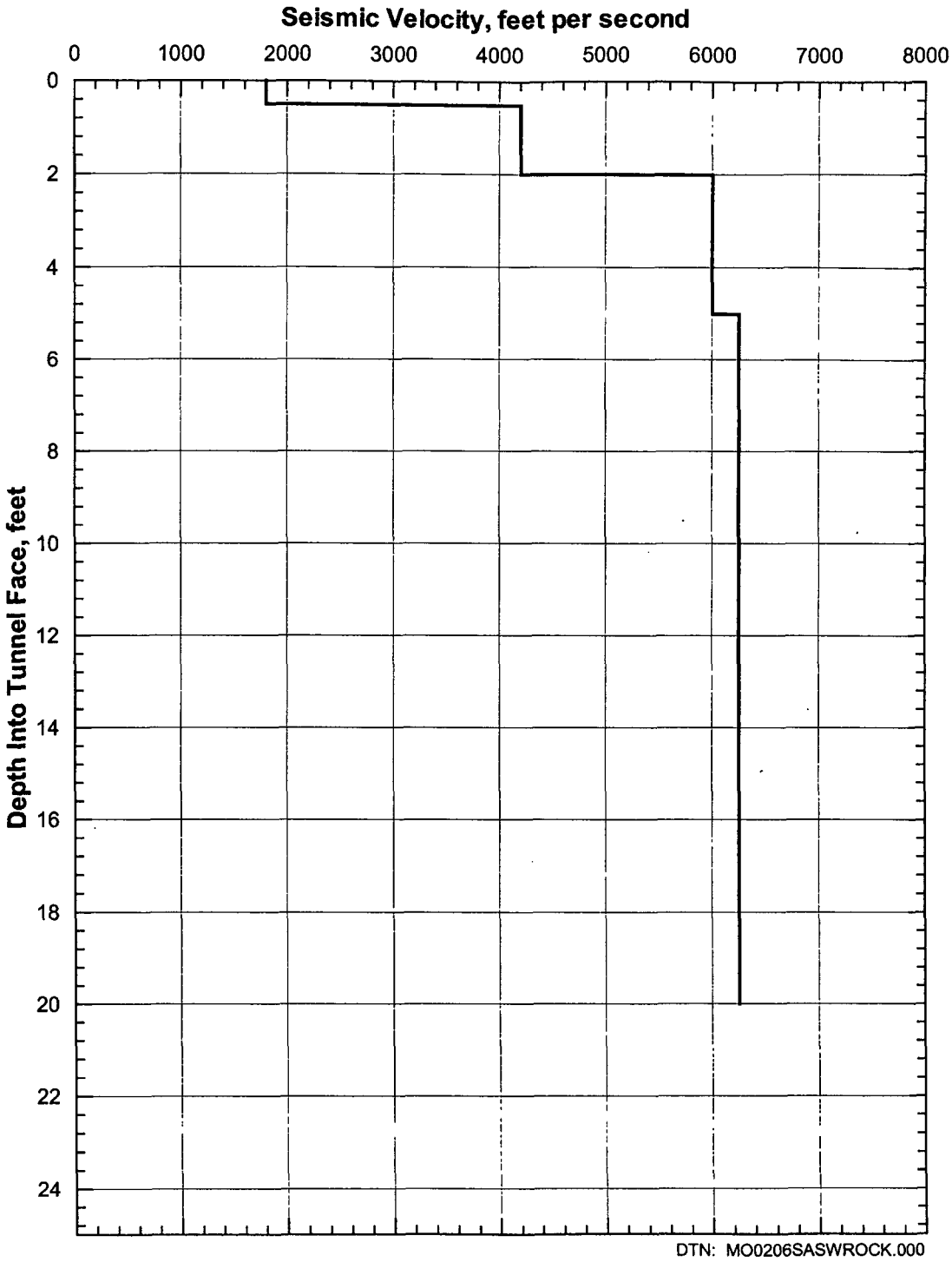

Figure 147. Shear-Wave Velocity Profile from SASW T-3

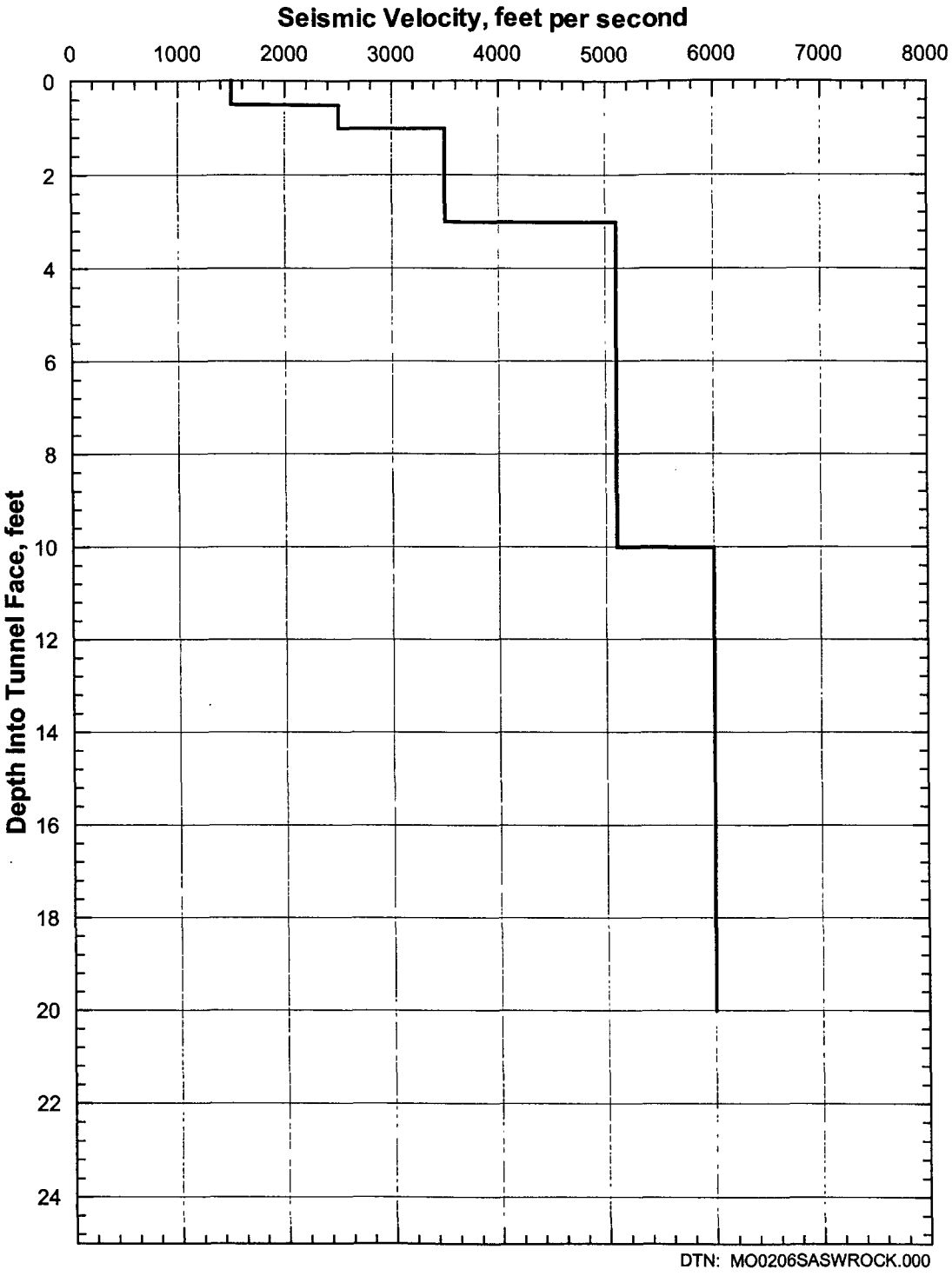

Figure 148. Shear-Wave Velocity Profile from SASW T-4

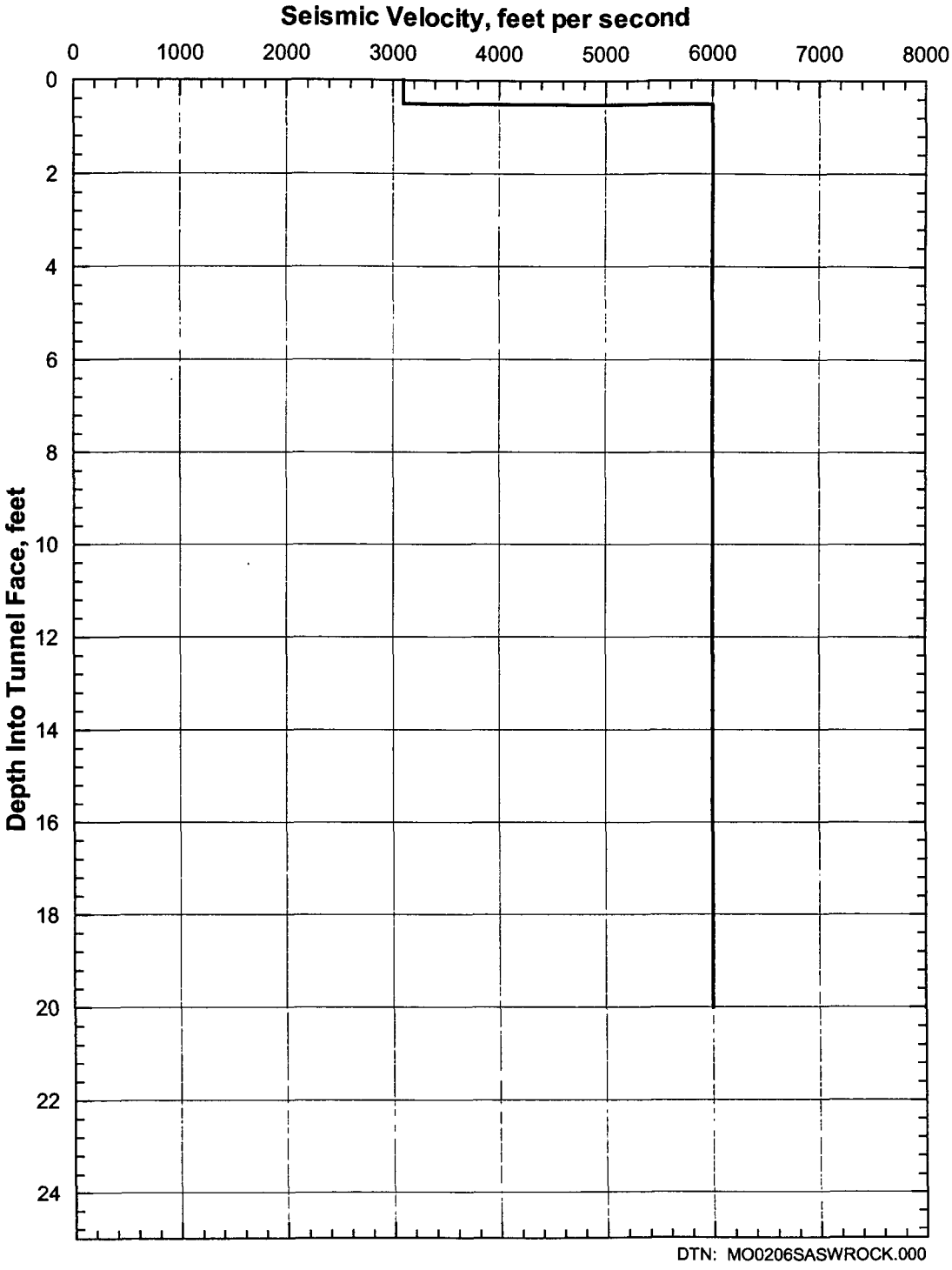

Figure 149. Shear-Wave Velocity Profile from SASW T-5

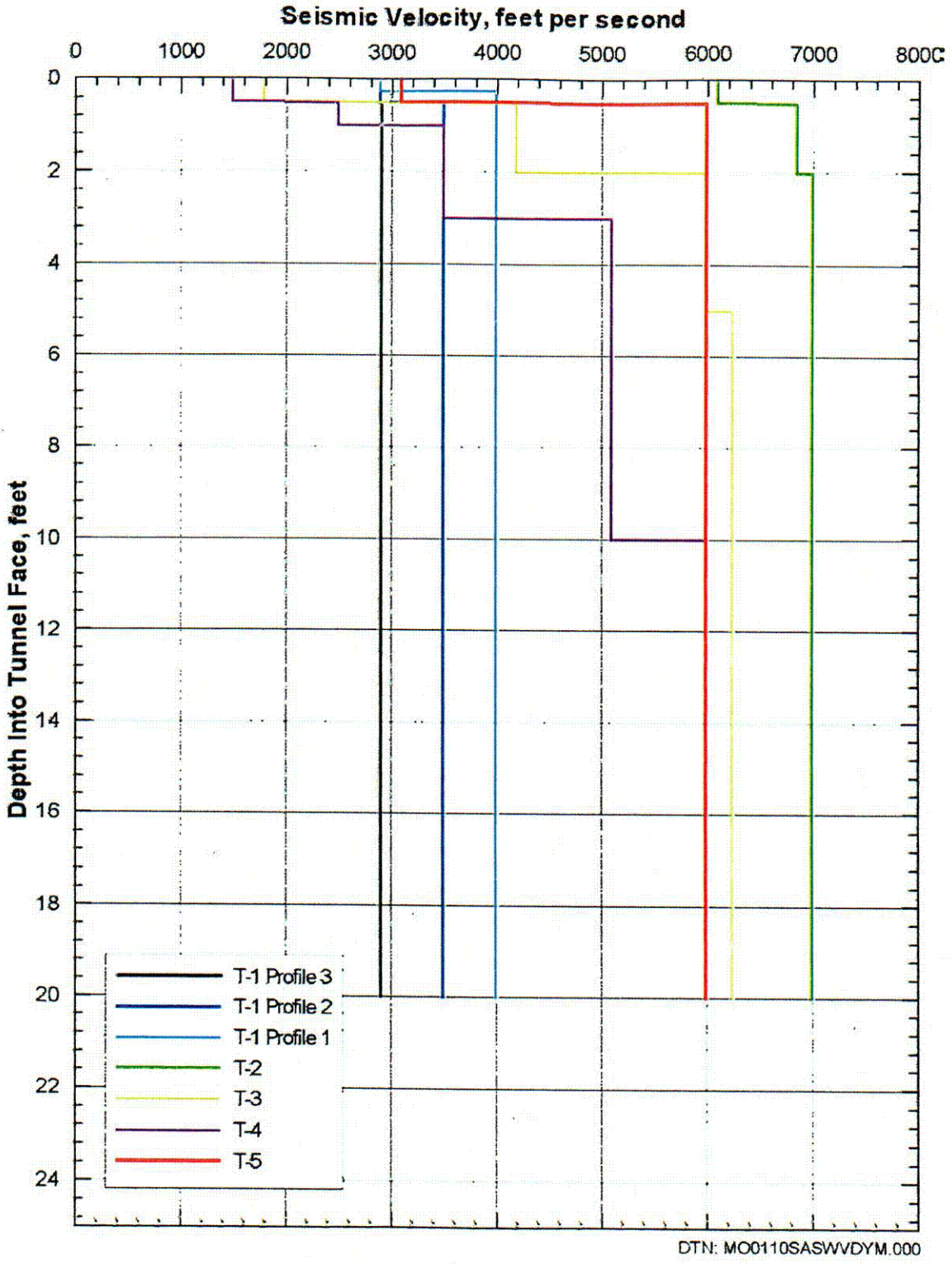

Figure 150. Shear-Wave Velocity Profiles from SASW Measurements in ESF

C03

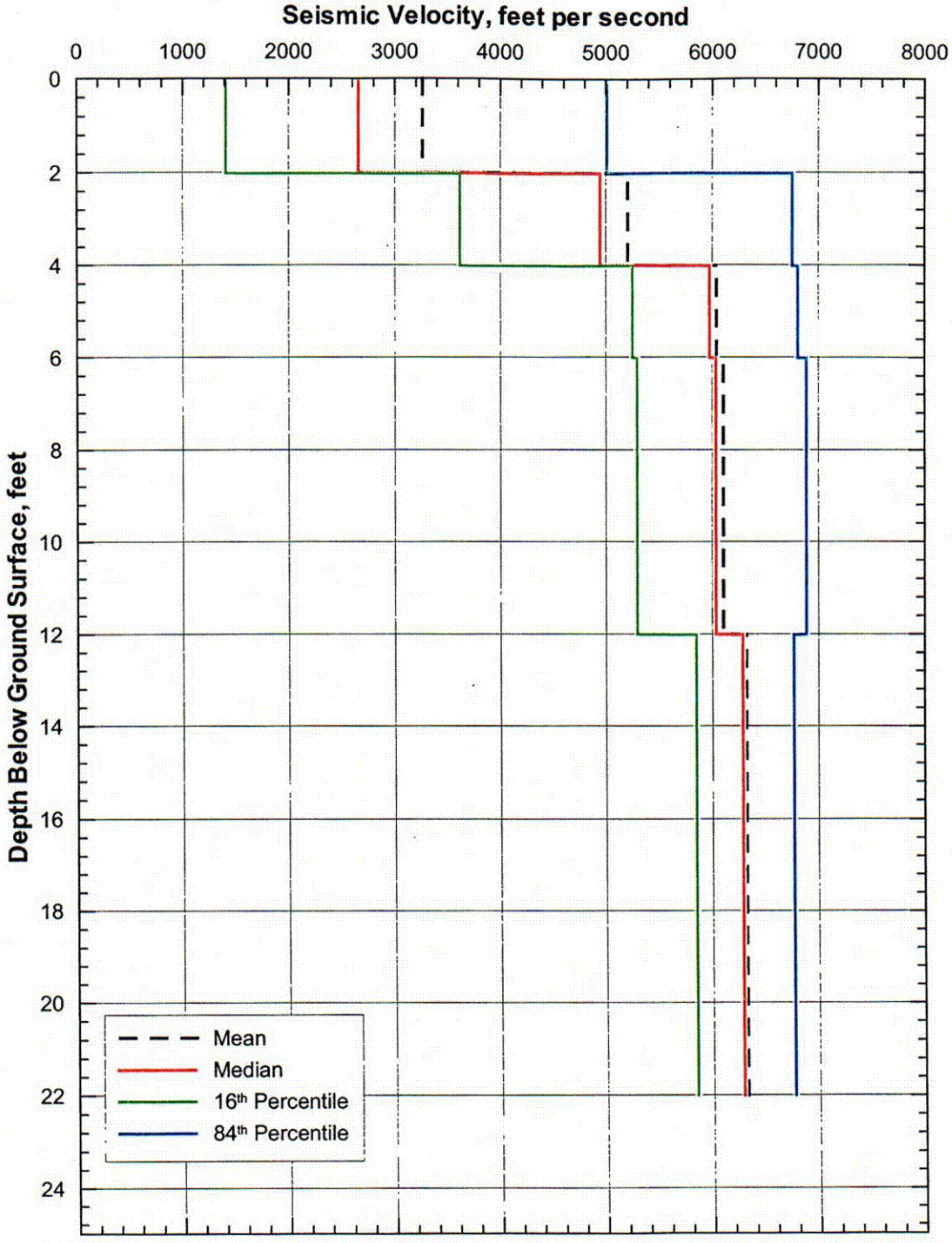

Note: These statistics have been calculated for illustrative purposes only. Final statistics calculated for use in the forthcoming scientific analysis entitled *Development of Seismic Design Input Ground Motions for a Geologic Repository at Yucca Mountain* will be submitted to the TDMS.

Figure 151. Statistical Analyses of Shear-Wave Velocity Profiles from SASW Measurements in ESF

C04

Table 23. Initial Properties of Intact Tuff Specimens from the ESF

UTACED Designation	SMF Designation	Location	Depth (ft)	Lithostratigraphic Unit	Height[a] (cm)	Diameter[a] (cm)	Total Mass[a] (g)	Water Content[a] (%)	Dry Unit Weight (pcf)	Total Unit Weight[a] (pcf)
UTA-20-F	01011666	ESF-Geotek#3	4.5	Tpki	11.55	3.95	170.3	6.69	70.4	75.1
UTA-20-G	01011668	ESF-Geotek#3	6.5	Tpki	11.50	3.96	182.1	13.90	70.5	80.3
UTA-20-I	00564008	SPC-564008	0.5	Tpcrv	11.58	3.96	290.6	0.96	125.8	127.0
UTA-20-J	00564000	SPC-564000	0.5	Tmbt1	11.43	3.95	248.6	4.36	106.2	110.8
UTA-20-L	00564005	SPC-564005	0.5	Tpki	12.75	6.30	499.4	1.64	77.1	78.4

Sources DTN: MO0203DHRSSWHB.001, [a] Wong (2002e, Appendix 42, page 17)

Table 24. Confining Pressures at which RCTS Tests Were Performed on the Intact Tuff Specimens from the ESF

UTACED Designation	SMF Designation	Depth (ft)	Lithostratigraphic Unit	Estimated Mean Total Stress (psi)	Low-Amplitude RC Test Pressures (psi)	High-Amplitude RC Test Pressures (psi)	Low- and High-Amplitude TS Test Pressures (psi)
UTA-20-F	01011666	4.5	Tpki	2.4	0, 0.6, 1.2, 2.4	2.4	2.4
UTA-20-G	01011668	6.5	Tpki	4	0, 1, 2, 4	4	4
UTA-20-I	00564008	0.5	Tpcrv	10	0, 3, 5, 10, 20, 40, 80	10, 40	10, 40
UTA-20-J	00564000	0.5	Tmbt1	10	0, 3, 5, 10, 20, 40, 80, 160	10, 40	10, 40
UTA-20-L	00564005	0.5	Tpki	10	0, 3, 5, 10, 20, 40, 80, 160	10, 40	10, 40

Source: Wong (2002e, Appendix 42, page 20)

6.3.3.2 Results

The effects of normalized confining pressure on G_{max} and D_{min} of the 5 ESF specimens are presented in Figures 152 and 153, respectively. In general, the small-strain behavior of the tuff is quite similar to that of the tuff from the WHB area. The effects of f on G_{max} and D_{min} are small (Figures XIV-6 and XIV-7).

The effects of γ on G, G/G_{max} and D are shown in Figures 154 to 156, respectively. The main differences between the ESF tuffs and those from the WHB site are that two ESF specimens show more nonlinearity in their G/G_{max} versus log γ relationship (UTA-20-I and UTA-20-L in Figure 155) and one specimen (UTA-20-I) shows relatively large values of D at $\gamma > 10^{-3}\%$ (Figure 156). These differences are thought to likely be attributed to the very shallow depths behind the tunnel wall from which the specimens in the ESF were taken where disturbance from the tunnel boring process is likely to be significant and the likelihood of micro-cracking in the specimens.

6.4 DATA ACQUIRED AT THE CREST OF YUCCA MOUNTAIN

6.4.1 Overview

In the computation of preliminary seismic design ground motions, best-estimate, lower- and upper-bound velocity profiles were estimated based on Vertical Seismic Profiling (VSP) surveys performed at six boreholes (Daley et al. 1994). Only one borehole, SD-12, was within the surface projection of the potential emplacement area as defined in July 2001 (Figure 157). This borehole was located at the eastern boundary of the emplacement block. Thus, an adequate characterization of the seismic velocities of the block and their variability was not available. To obtain velocity information, a program of shallow downhole velocity measurements and SASW surveys along the Yucca Mountain crest and downslope (east) were undertaken in the summers of 2000 and 2001. The following describes the approaches and results of those surveys.

6.4.2 SASW Surveys

SASW surveys were performed on the top of Yucca Mountain generally above the potential emplacement area in the summers of 2000 and 2001 by UTA. In the first phase, SASW surveys were performed from 12 to 15 September 2000. The goal of these measurements was to determine the shear-wave velocity structure to depths of approximately 500 to 700 ft at several locations beneath the crest of Yucca Mountain. In total, 7 SASW surveys were carried out along the crest and these are designated with a "C" (e.g., C-1) (these lines were also referred to at one time as "CYM", including in some of the data sets).

In June and July 2001, additional SASW measurements were made at 26 locations along the crest of Yucca Mountain as well as downslope to the east of the crest. Twelve of these surveys were performed to obtain shear-wave velocity profiles to depths of 150 to 200 ft. These SASW tests are designated in this report with an "S" to represent relatively shallow profiling depths (S-1 to S-12). Eleven surveys were performed to obtain profiles to depths of 400 ft or greater, where spatial access was not limited. These surveys are designated with the letter "D" (D-1 to D-11) to represent relatively deep profiling depths (survey D-12 is discussed in Section 6.2.7).

In addition to the C, S, and the D surveys, 3 sets of SASW measurements were performed on the surface of exposed rock at the crest. These tests are designated with the letter "R" for rock and are referred to as R-1, R-2, and R-3 herein. This section describes the SASW measurements, analysis procedures, and the results of the SASW surveys at the top of Yucca Mountain.

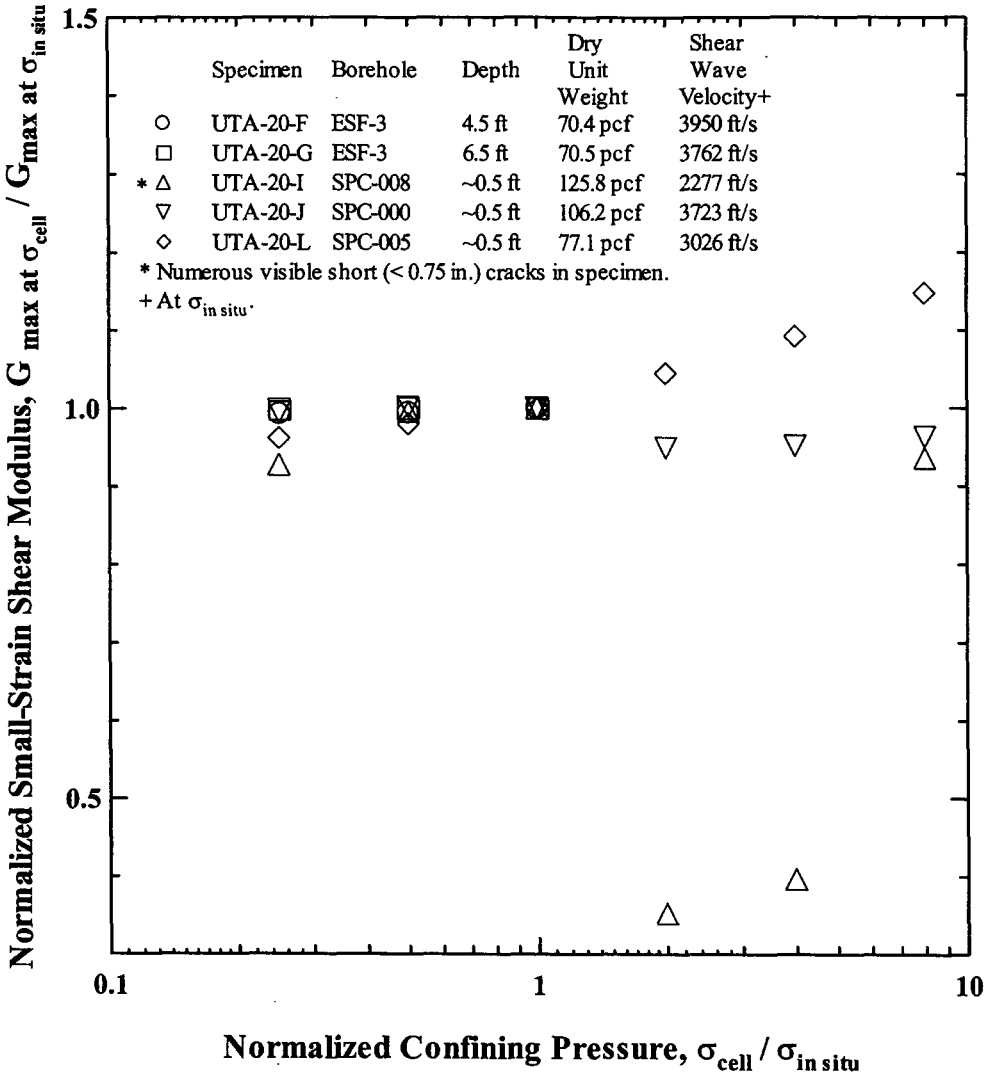

Source: Wong (2002e, Appendix 42, page 54)

Figure 152. Variation in Normalized Small-Strain Shear Modulus with Normalized Confining Pressure of Intact Tuff Specimens from the ESF

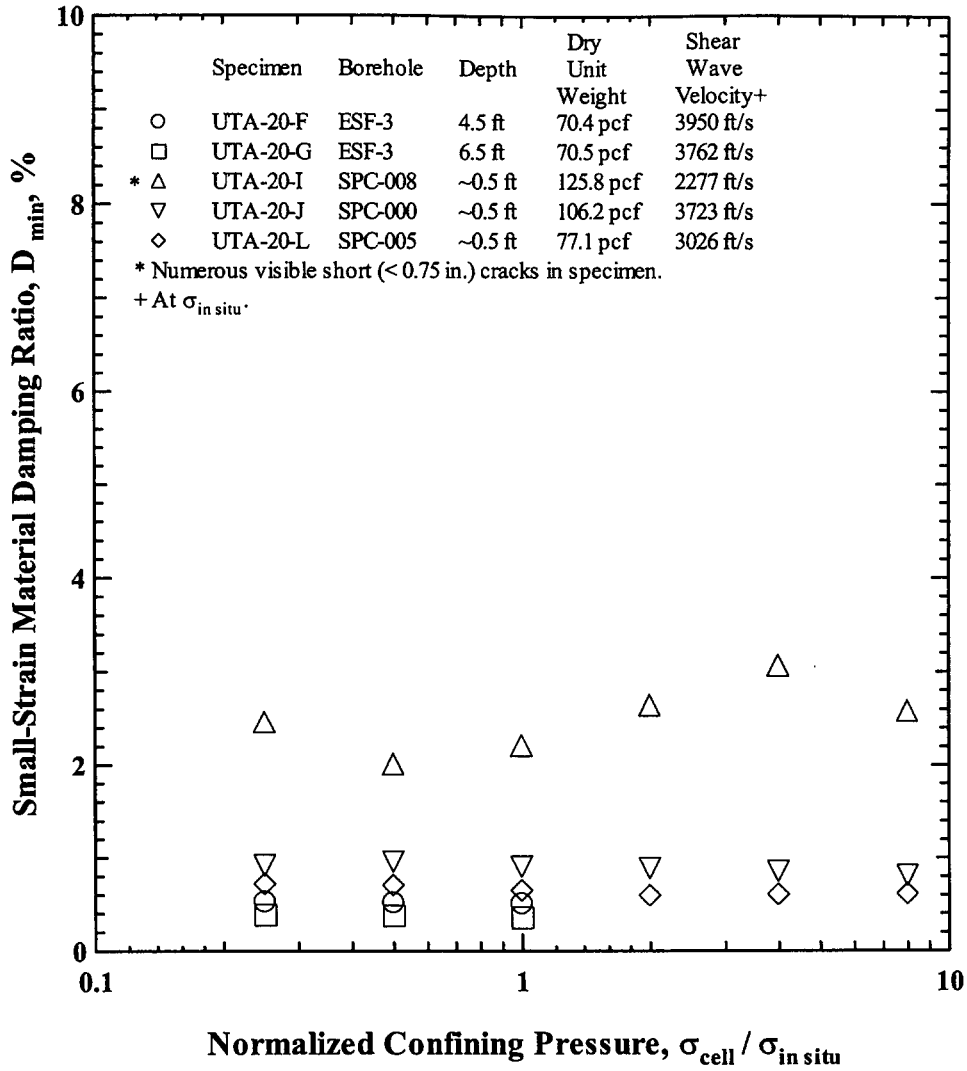

Source: Wong (2002e, Appendix 42, page 55)

Figure 153. Variation in Small-Strain Material Damping Ratio with Normalized Confining Pressure of Intact Tuff Specimens from the ESF

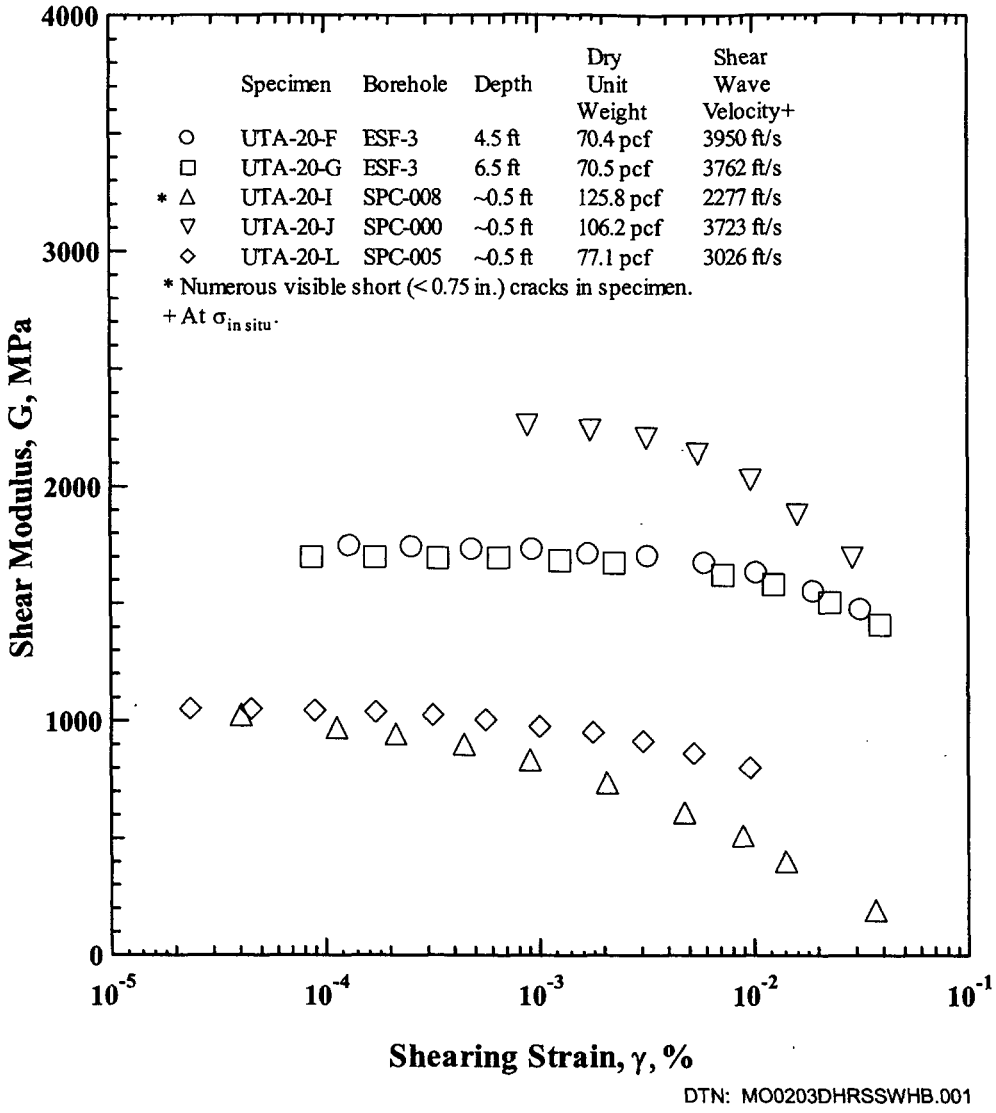

Figure 154. Variation in Shear Modulus with Shearing Strain of Intact Tuff Specimens from the ESF

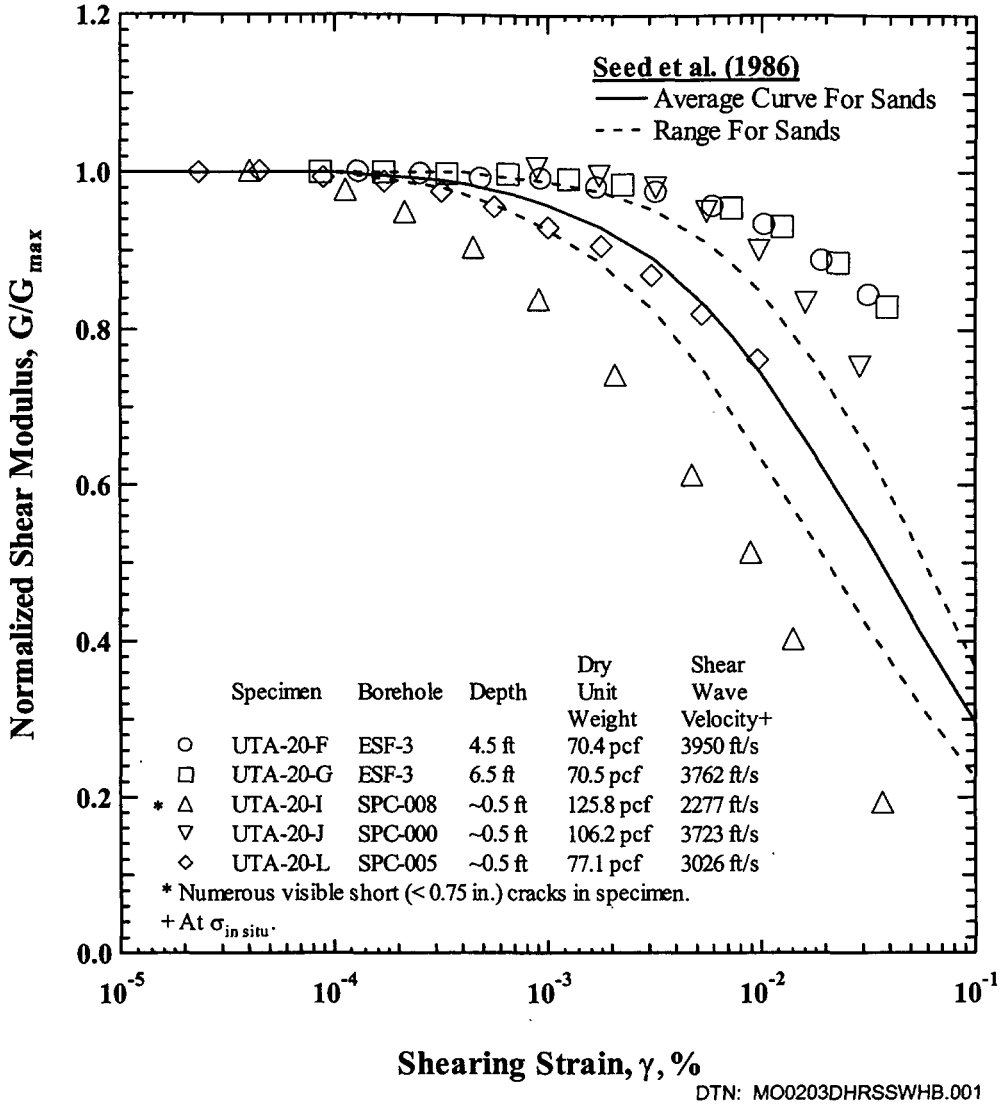

Figure 155. Variation in Normalized Shear Modulus with Shearing Strain of Intact Tuff Specimens from the ESF

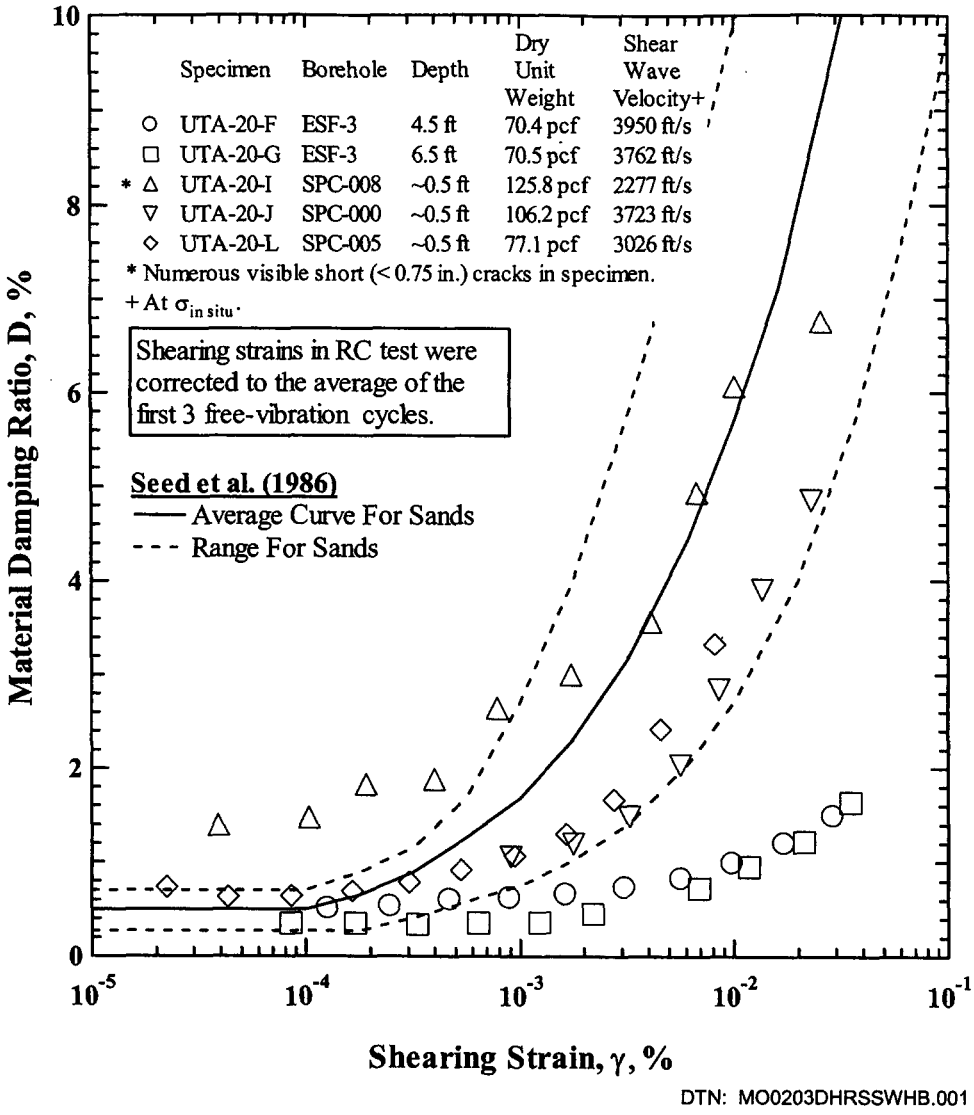

DTN: MO0203DHRSSWHB.001

Figure 156. Variation in Material Damping Ratio with Shearing Strain of Intact Tuff Specimens from the ESF

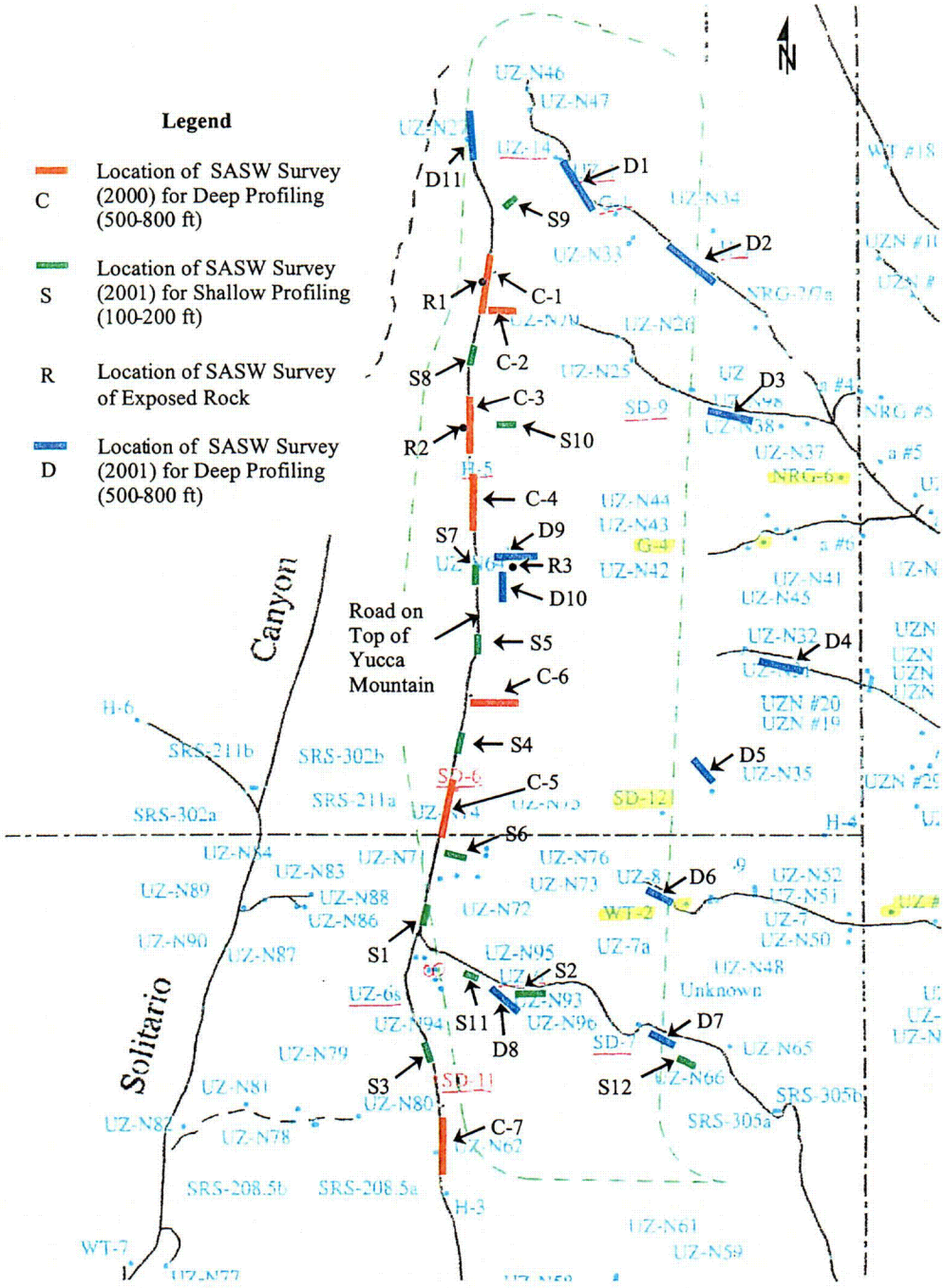

Note: Dashed green line shows the emplacement area proposed as of July 2000. Boreholes used for VSP are highlighted in yellow. From Wong (2002a, Appendix 38, page 28)

Figure 157. Locations of Boreholes Used for Vertical Seismic Profiling Surveys and SASW Surveys at Yucca Mountain.

C05

6.4.2.1 Approach

A total of 33 SASW surveys were performed on top of Yucca Mountain generally above the potential emplacement area. The locations of these surveys are shown on Figure 157. The lengths of the lines as shown on Figure 157 are approximately equal to the maximum receiver spacing along the survey. The locations of these surveys referenced to other landmarks are presented in Scientific Notebooks SN-M&O-SCI-023-V1 (Wong 2002d) and SN-M&O-SCI-040-V1 (Wong 2002a). A general description of the approach used in the SASW surveys is contained in Section 6.2.7.2 and only differences in that approach are described below.

To cover the broad range in frequencies required for the SASW measurements over the wide range of sites, three different sources were utilized. Impact hammers were used to generate higher-frequency surface waves. At the shortest receiver spacings (typically 3 ft), a small, hand-held geology hammer was used to impact the ground. At larger receiver spacings (typically 6, 12, and 25 ft), a sledgehammer was employed. At the R sites, a small ball-peen hammer was used to excite the surface wave energy.

For receiver spacings equal to and greater than 25 ft at the S sites, a bulldozer was used to excite surface wave energy. Similarly at the D sites, a Vibroseis truck was used to excite the necessary frequencies (Figure 158). Figure 159 shows the Vibroseis truck performing a SASW survey with the receivers (shown in foreground) running downslope of the Yucca Mountain crest. The Vibroseis truck can excite energy at frequencies below those excited by a bulldozer source and can, therefore, be used to obtain profiles to greater depths.

A common receivers-midpoint geometry was employed whenever it was possible (Section 6.2.7.2). In some cases (e.g., SASW D-10), space and access limitations did not allow for a common receivers-midpoint geometry to be used at all spacings. These cases are noted in the scientific notebooks. Additionally, at each spacing, SASW measurements are ideally performed with the source located first on one end of the survey and then repeated with the source moved to the opposite end of the survey (termed forward and reverse directions). If good quality data are recorded in both directions, the cross-power spectra can be combined to eliminate any differences in receiver phase shifts or receiver coupling. At most locations, surveys were performed in only one direction at spacings greater than 25 ft due to the space and time limitations of moving the low-frequency source (bulldozer or Vibroseis truck) back and forth around the receiver alignment. Moving and replacing the receivers to allow the source to pass from one end of the survey to the other would change the coupling and defeat the purpose of performing forward and reverse tests. At the shorter spacings (< 25 ft) where impact hammers were used as the source, the test was performed in both the forward and reverse directions.

The SASW surveys oriented downslope of the crest could not be performed in both directions due to the restrictions on moving the Vibroseis truck into undisturbed areas. Performing the survey in only one direction had an insignificant impact on the results in these cases because the receivers had already been shown to be well matched, and any differences in receiver-to-ground coupling were insignificant.

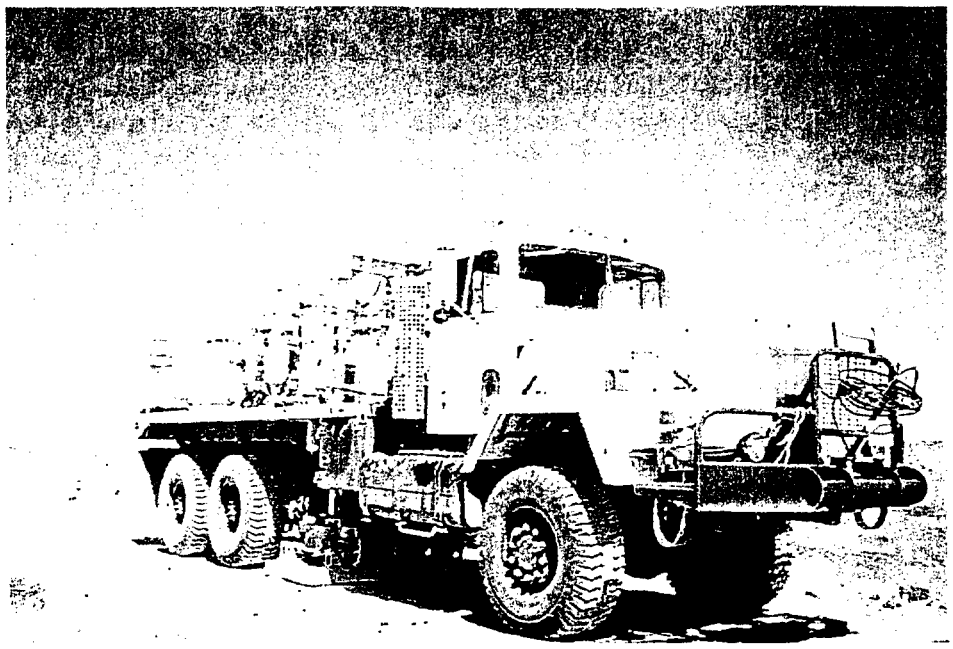

Figure 158. Photograph of Vibroseis Truck in Operation on the Crest of Yucca Mountain

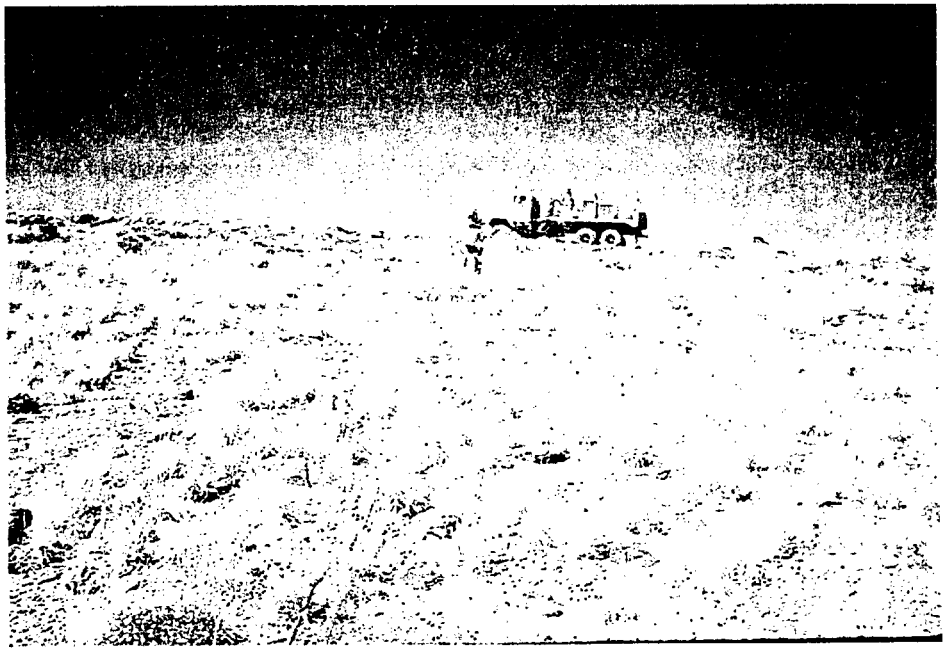

Figure 159. Photograph of SASW Survey Going Downslope with the Vibroseis Truck Being Readied for Use as the Source

SASW measurements were performed using a sequence of increasing spacings. Distances between receivers of 3, 6, 12, 25, 50, 100, and 200 ft were typically used. At the C and D sites, additional receiver spacings of 400, 600, and 800 ft were used when space considerations allowed. This number and progression of receiver spacings resulted in extensive overlapping of individual dispersion curves used to develop the composite field curve, which enhanced the measurement reliability. At the R sites, only two receiver spacings of typically 6 inches and 1 ft were used. The exact receiver spacings used at all of the SASW sites can be found on the data sheets presented in the Supplemental Records to Scientific Notebooks SN-M&O-SCI-023-V1 (Wong 2002d) and SN-M&O-SCI-040-V1 (Wong 2002a).

The SASW surveys with the Vibroseis truck were performed in a swept-sine mode where the source signal was swept over the frequencies of interest, and the relative phase and coherence were determined at each frequency. The source output of the Hewlett-Packard Dynamic Signal Analyzer was used to control the vibration frequency and amplitude of the Vibroseis truck. This process also allowed the operator to subjectively evaluate the data being collected in the field to assure consistency with the expected Rayleigh wave propagation in a layered halfspace.

For the surveys performed with impact hammers and the bulldozer, several time records were collected and averaged in the frequency domain to compute the phase and coherence functions. Typically, 3 to 5 measurements were averaged for the hammer measurements, and 10 to 20 measurements were averaged for the bulldozer surveys. For the measurements performed with the Vibroseis truck, the spectral functions were determined one frequency at a time in a swept-sine fashion. The number of averages and integration time was adjusted in the field to control how long the source remained at each frequency. Typically, 3 to 5 averages were used at each frequency in the determination of the spectral functions when the Vibroseis was used. All of the phase plots that were used in the interpretation of the data are presented in the Supplemental Records to Scientific Notebooks SN-M&O-SCI-023-V1 (Wong 2002d) and SN-M&O-SCI-040-V1 (Wong 2002a). The wrapped phase spectrum and coherence function from one receiver spacing are shown on Figure 160 as an example. These data were collected from the 400-ft receiver spacing recorded at D-2.

6.4.2.2 Results

All shear-wave velocity profiles are shown on Figures 161 through 191 and values are listed in Attachment XV. Of the 33 SASW surveys performed on Yucca Mountain, 22 were on or very near the crest of Yucca Mountain (Figure 157). Surveys C-2, C-6, D-6, and D-11 resulted in dispersion curves that indicated significant lateral variability. Thus at these sites, multiple shear-wave velocity profiles were estimated to reflect the variability over the distance of the survey. A total of 38 profiles are shown in composite on Figure 192 (R surveys not shown). The median, mean, and 16^{th} and 84^{th} percentile profiles are shown on Figure 193. Also shown is the base case tuff velocity model developed in 1999 (DTN: MO98PRECLOSURE.000).

Examination of the individual shear-wave velocity profiles suggests that unlike the typical increase in velocity with depth observed in most geologic settings, many of the profiles indicate low-velocity zones beneath higher velocity rock, which are often observed in volcanic terrain (Wong et al. 1995, pages 6-15 to 6-20). The limited shallow downhole shear-wave velocity data are consistent with the presence of these zones (Section 6.4.3).

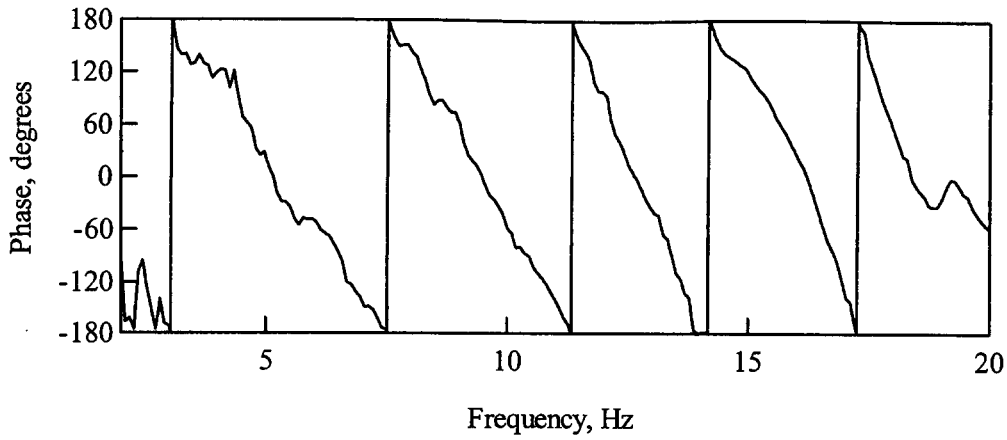

a. Cross-Power Spectrum

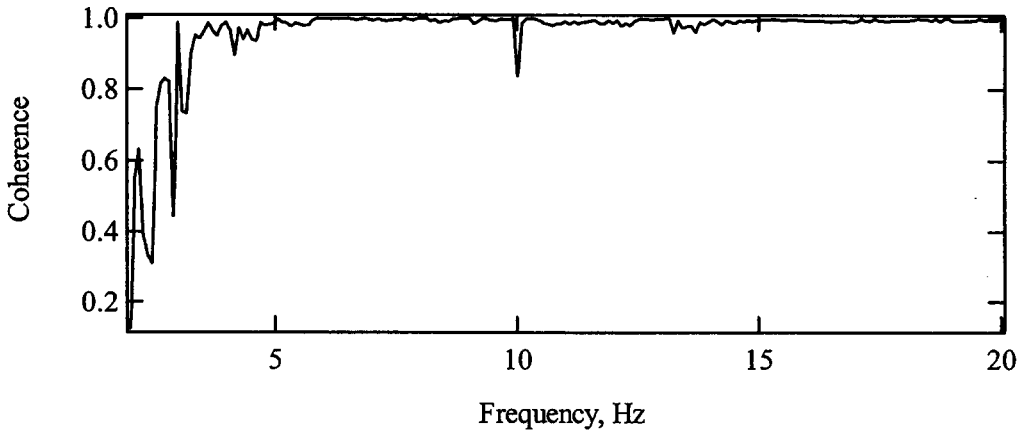

b. Coherence Function

Source: Wong (2002a, Appendix 37)

Figure 160. Cross-Power Spectrum and Coherence Function Measured at Site D-2 from the 400-ft Receiver Spacing

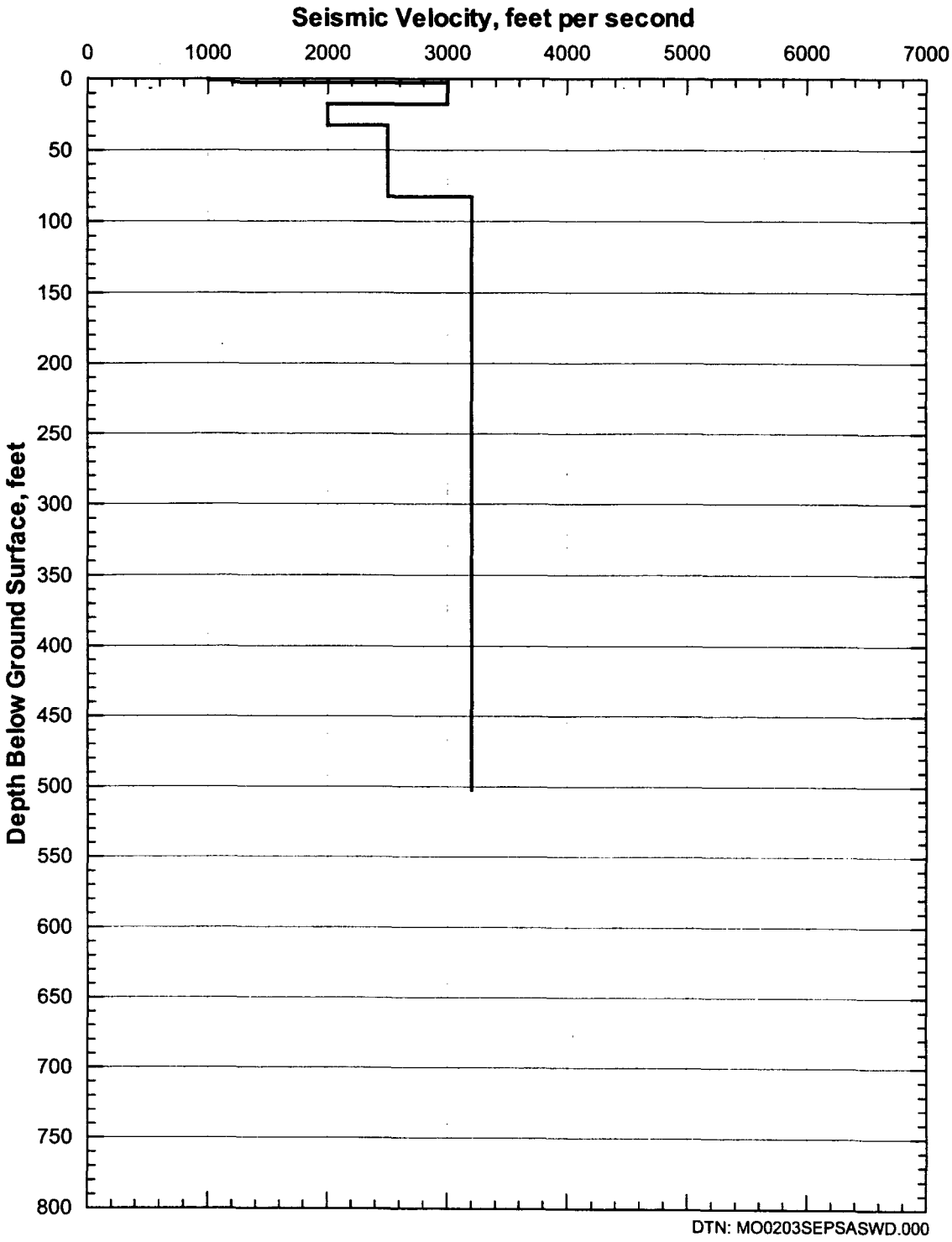

Figure 161. Shear-Wave Velocity Profile from SASW C-1

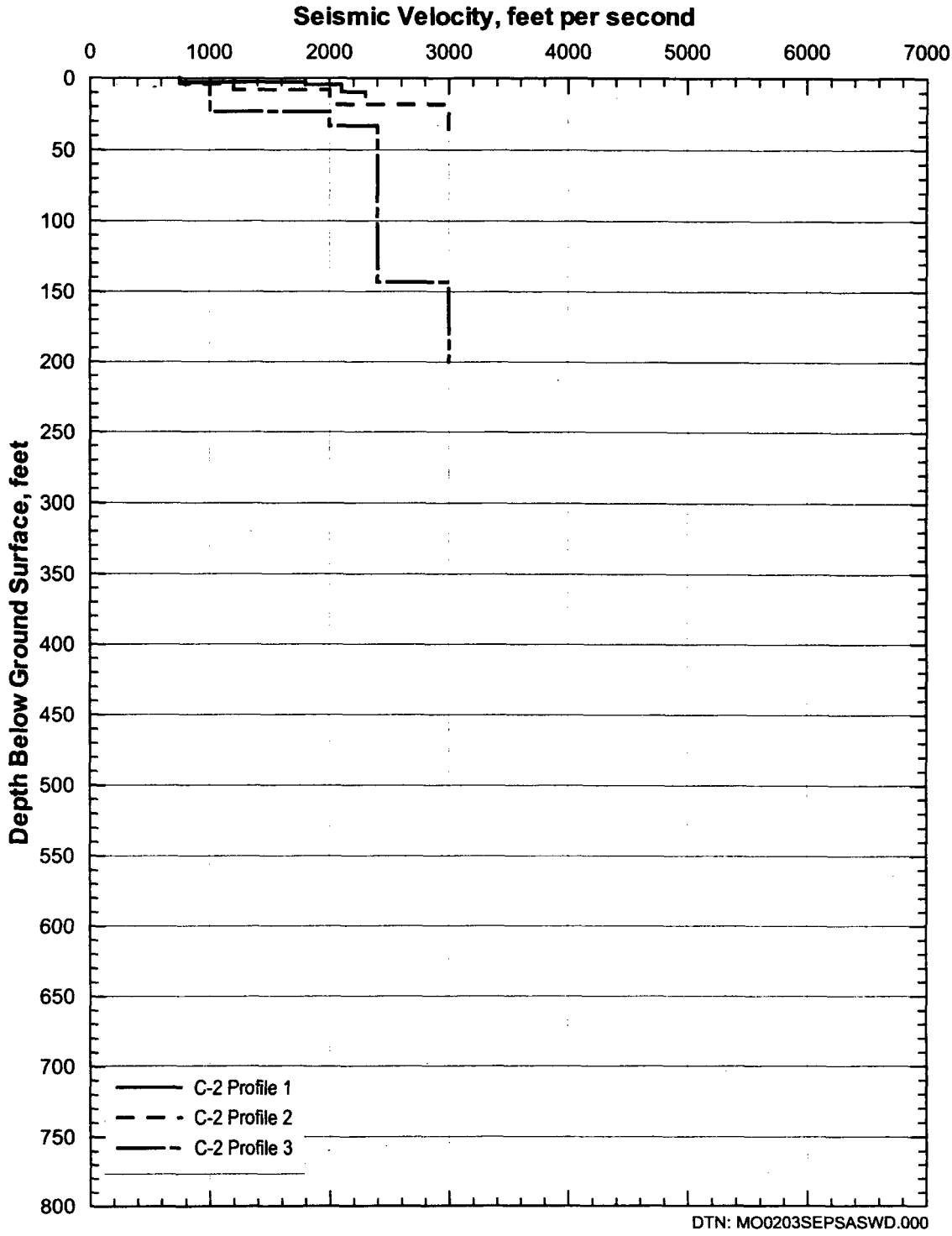

Figure 162. Shear-Wave Velocity Profiles from SASW C-2

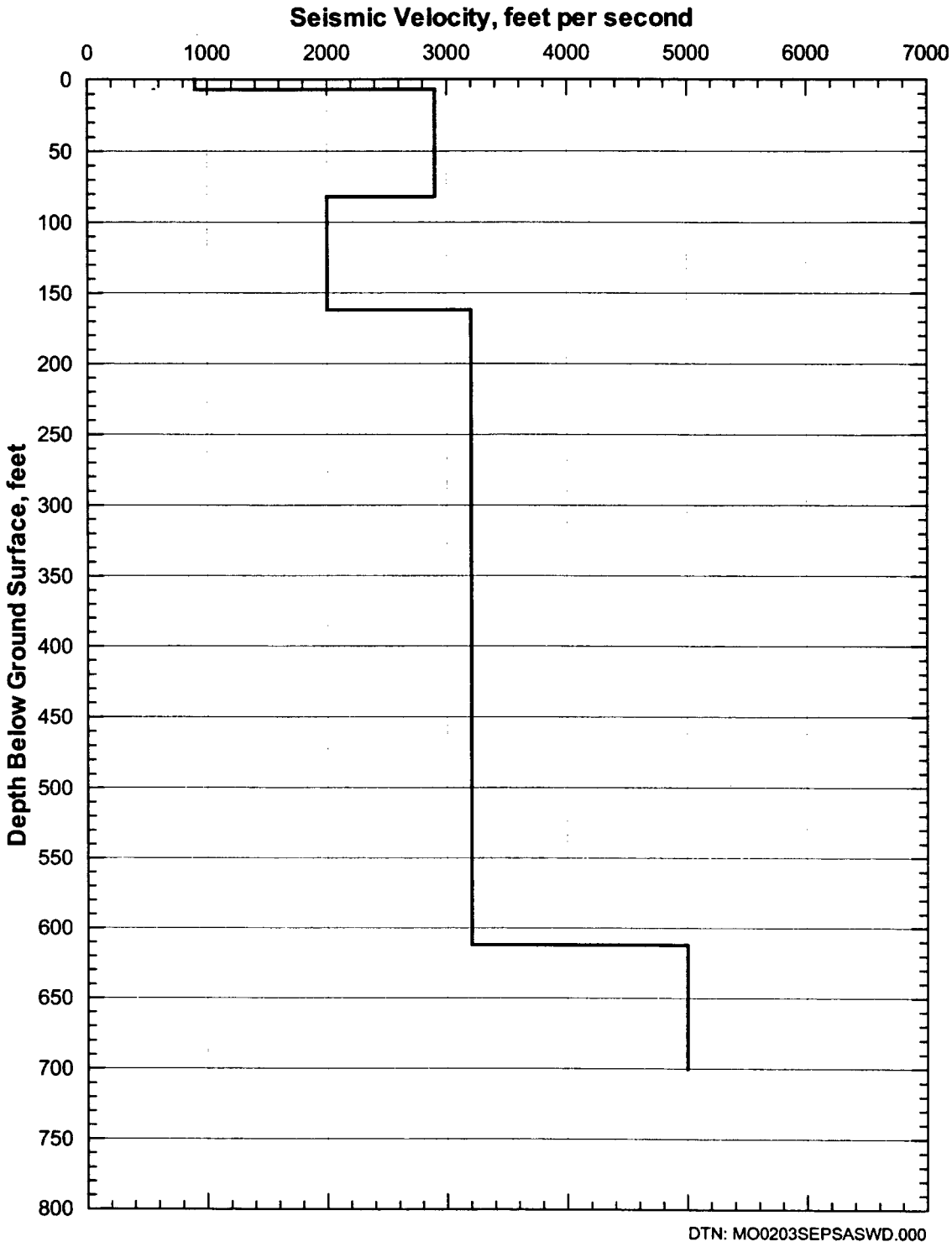

Figure 163. Shear-Wave Velocity Profile from SASW C-3

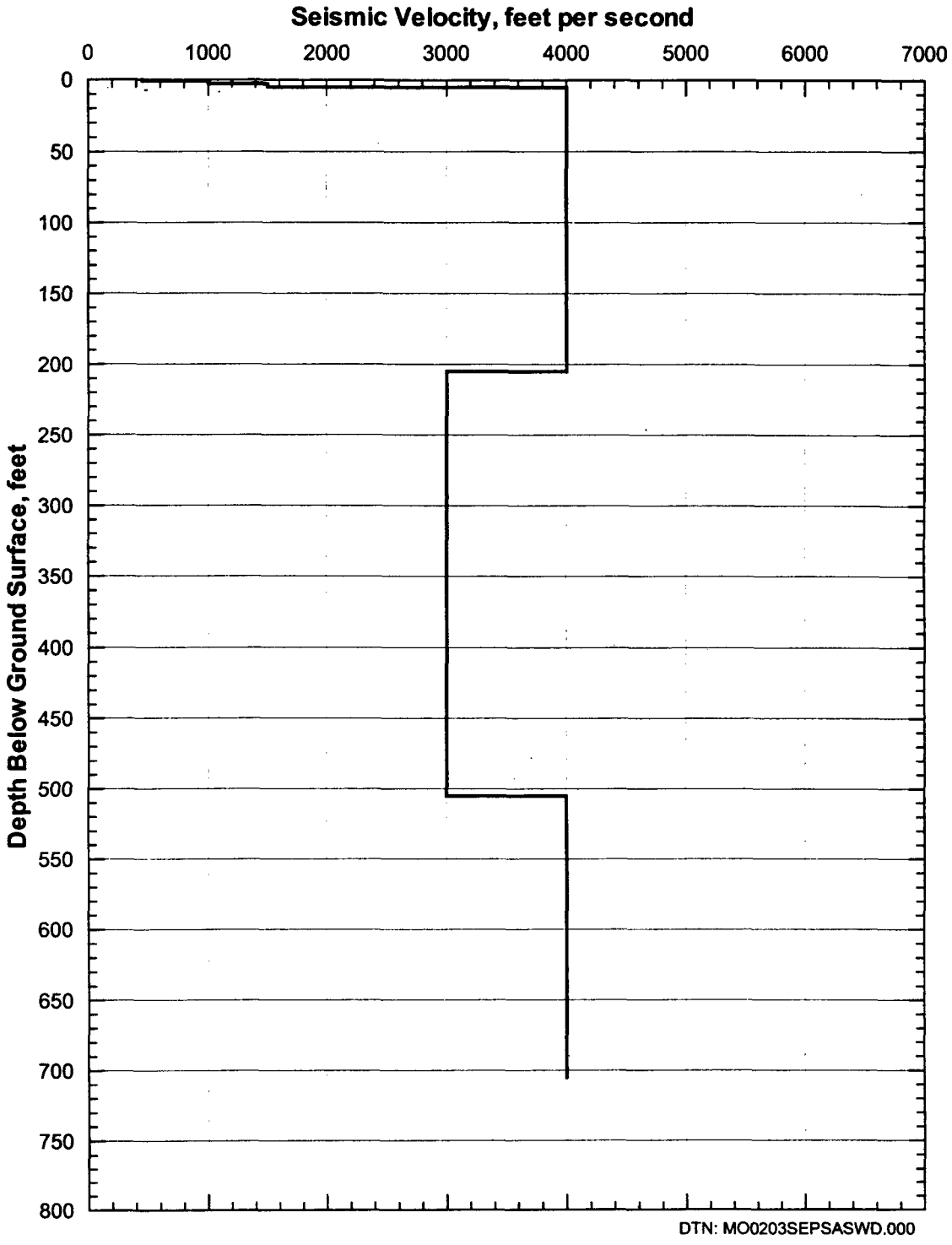

Figure 164. Shear-Wave Velocity Profile from SASW C-4

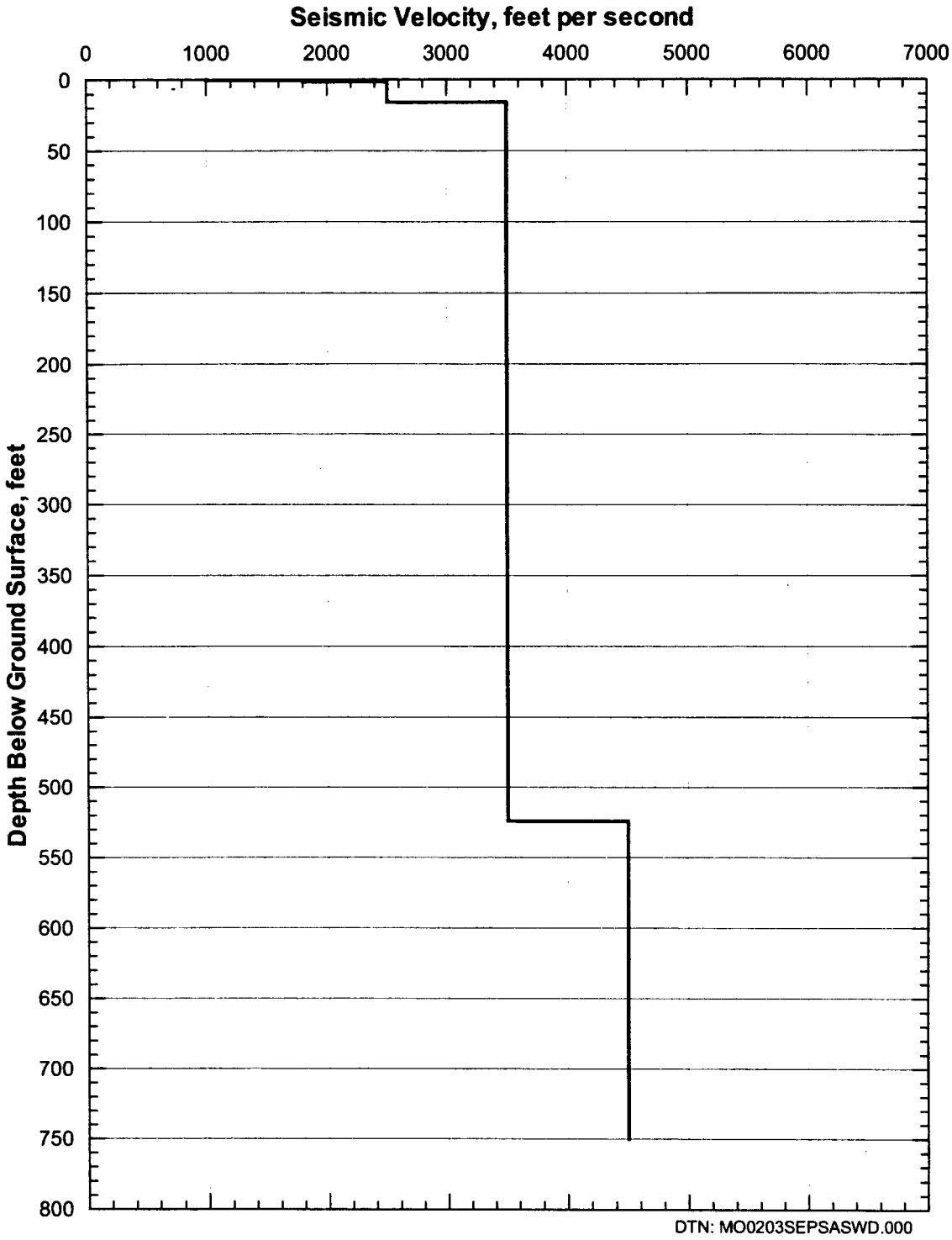

Figure 165. Shear-Wave Velocity Profile from SASW C-5

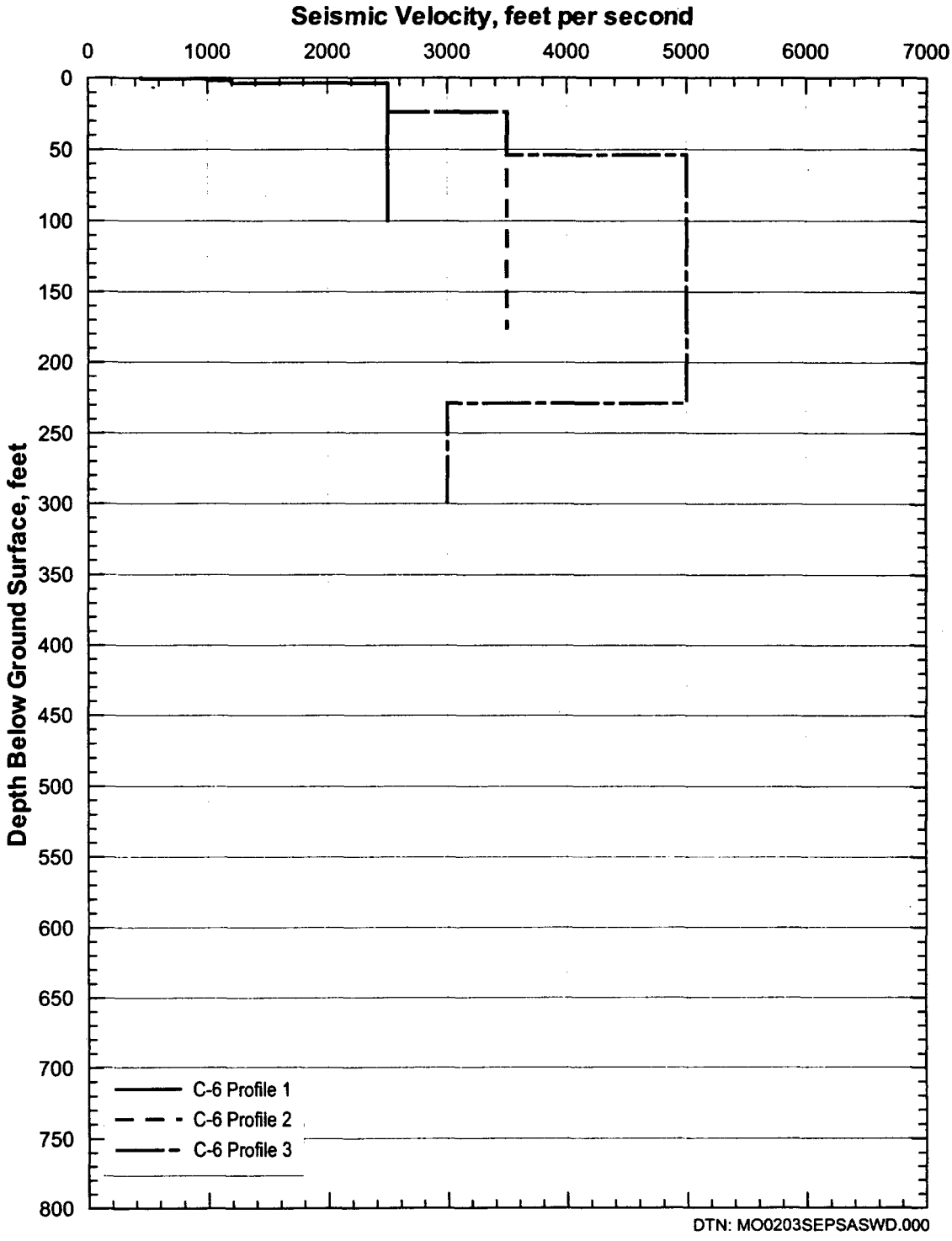

Figure 166. Shear-Wave Velocity Profiles from SASW C-6

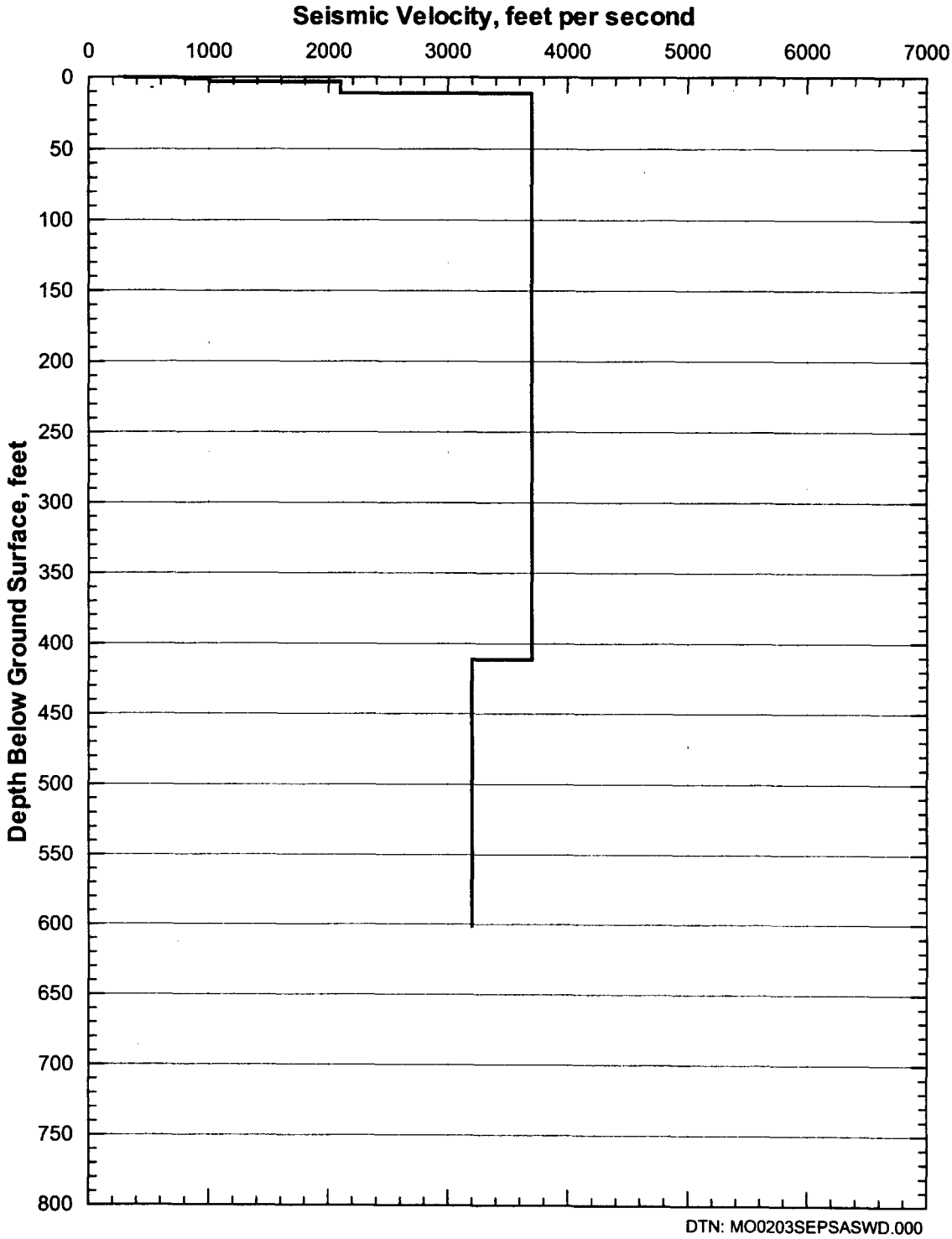

Figure 167. Shear-Wave Velocity Profile from SASW C-7

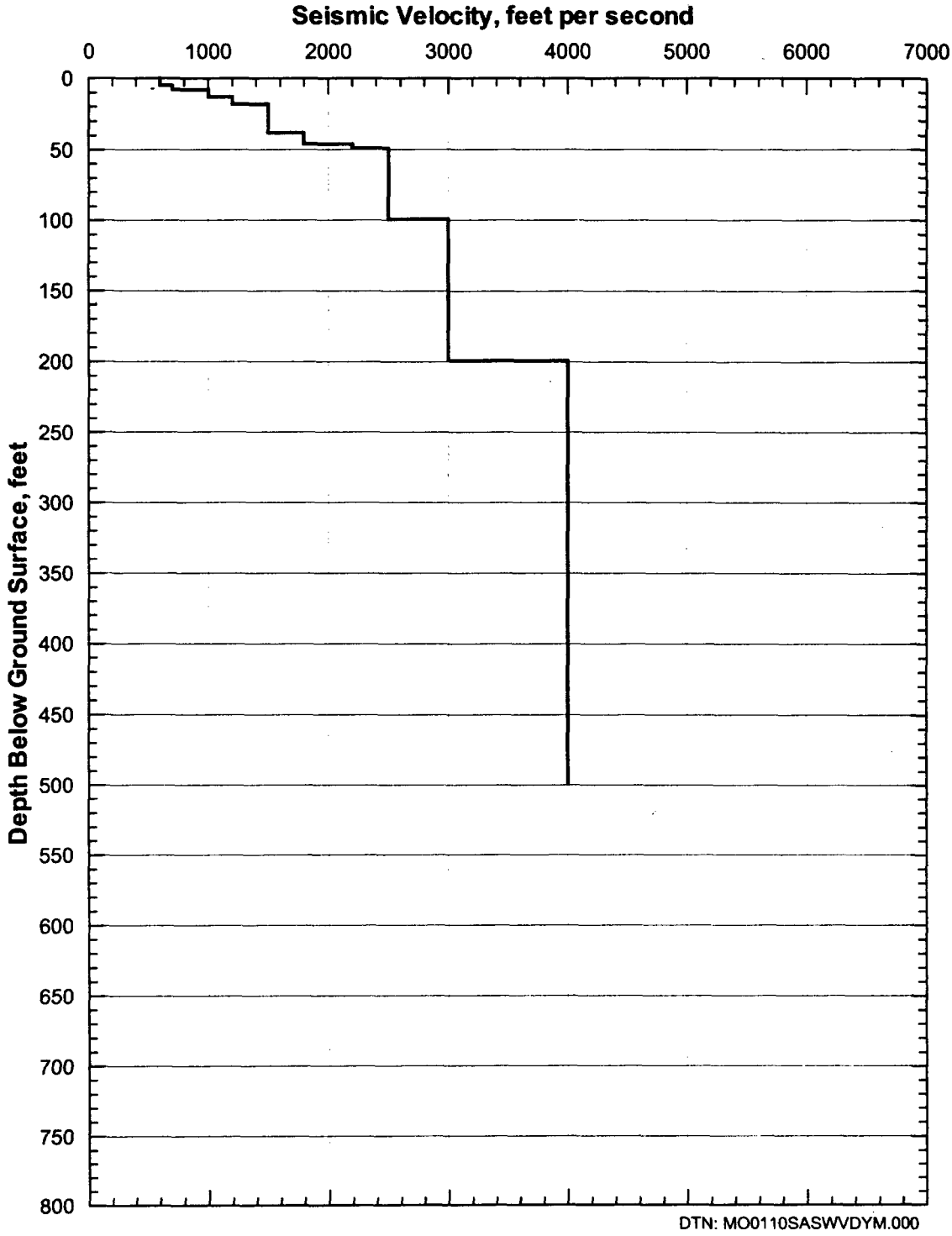

Figure 168. Shear-Wave Velocity Profile from SASW D-1

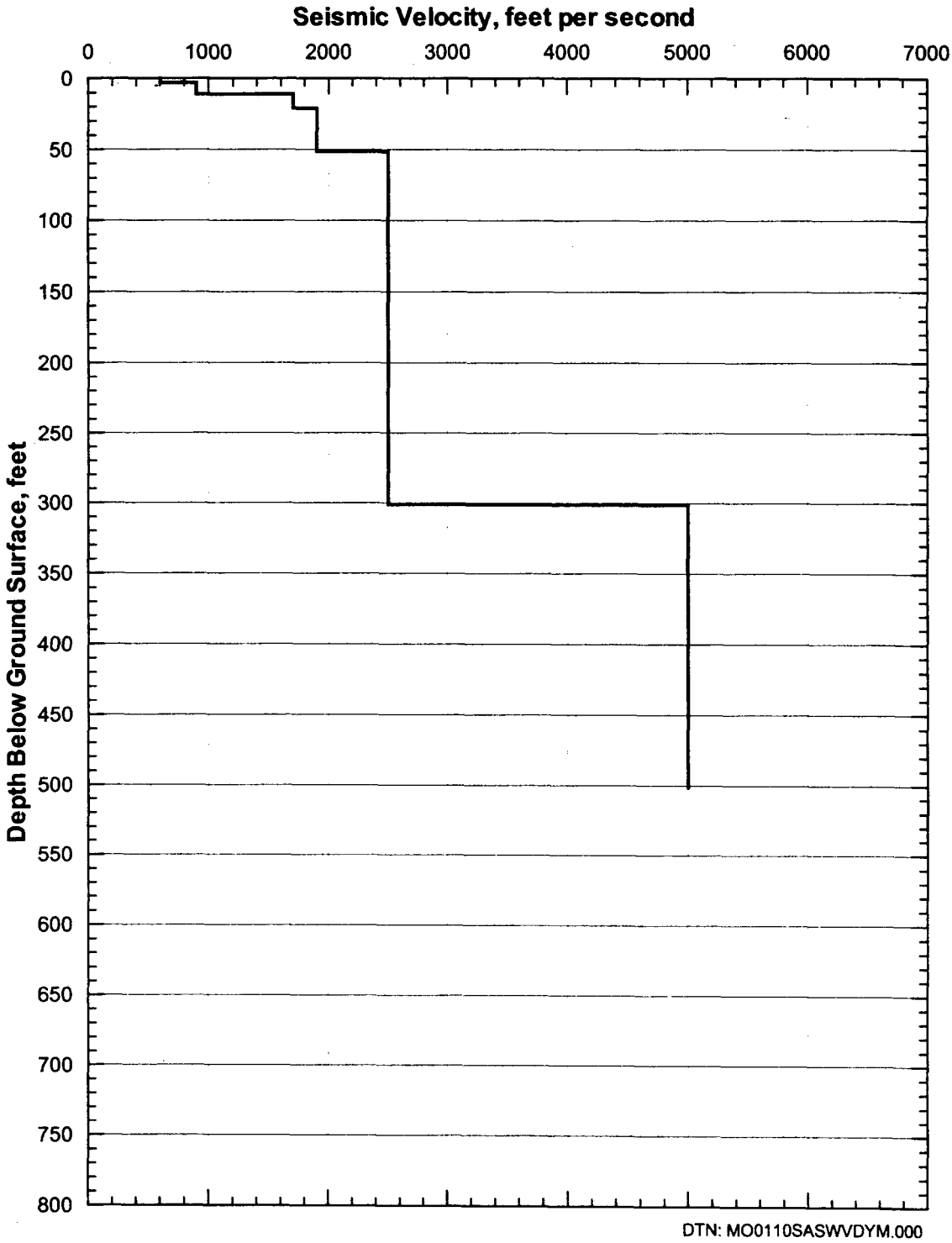

Figure 169. Shear-Wave Velocity Profile from SASW D-2

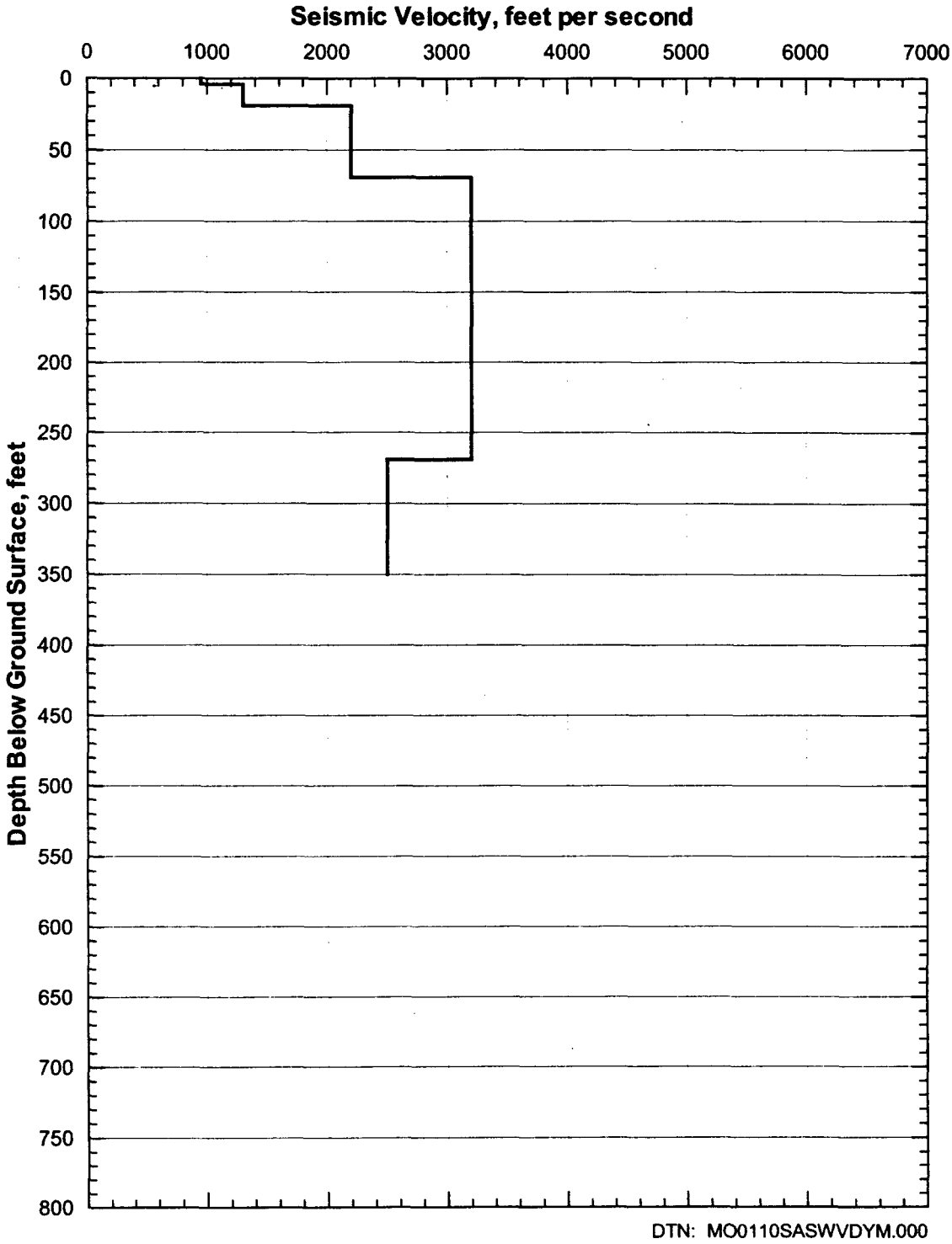

Figure 170. Shear-Wave Velocity Profile from SASW D-3

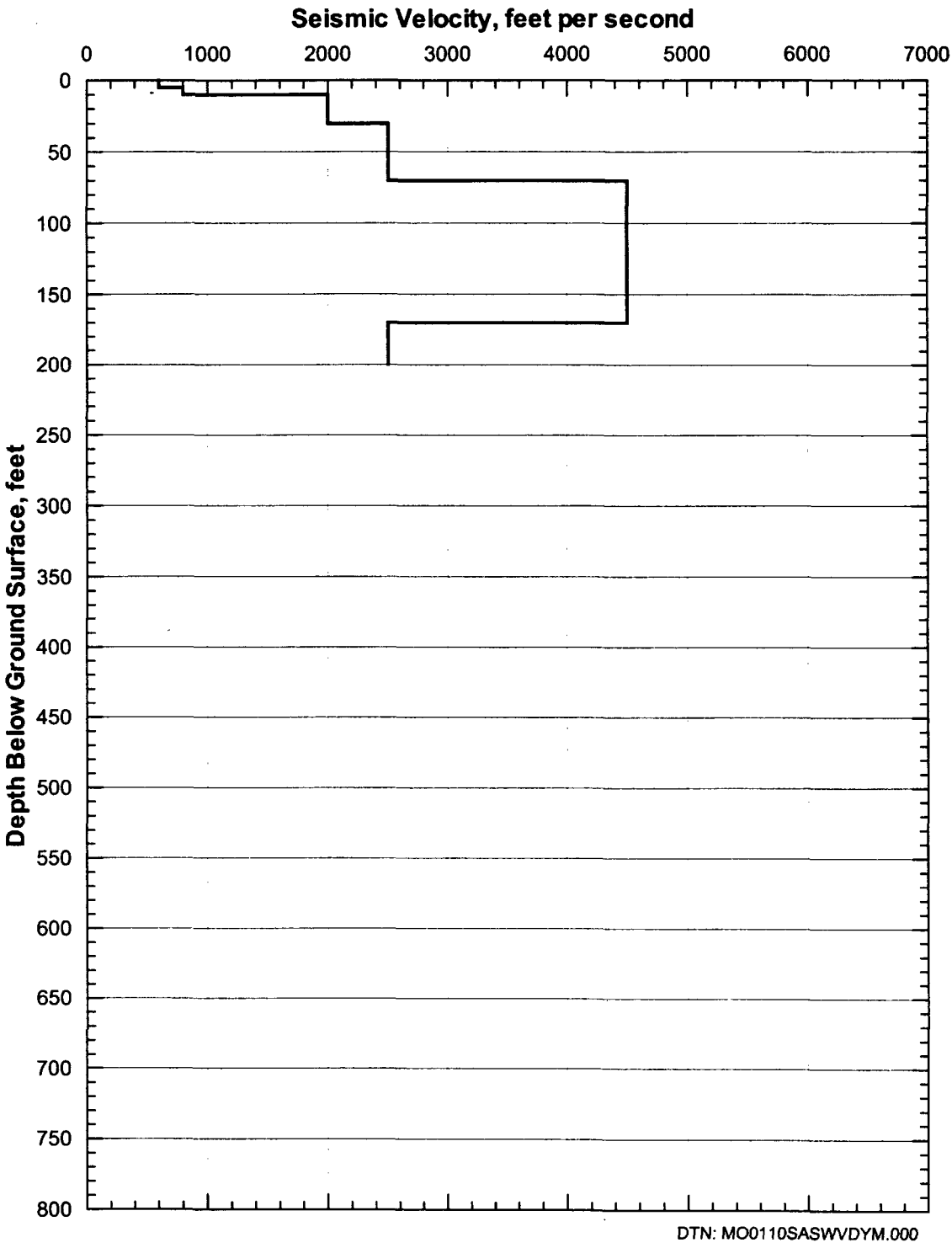

Figure 171. Shear-Wave Velocity Profile from SASW D-4

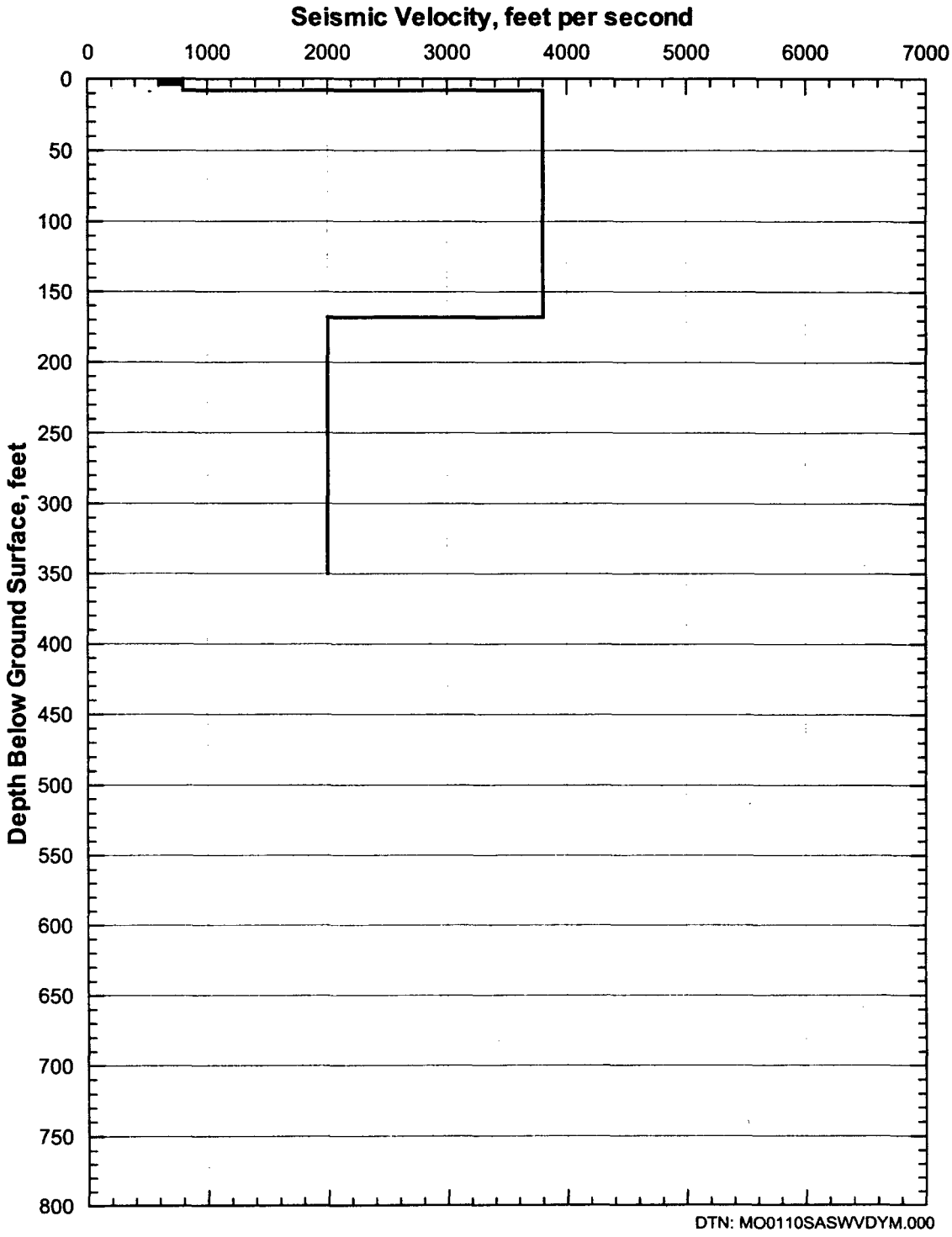

Figure 172. Shear-Wave Velocity Profile from SASW D-5

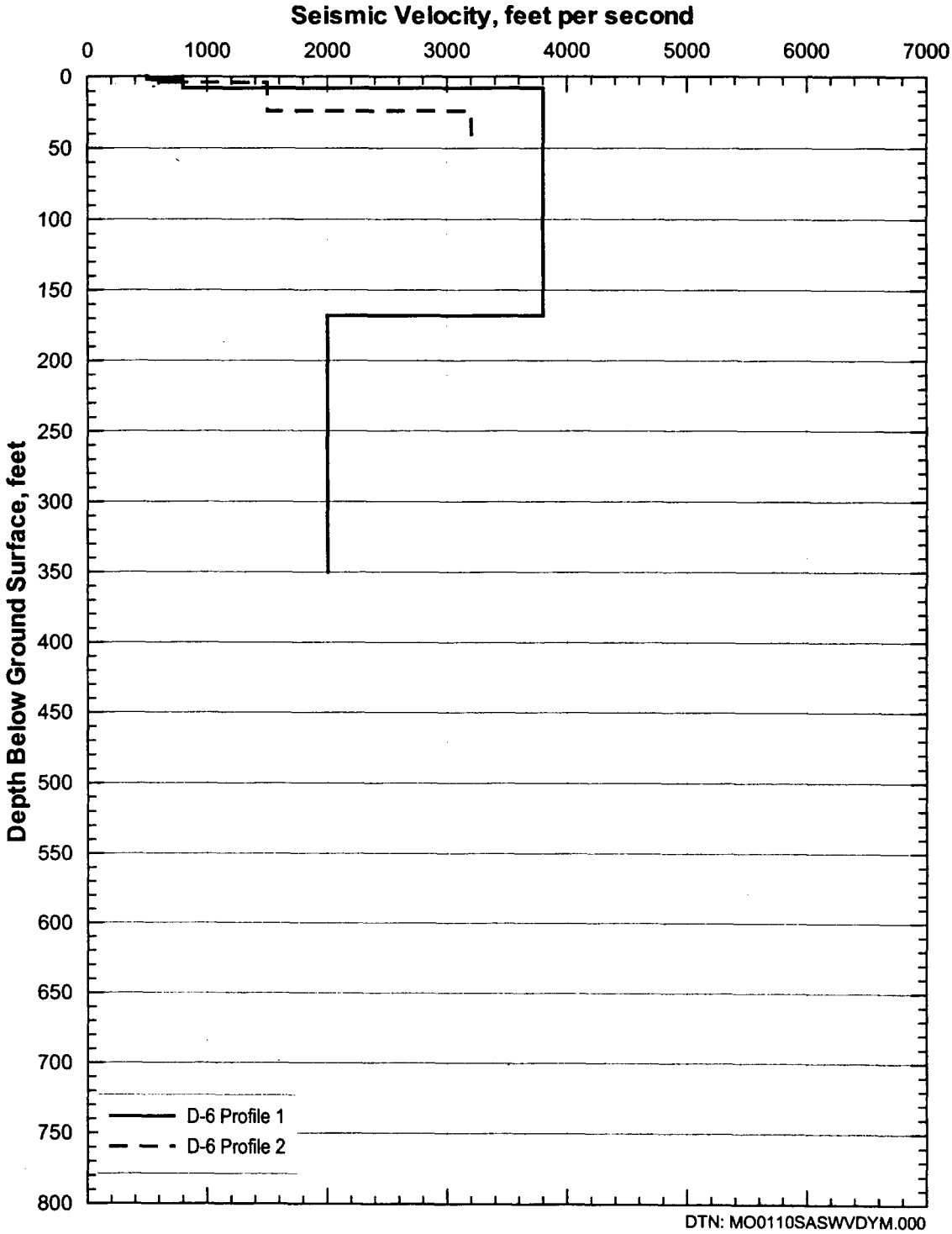

Figure 173. Shear-Wave Velocity Profiles from SASW D-6

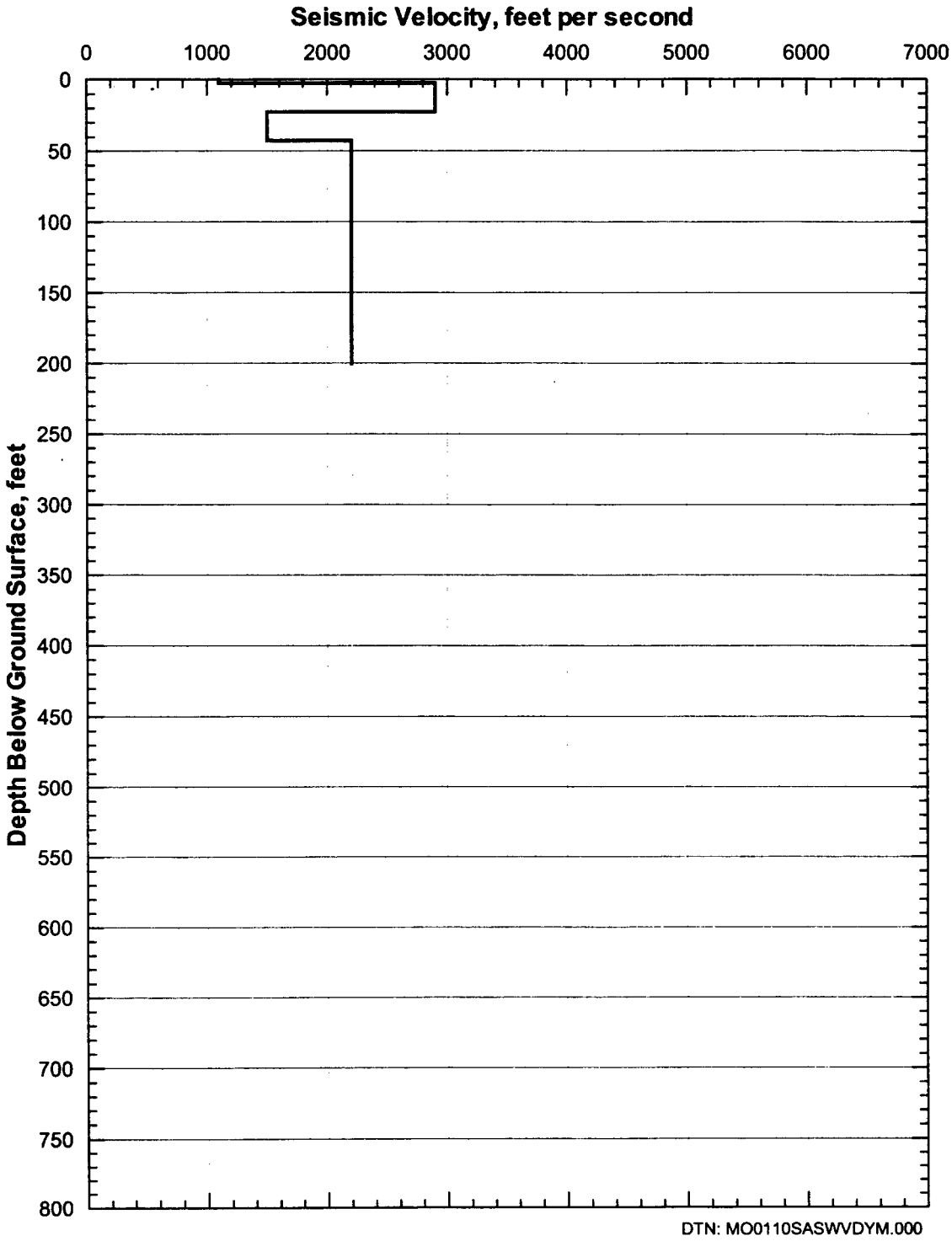

Figure 174. Shear-Wave Velocity Profile from SASW D-7

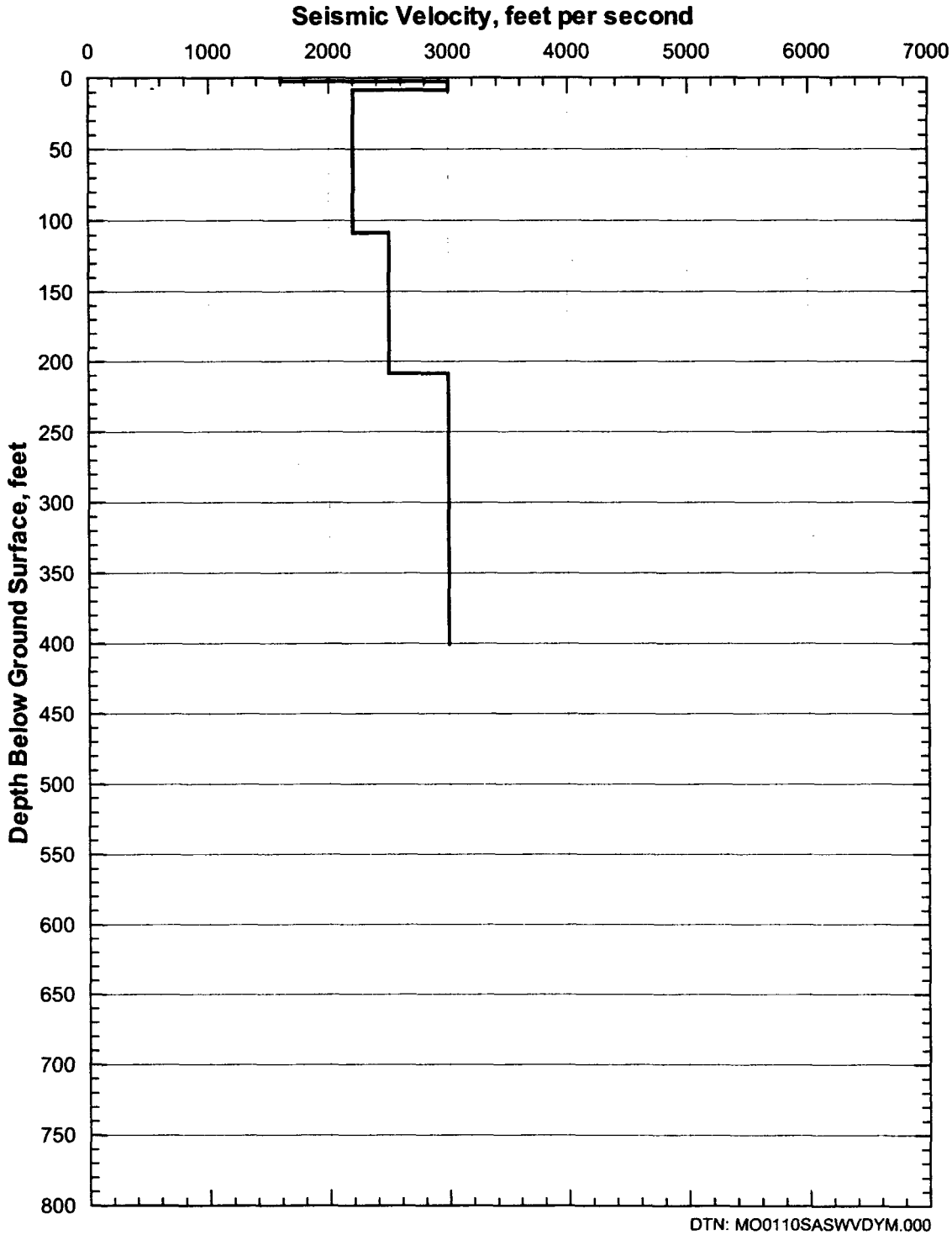

Figure 175. Shear-Wave Velocity Profile from SASW D-8

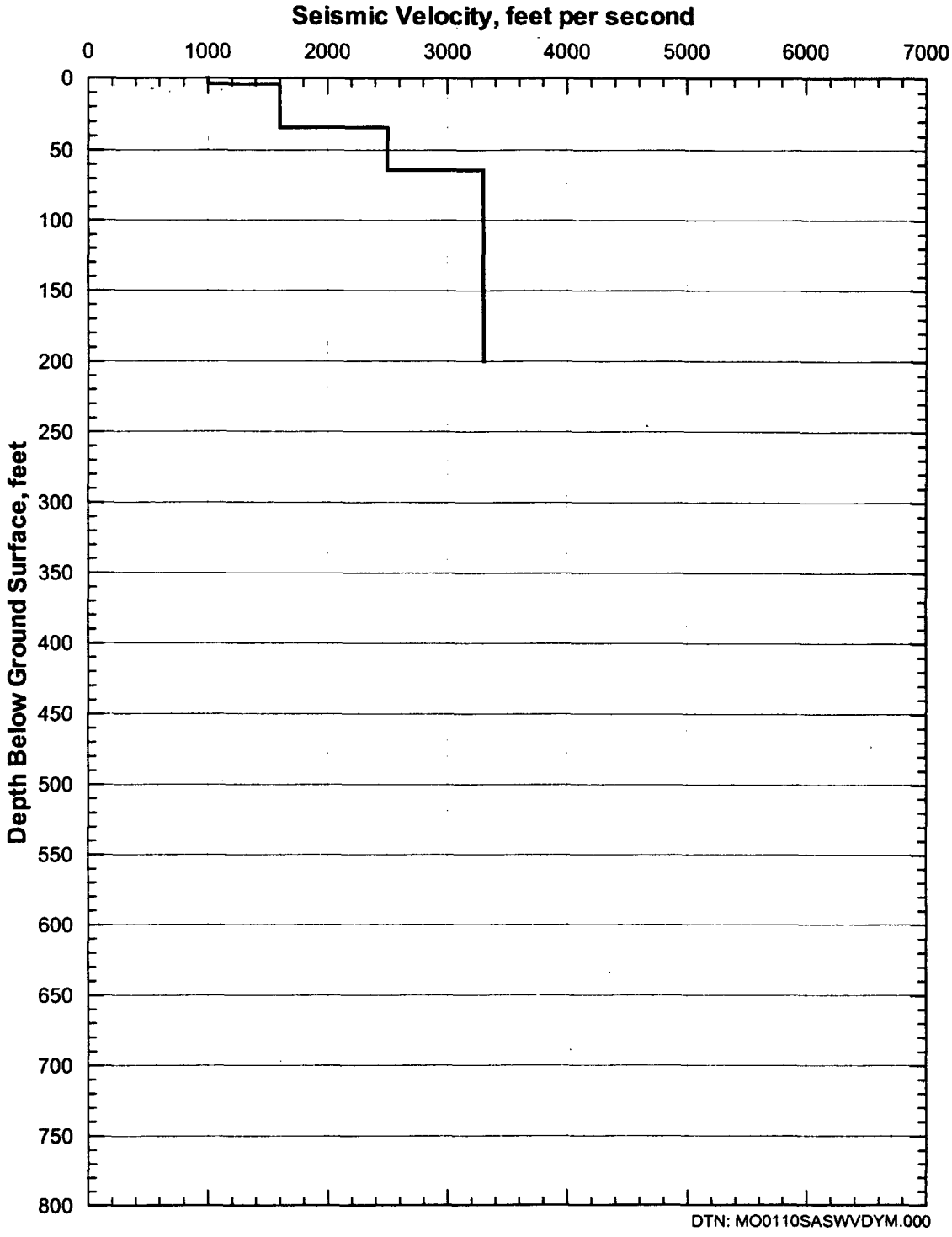

Figure 176. Shear-Wave Velocity Profile from SASW D-9

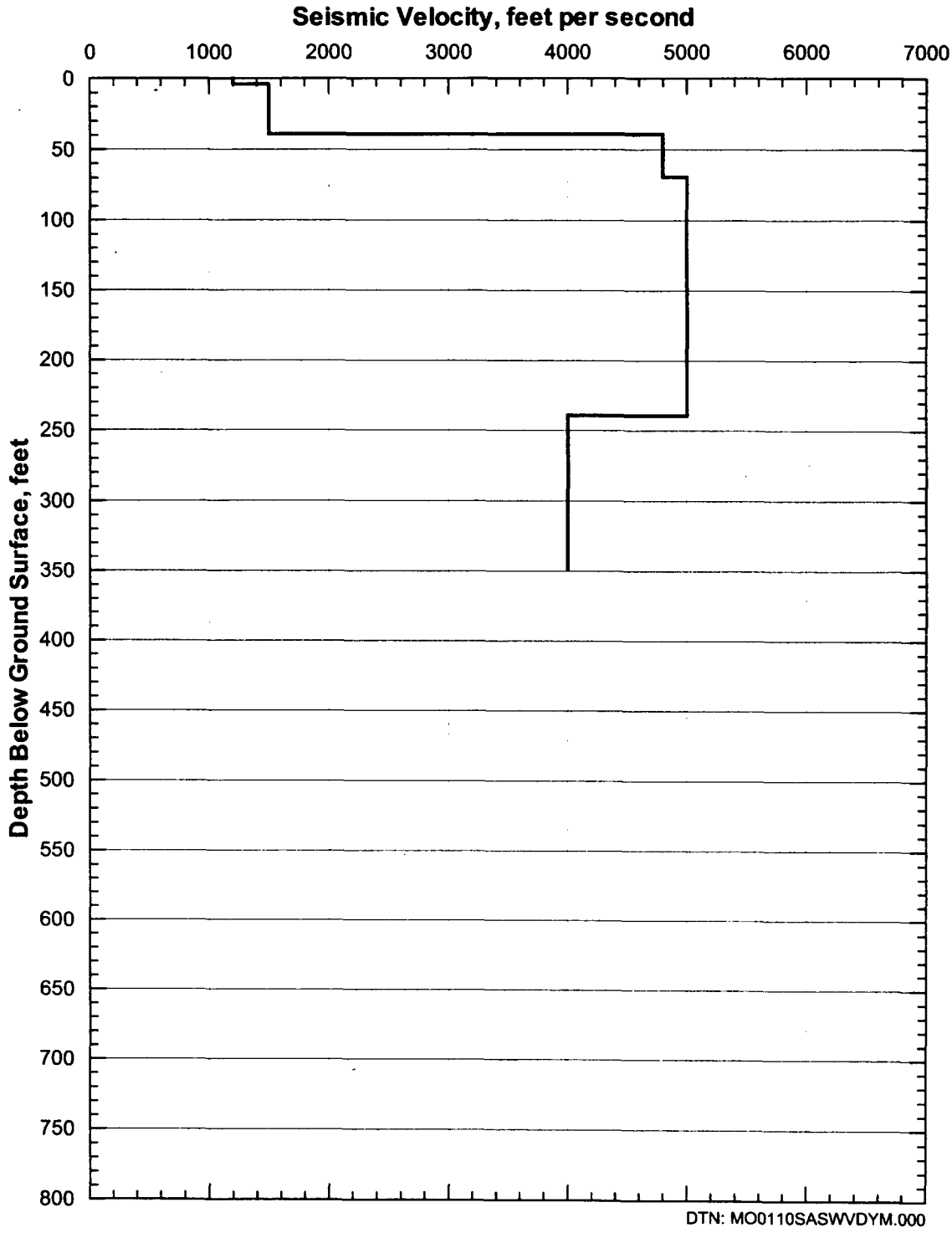

Figure 177. Shear-Wave Velocity Profile from SASW D-10

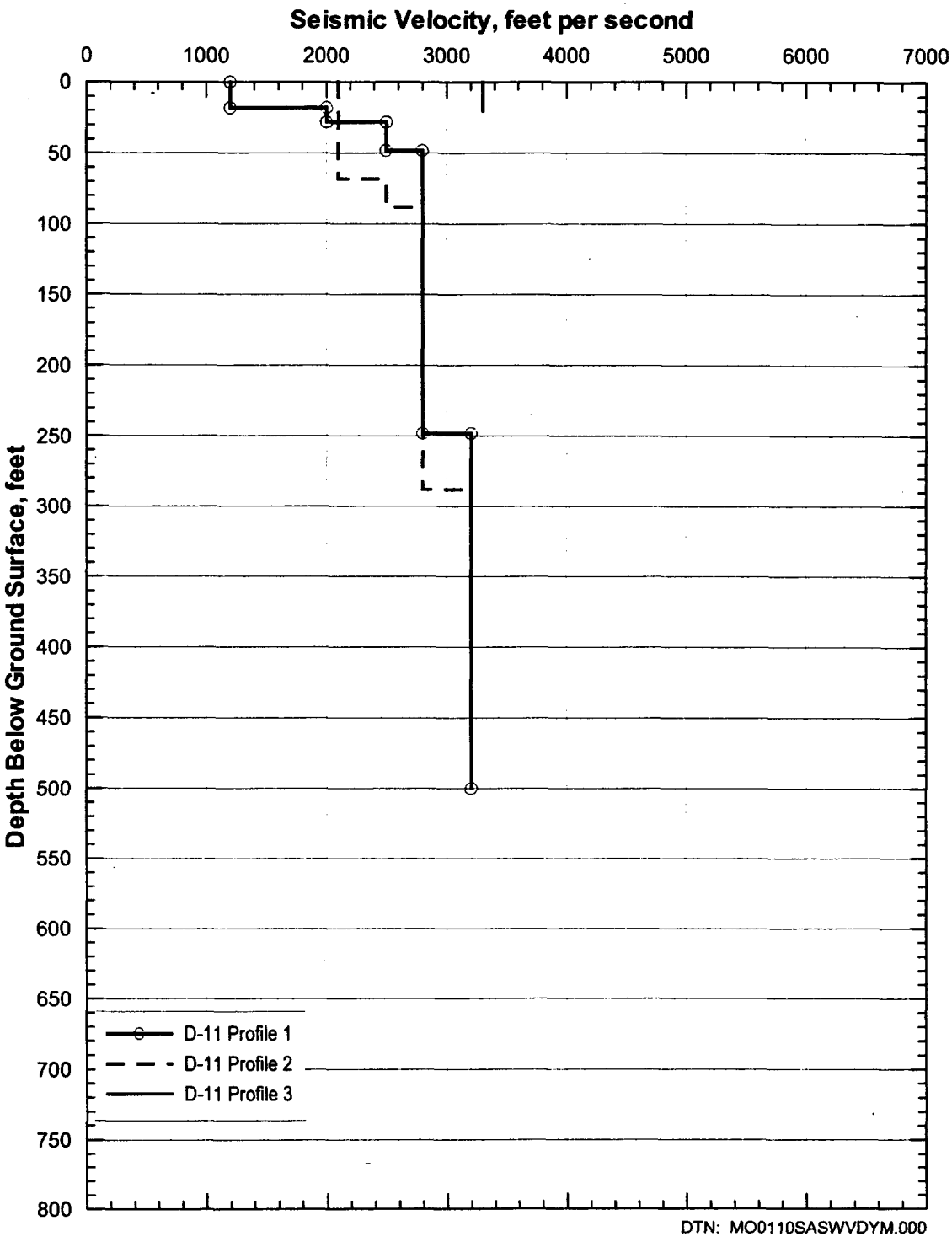

Figure 178. Shear-Wave Velocity Profiles from SASW D-11

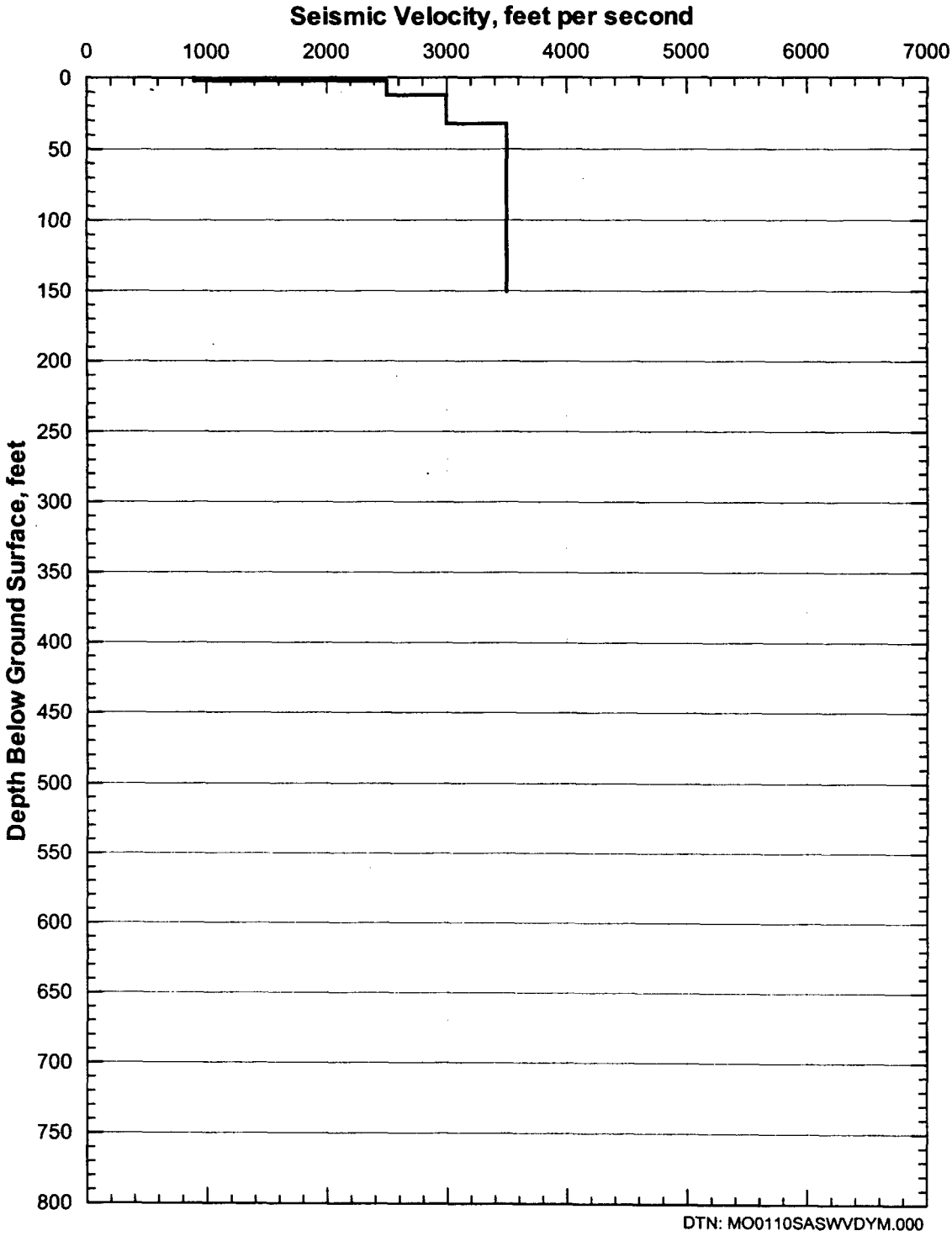

Figure 179. Shear-Wave Velocity Profile from SASW S-1

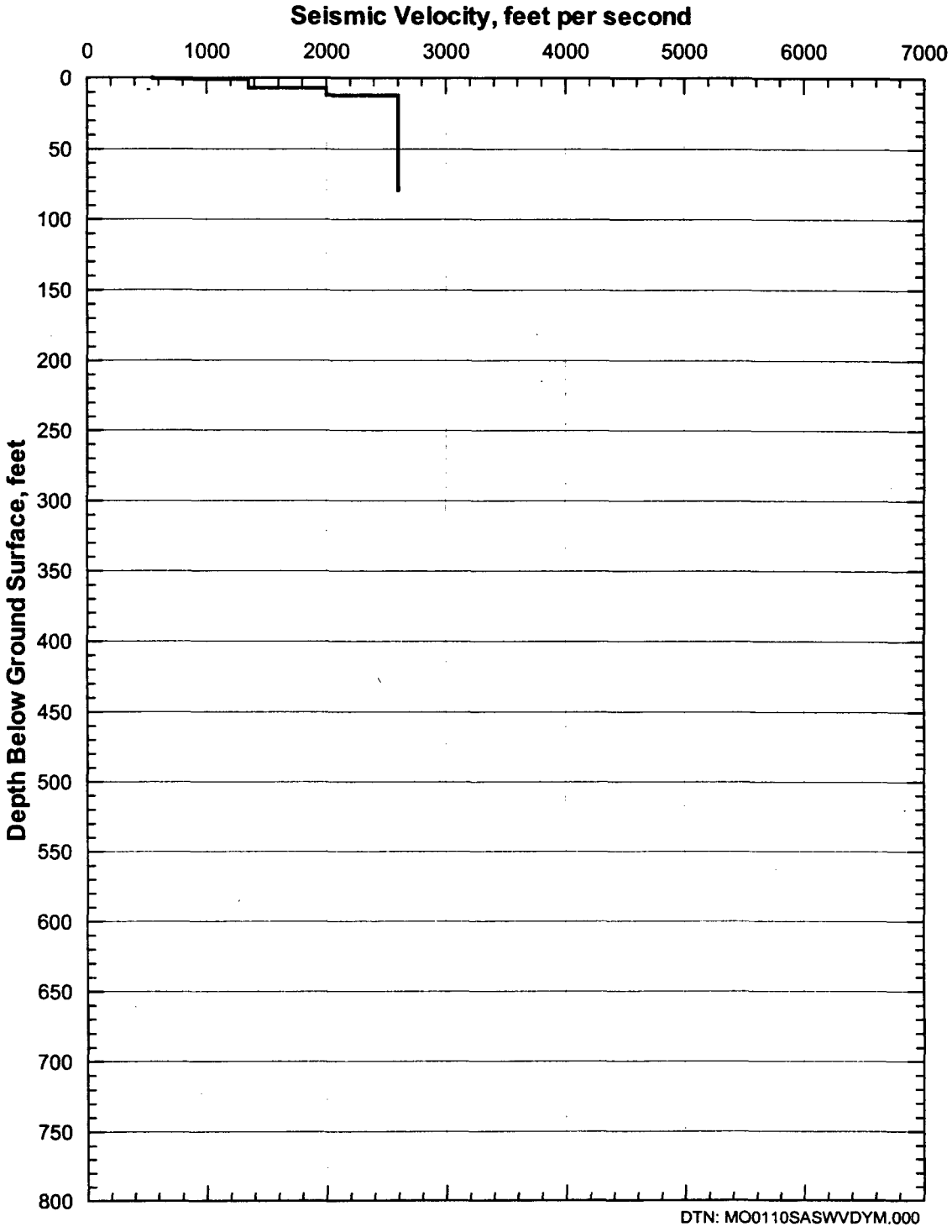

Figure 180. Shear-Wave Velocity Profile from SASW S-2

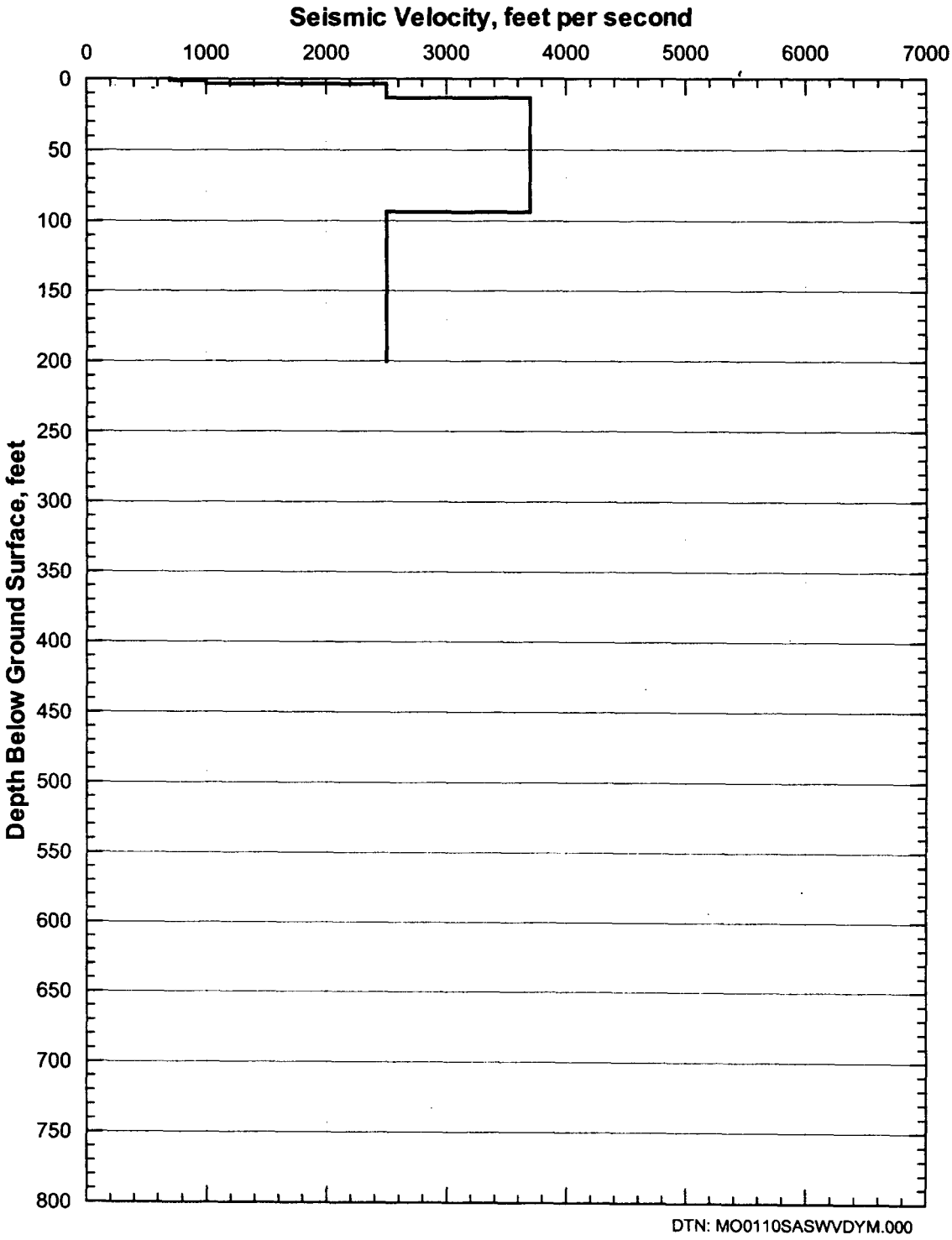

Figure 181. Shear-Wave Velocity Profile from SASW S-3

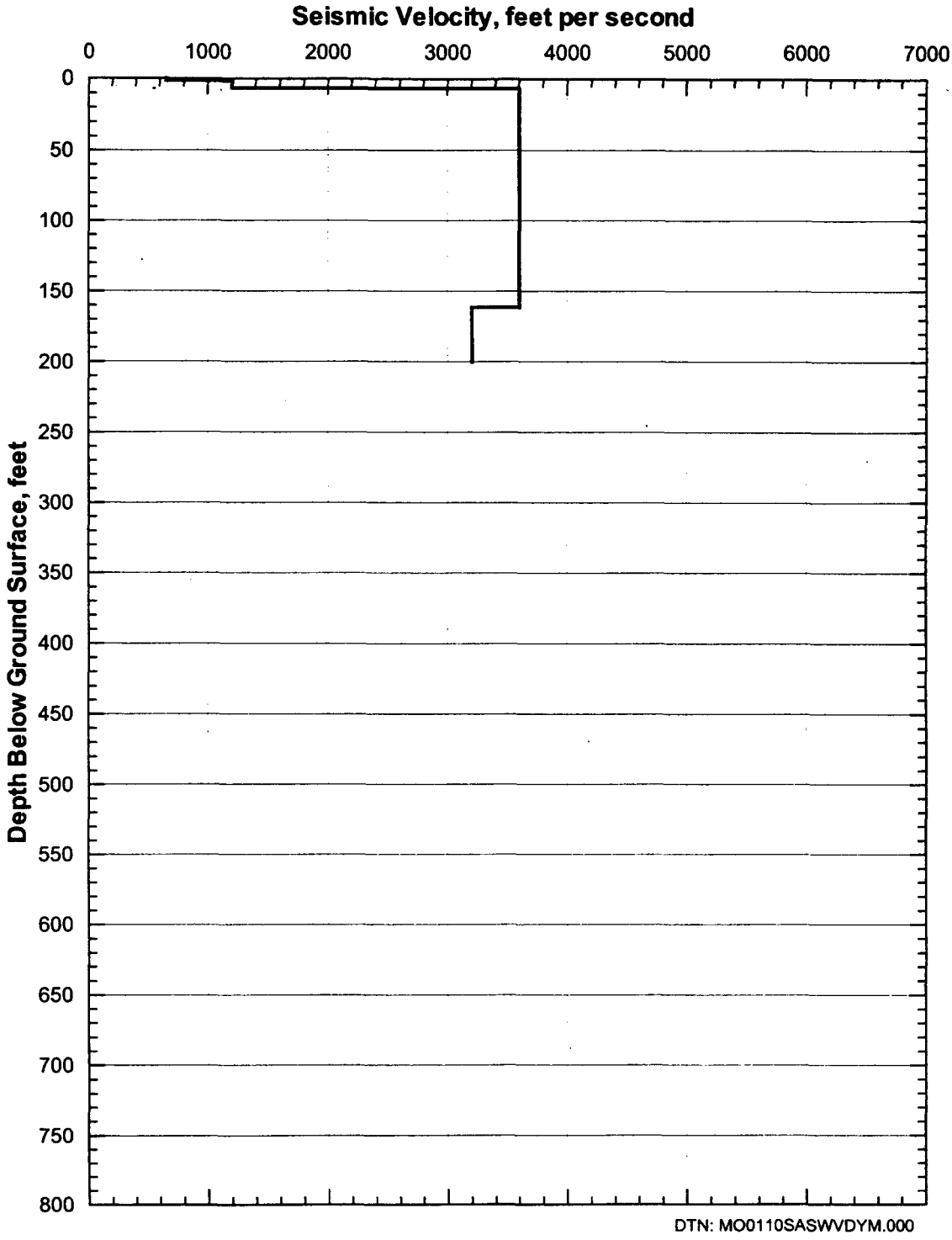

Figure 182. Shear-Wave Velocity Profile from SASW S-4

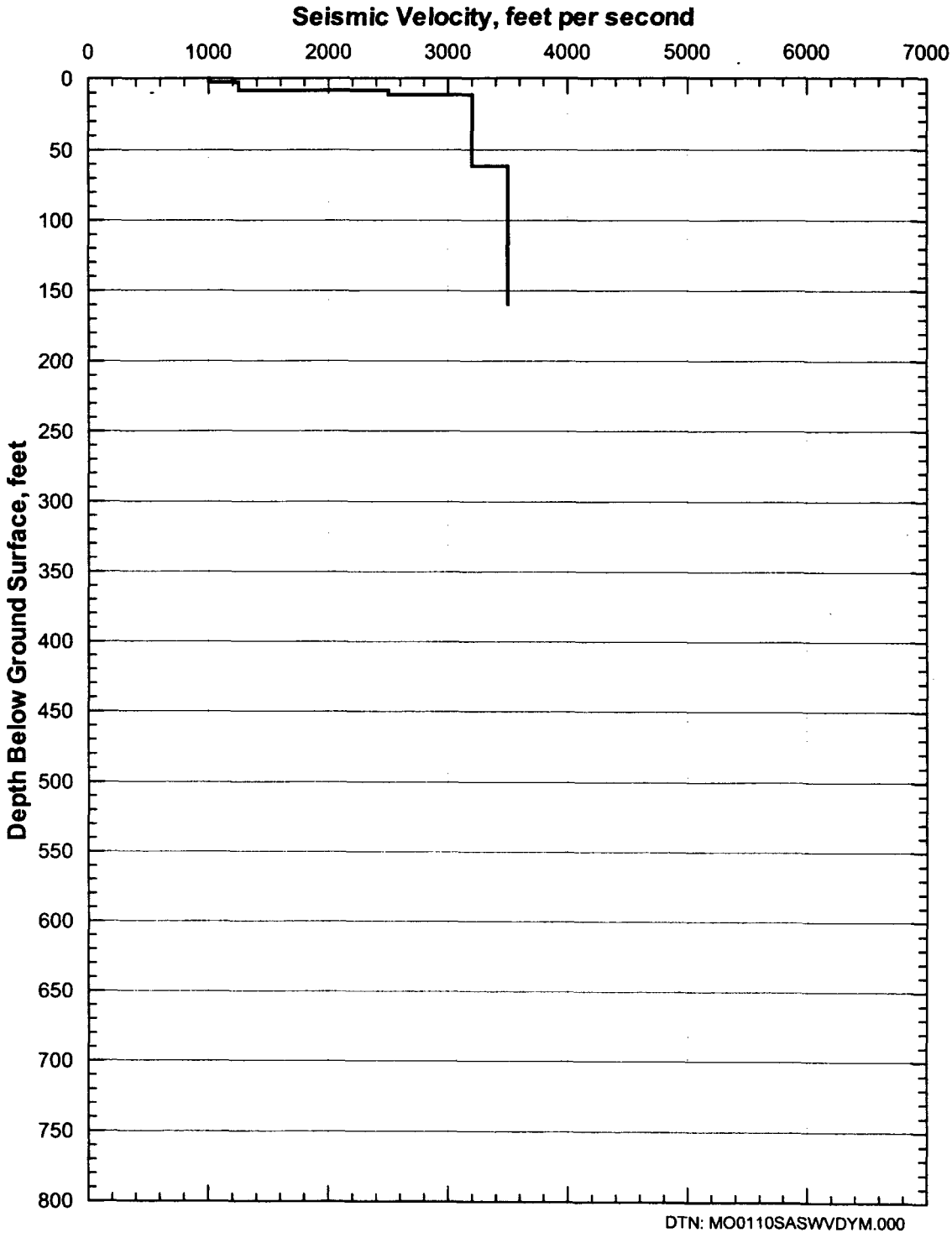

Figure 183. Shear-Wave Velocity Profile from SASW S-5

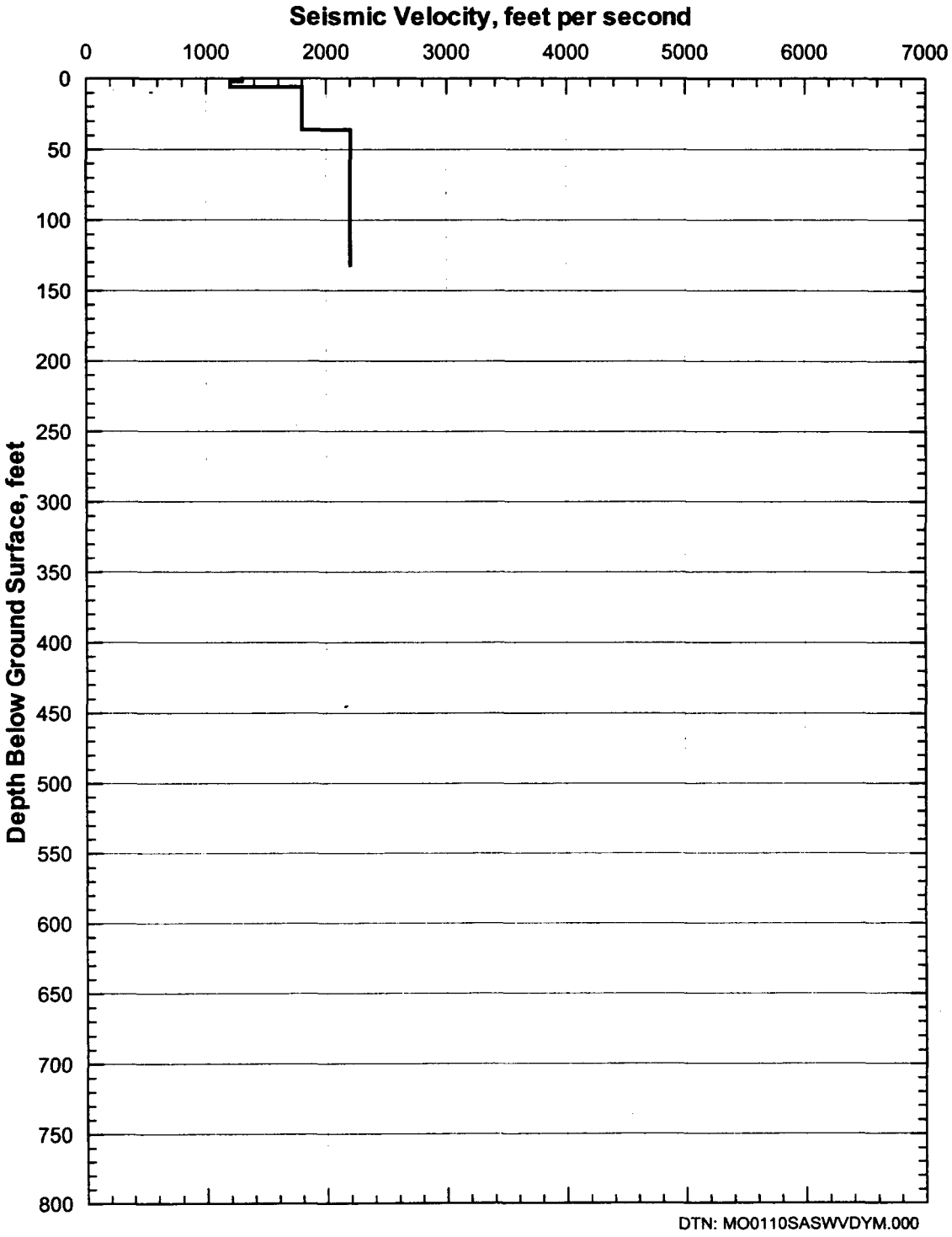

Figure 184. Shear-Wave Velocity Profile from SASW S-6

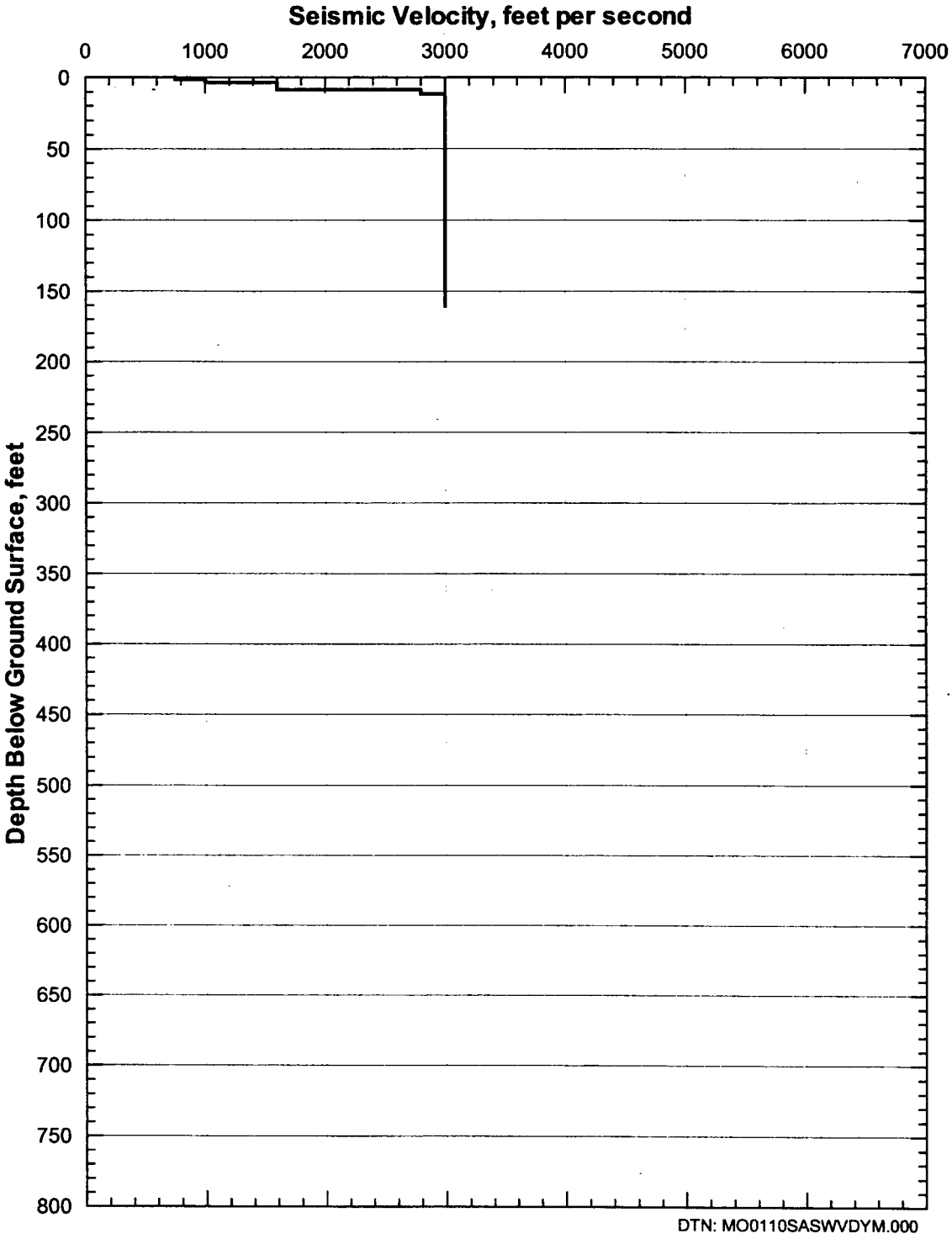

Figure 185. Shear-Wave Velocity Profile from SASW S-7

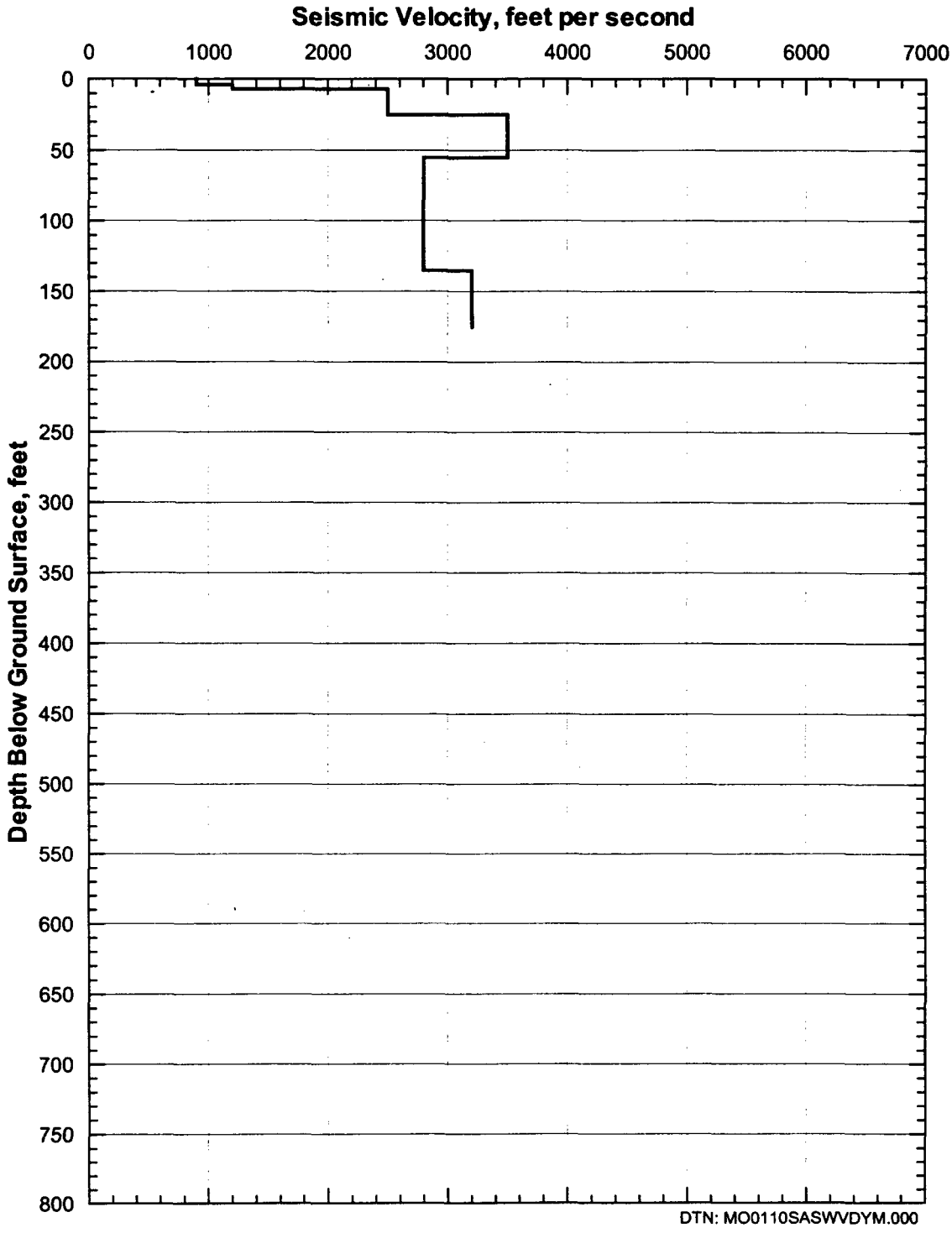

Figure 186. Shear-Wave Velocity Profile from SASW S-8

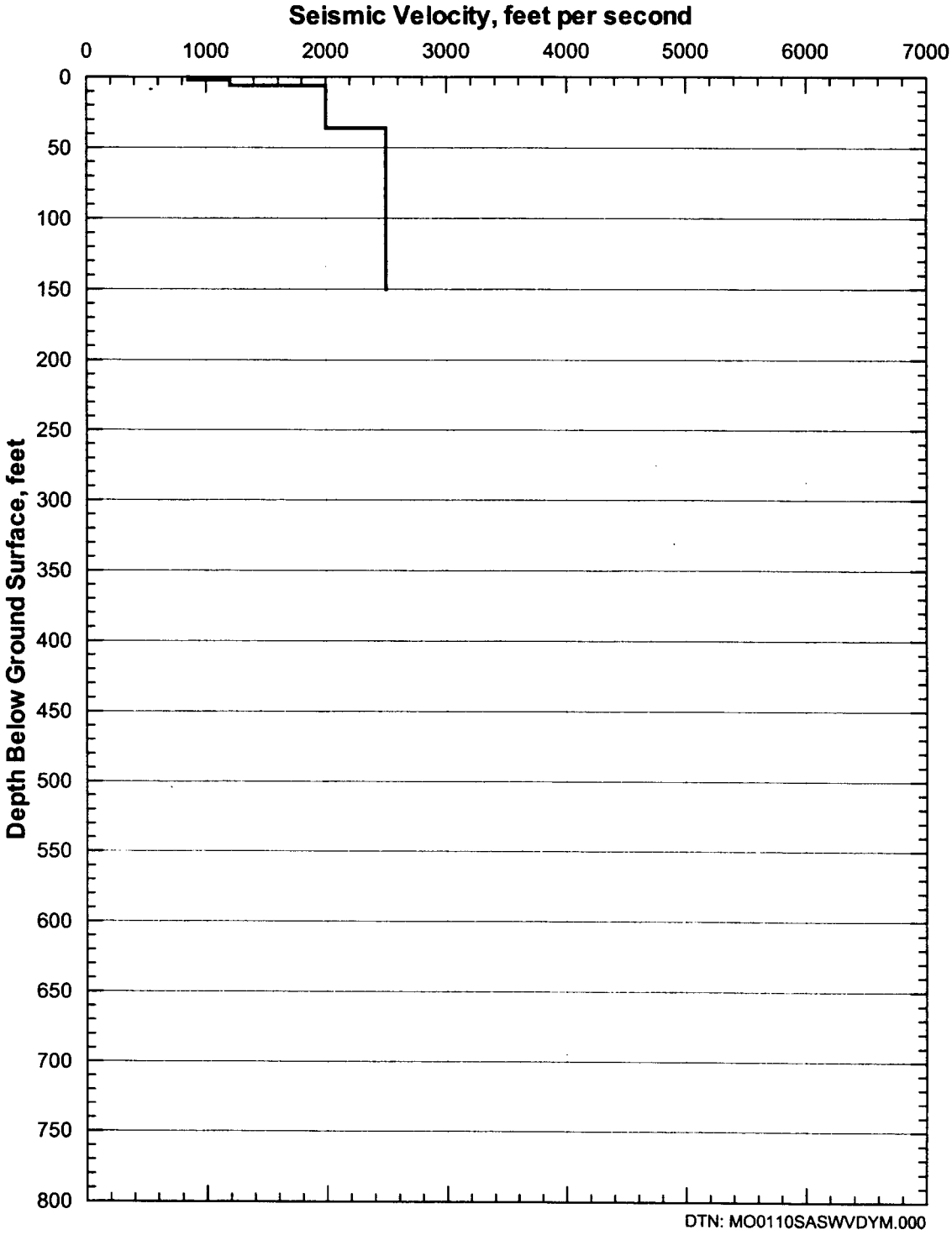

Figure 187. Shear-Wave Velocity Profile from SASW S-9

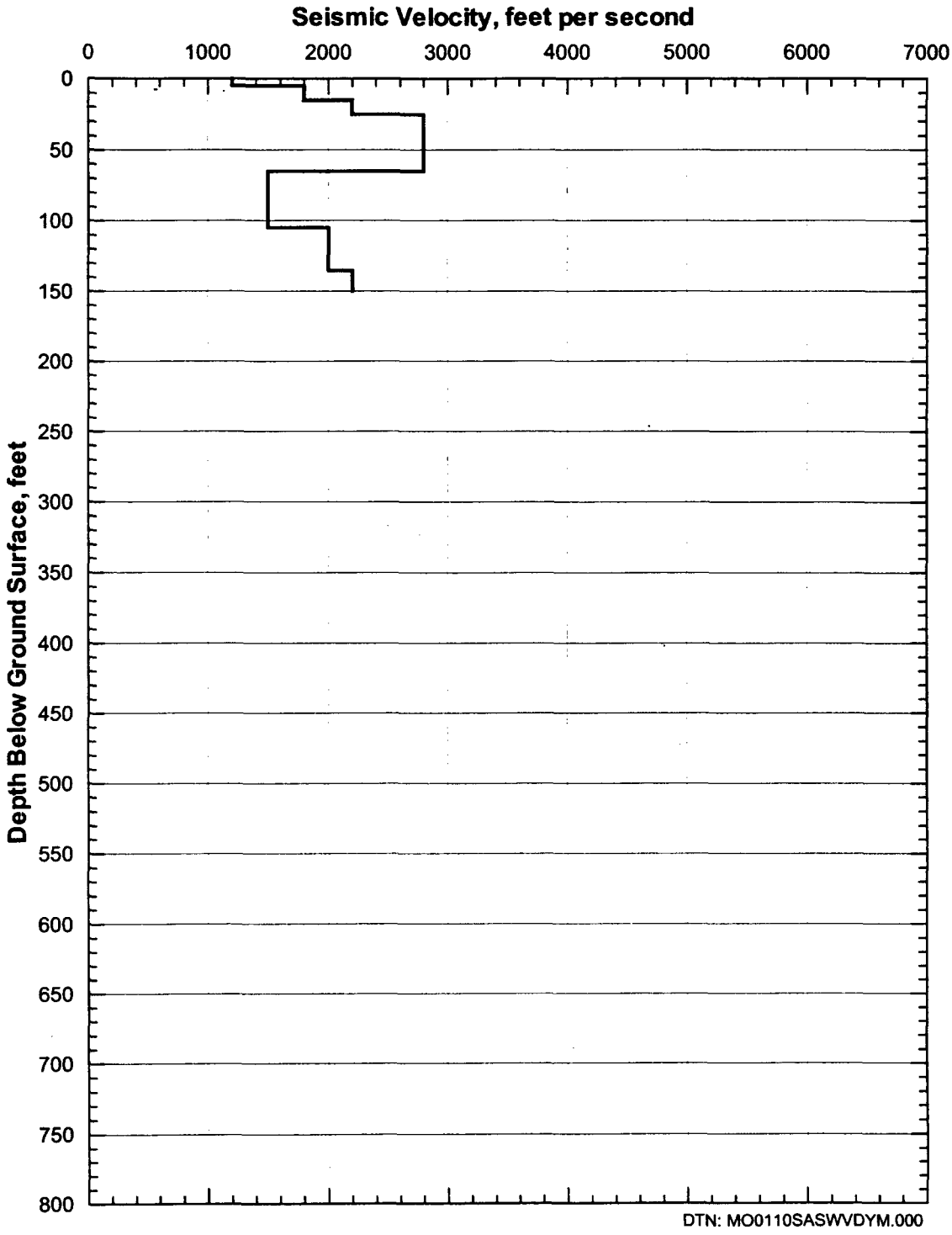

Figure 188. Shear-Wave Velocity Profile from SASW S-10

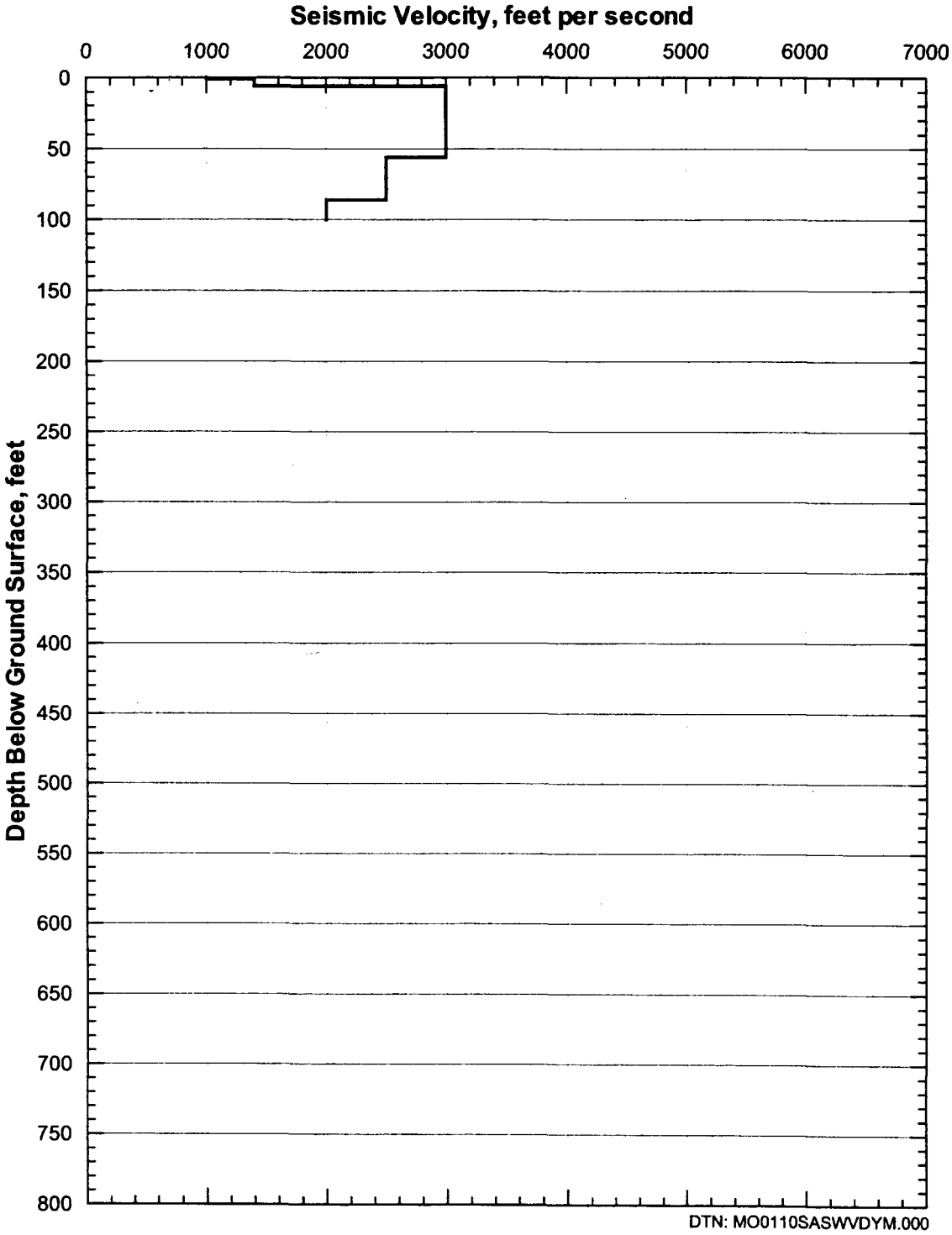

Figure 189. Shear-Wave Velocity Profile from SASW S-11

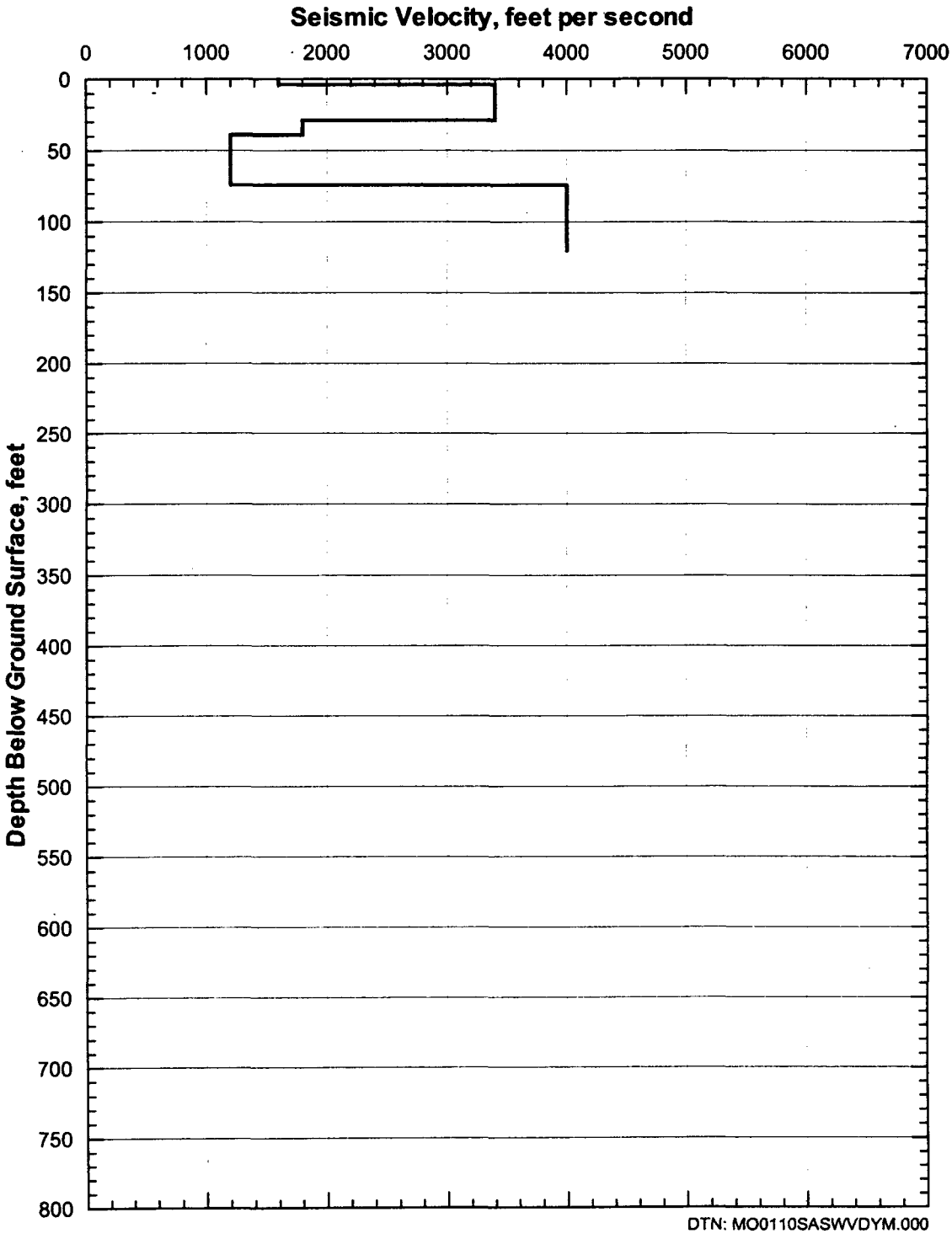

Figure 190. Shear-Wave Velocity Profile from SASW S-12

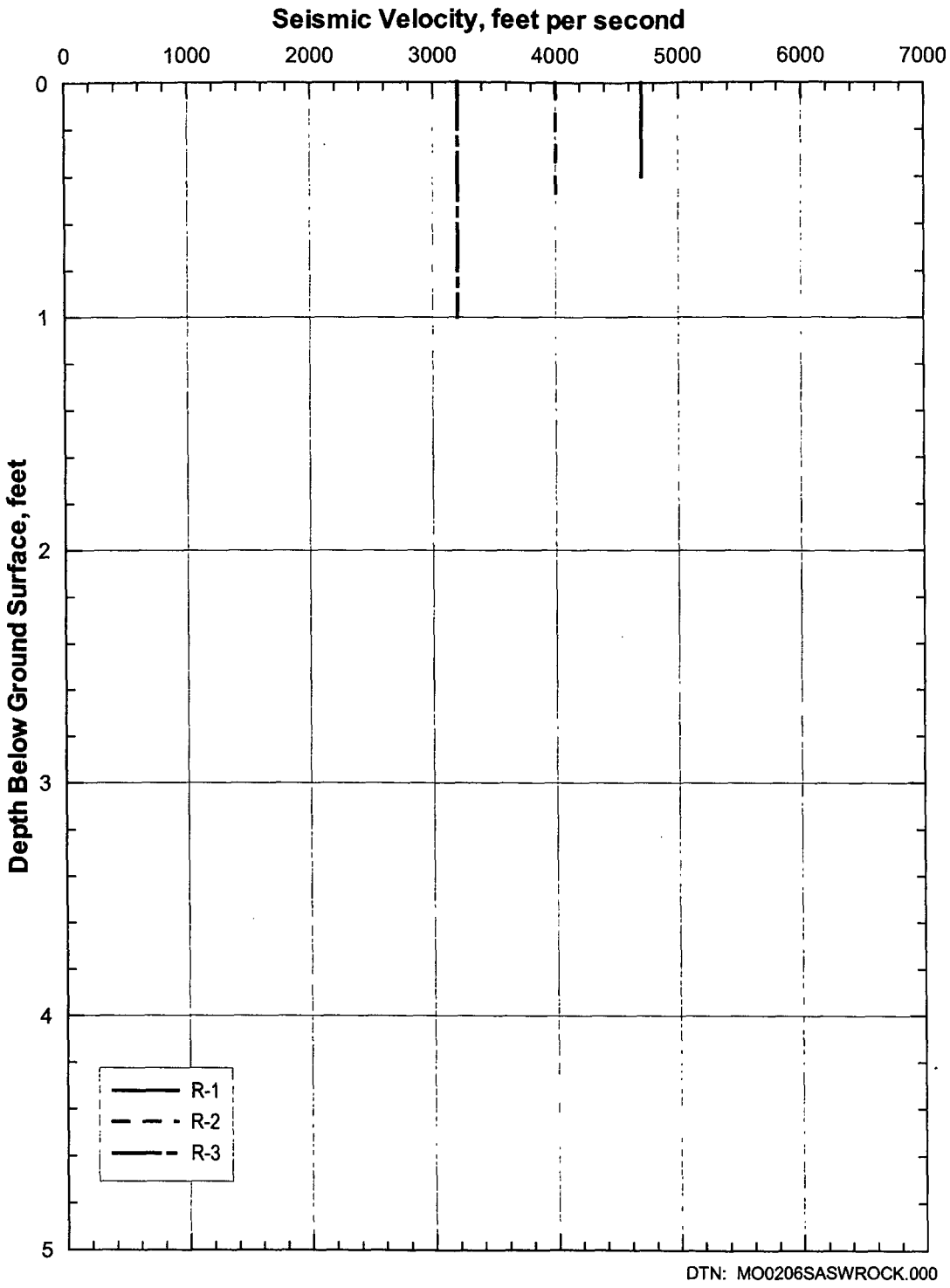

Figure 191. Shear-Wave Velocity Profiles from SASW R Measurements

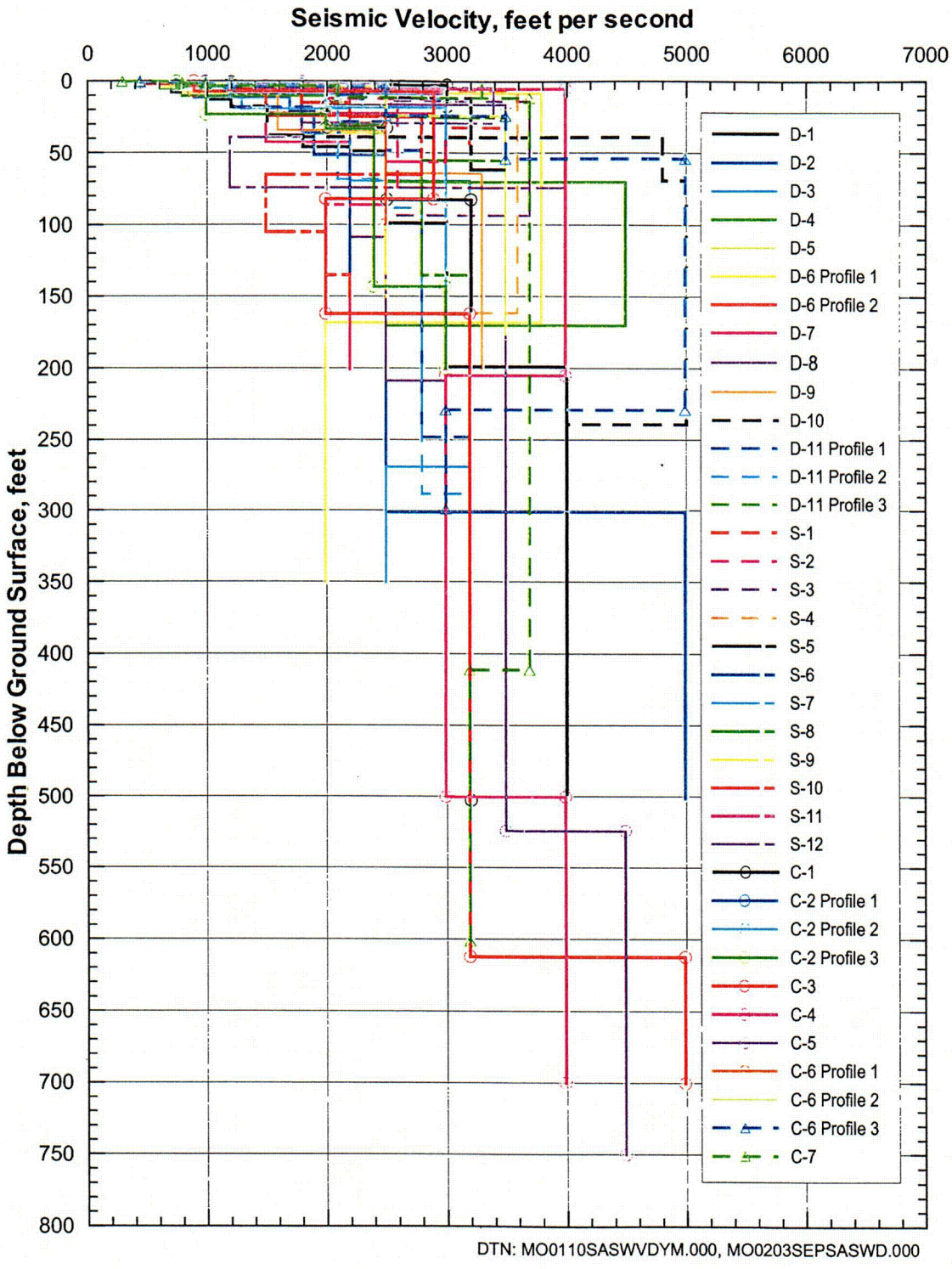

Figure 192. Shear-Wave Velocity Profiles from SASW Measurements on Top of Yucca Mountain

C06

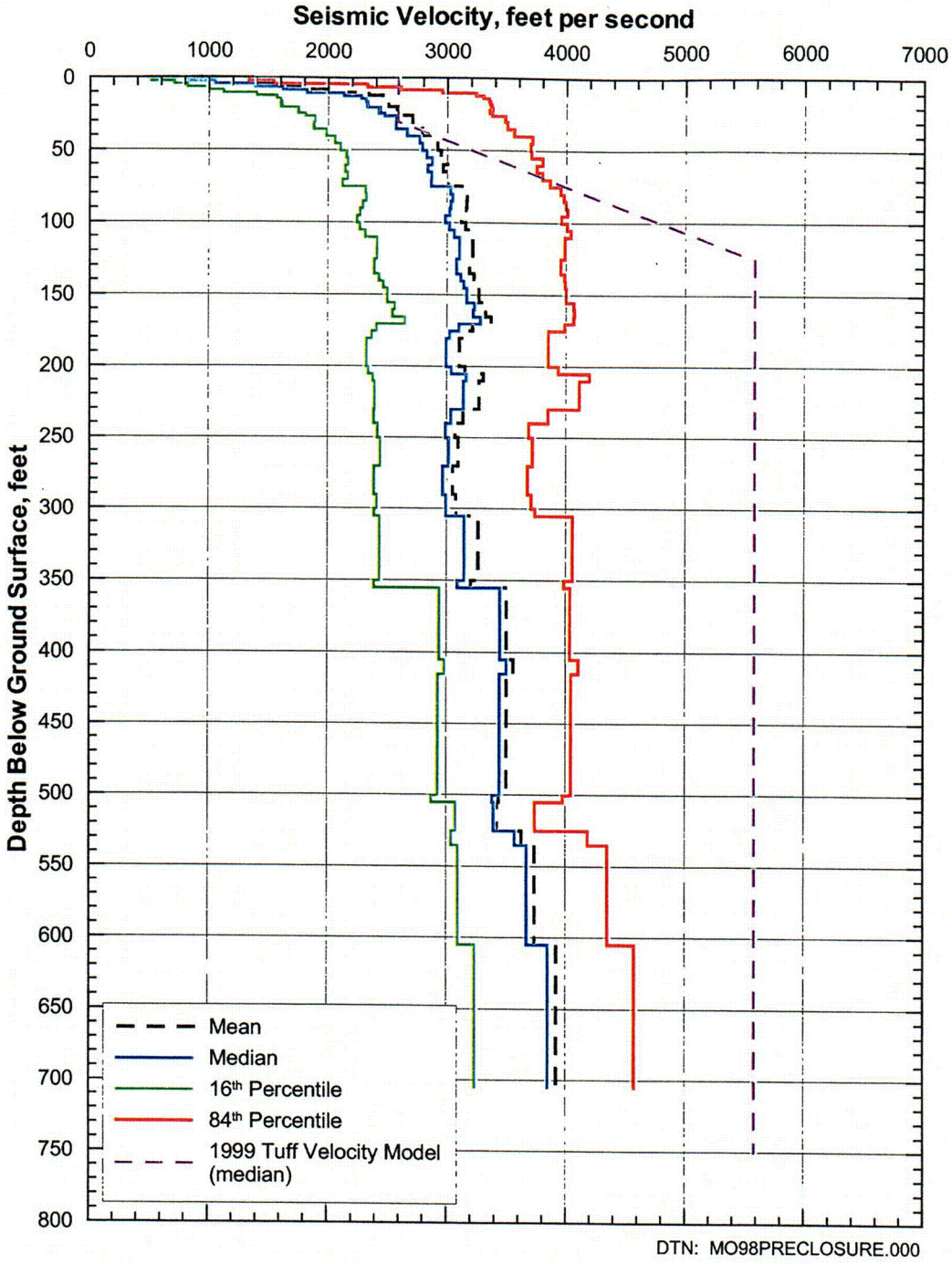

Note: These statistics have been calculated for illustrative purposes only. Final statistics calculated for use in the forthcoming scientific analysis entitled *Development of Seismic Design Input Ground Motions for a Geological Repository at Yucca Mountain* will be submitted to the TDMS.

Figure 193. Statistical Analyses of Shear-Wave Velocity Profiles from SASW Measurements on Top of Yucca Mountain

C07

Of the 22 surveys performed along or near the crest, 13 surveys (C-1, C-3, C-4, C-5, C-7, S-1, S-3, S-4, S-5, S-7, S-8, D-10, and D-11) were oriented approximately parallel to the crest of Yucca Mountain (Figure 157). The profiles determined from these 13 surveys are shown on Figure 194. Nine surveys (C-2, C-6, S-2, S-6, S-9, S-10, S-11, D-8, and D-9) were oriented approximately perpendicular to the crest and generally downslope of the crest (some are on the road leading to the top of Yucca Mountain). The shear-wave velocity profiles from these 9 surveys are presented on Figure 195. On Figure 194, profile D-10 has much higher shear-wave velocities than the other profiles. Likewise, in Figure 195, C-6 yielded profiles that were significantly greater than the others. Interestingly, C-6 and D-10 are located relatively near each other on the mountain (Figure 157), and may reflect an area of locally higher velocity, although the intervening S-5 profile is not anomalously higher than the other profiles.

A comparison between the mean shear-wave velocity profile oriented parallel to the crest and the mean profile from surveys oriented perpendicular to the crest indicates a difference of up to about 600 ft/s in the top 150 ft (Figure 196). This difference may be related to anisotropy due to fracturing in the near-surface volcanic units of Yucca Mountain. Fractures were observed to be generally oriented parallel to the crest and thus velocity measurements perpendicular to the crest are being made across open(?) fractures, possibly resulting in lower velocities. At this time, this hypothesis is speculative. Below a depth of 150 ft, there are few deep profiles perpendicular to the crest to make a valid comparison. Only two profiles extend to depths greater than 200 ft (Figure 195). This lack of deep penetration was due to access limitations down the side of Yucca Mountain.

Eight SASW surveys (D-1, D-2, D-3, D-4, D-5, D-6, D-7, and S-12) were located at some distance on several roads east of the crest of the mountain (Figure 157). In several cases, surveys were conducted along roads situated in drainages where low-velocity alluvial sediments have accumulated. These shear-wave velocity profiles are examined separately. There is considerable variability in the velocities (Figure 197). Figure 198 presents the shear-wave velocity profiles from D-1, D-2, and D-3, which were located towards the north end of the potential (as of July 2000) repository footprint (Figure 157). These three profiles generally show similar trends in shear-wave velocity in the top 200 ft. Below 200 ft, the profiles differ significantly. Figure 199 shows the shear-wave velocity profiles from D-4, D-5, and D-6 located near the central region of the potential (as of July 2000) emplacement area (Figure 157). They are also fairly consistent, and appear to generally have higher velocities in the top 150 ft than profiles D-1, D-2, and D-3. Lastly, Figure 200 presents the shear-wave velocity profiles from D-7 and S-12 located near the south end (Figure 157). As indicated by their shallow velocities, both surveys were located on a ridge and thus on rock rather than alluvium. Both of these profiles exhibit significant velocity inversions. However, the shear-wave velocity below the low-velocity zone is not well resolved with the SASW method. Therefore, the difference in velocities at depth may not be as great as is indicated on Figure 200.

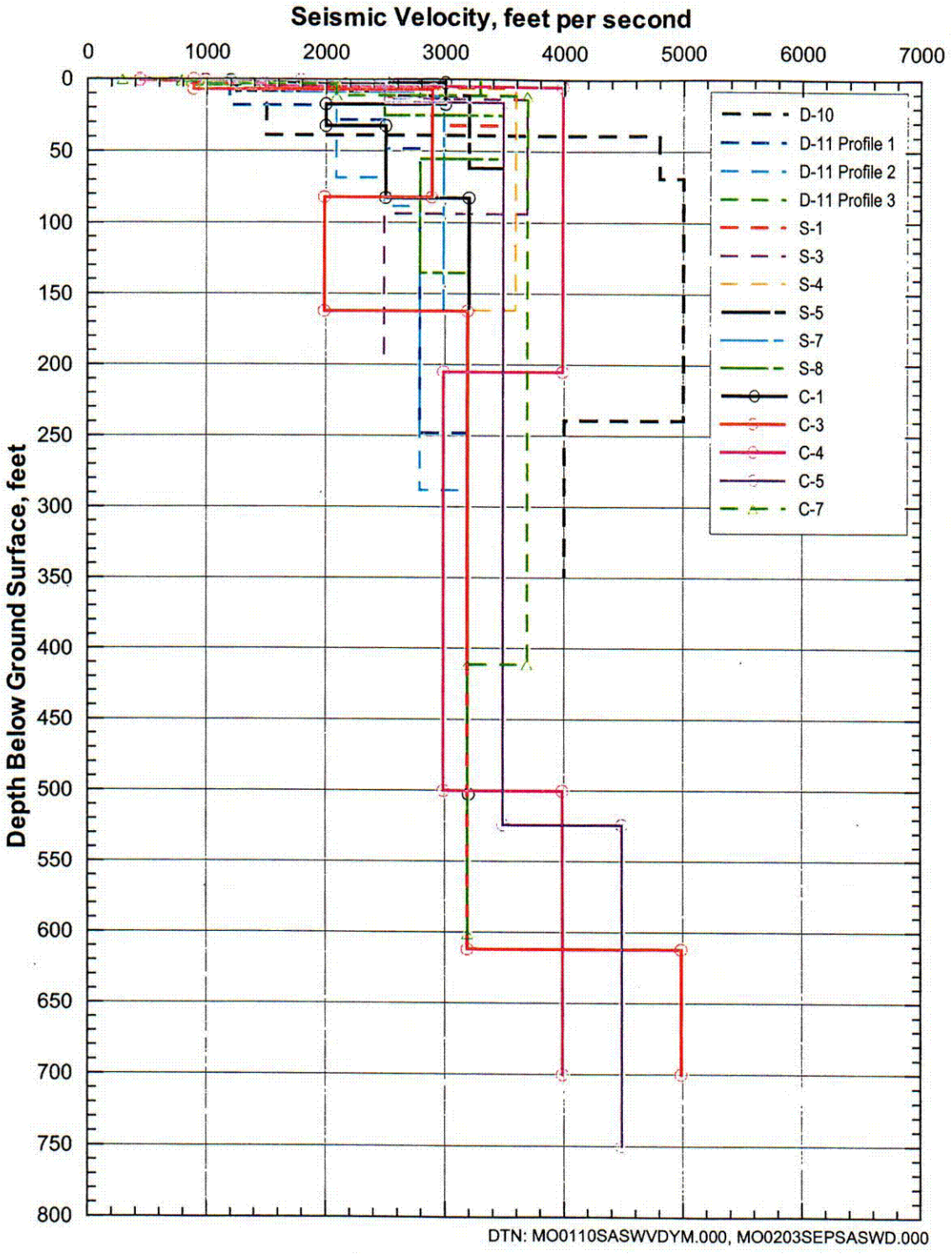

Figure 194. Shear-Wave Velocity Profiles from SASW Measurements Parallel to the Crest of Yucca Mountain

C08

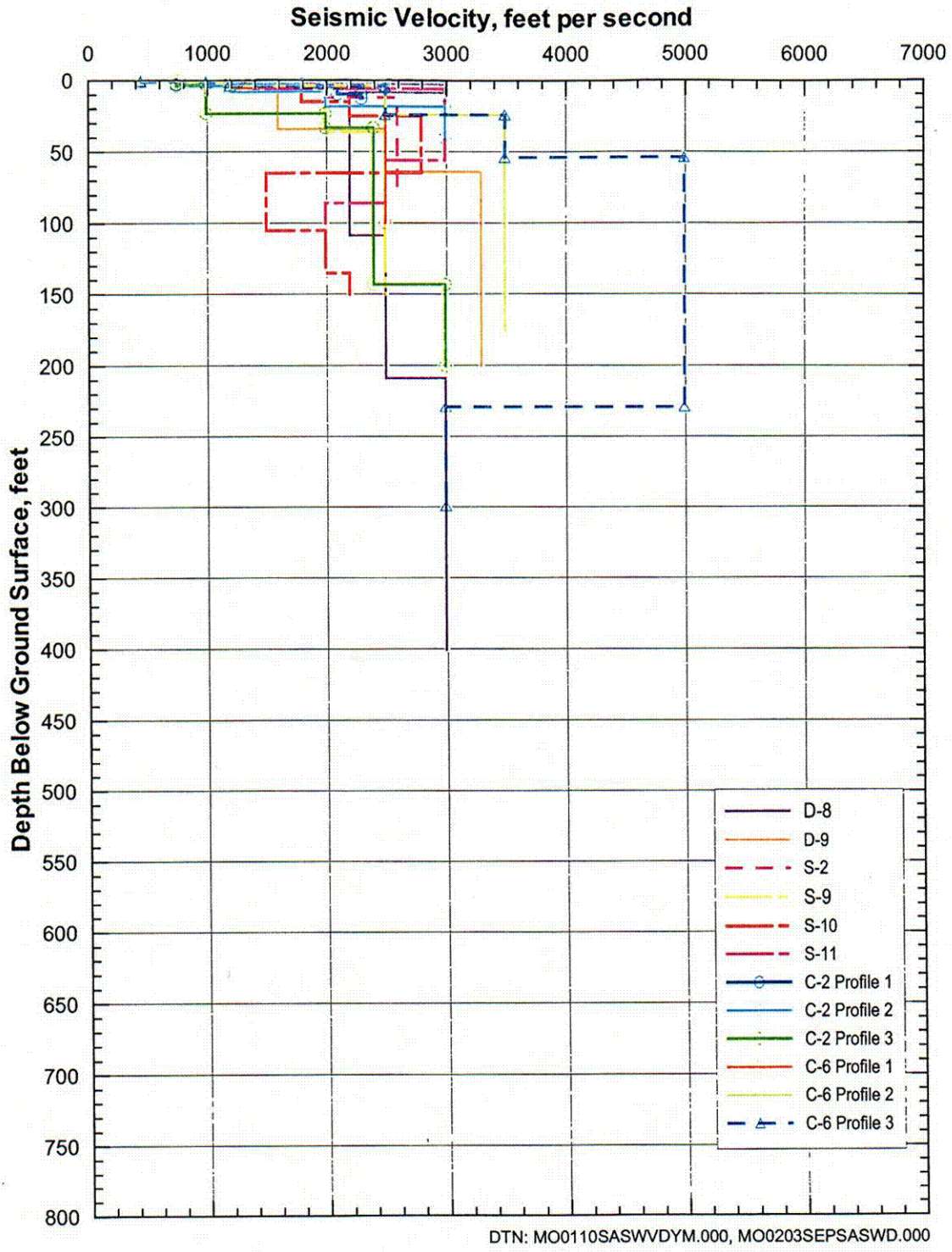

Figure 195. Shear-Wave Velocity Profiles from SASW Measurements Perpendicular to the Crest of Yucca Mountain

C09

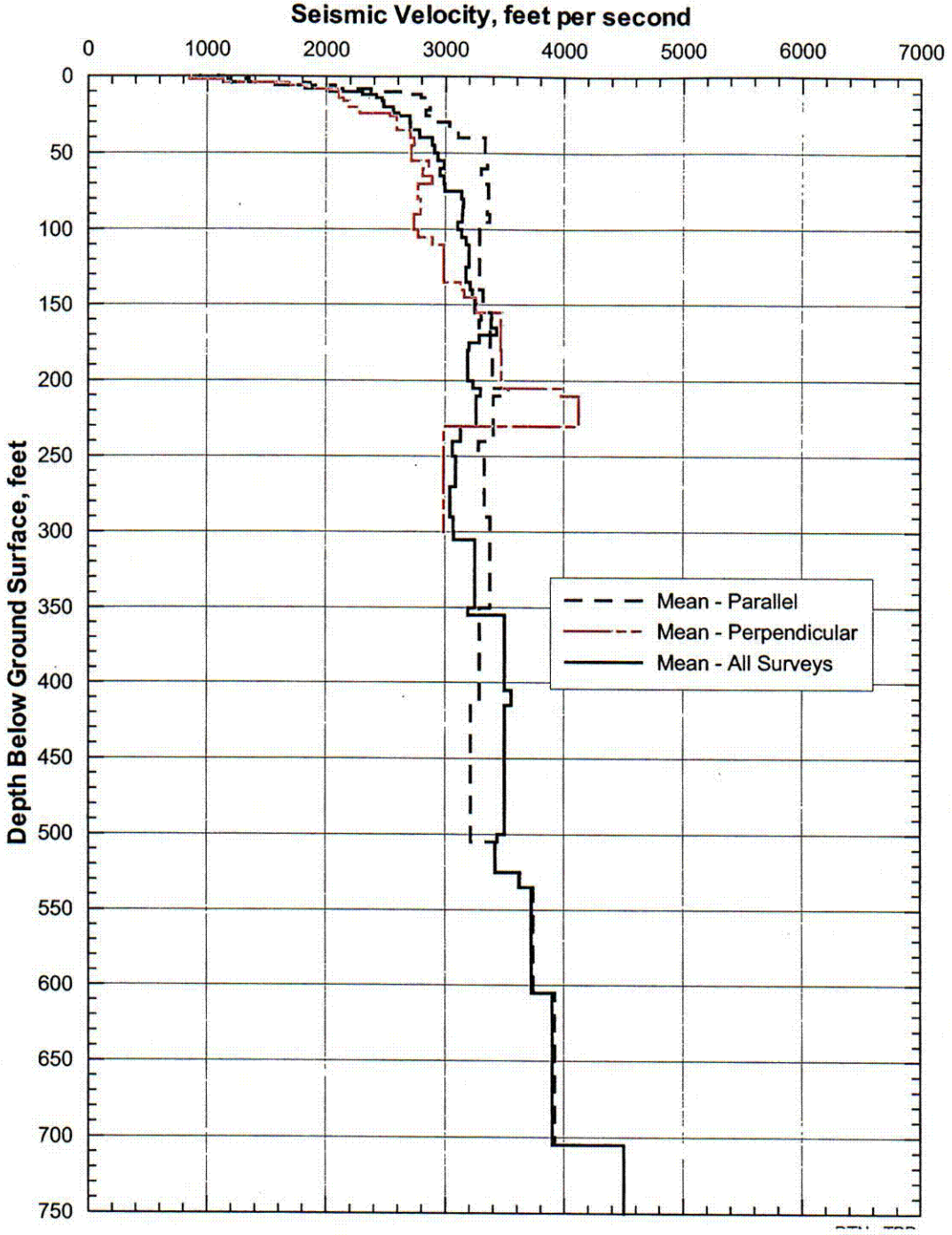

Note: These statistics have been calculated for illustrative purposes only. Final statistics calculated for use in the forthcoming scientific analysis entitled *Development of Seismic Design Input Ground Motions for a Geologic Repository at Yucca Mountain* will be submitted to the TDMS.

Figure 196. Comparison of Mean Shear-Wave Velocity Profiles from SASW Measurements Relative to the Orientation to the Crest of Yucca Mountain

C10

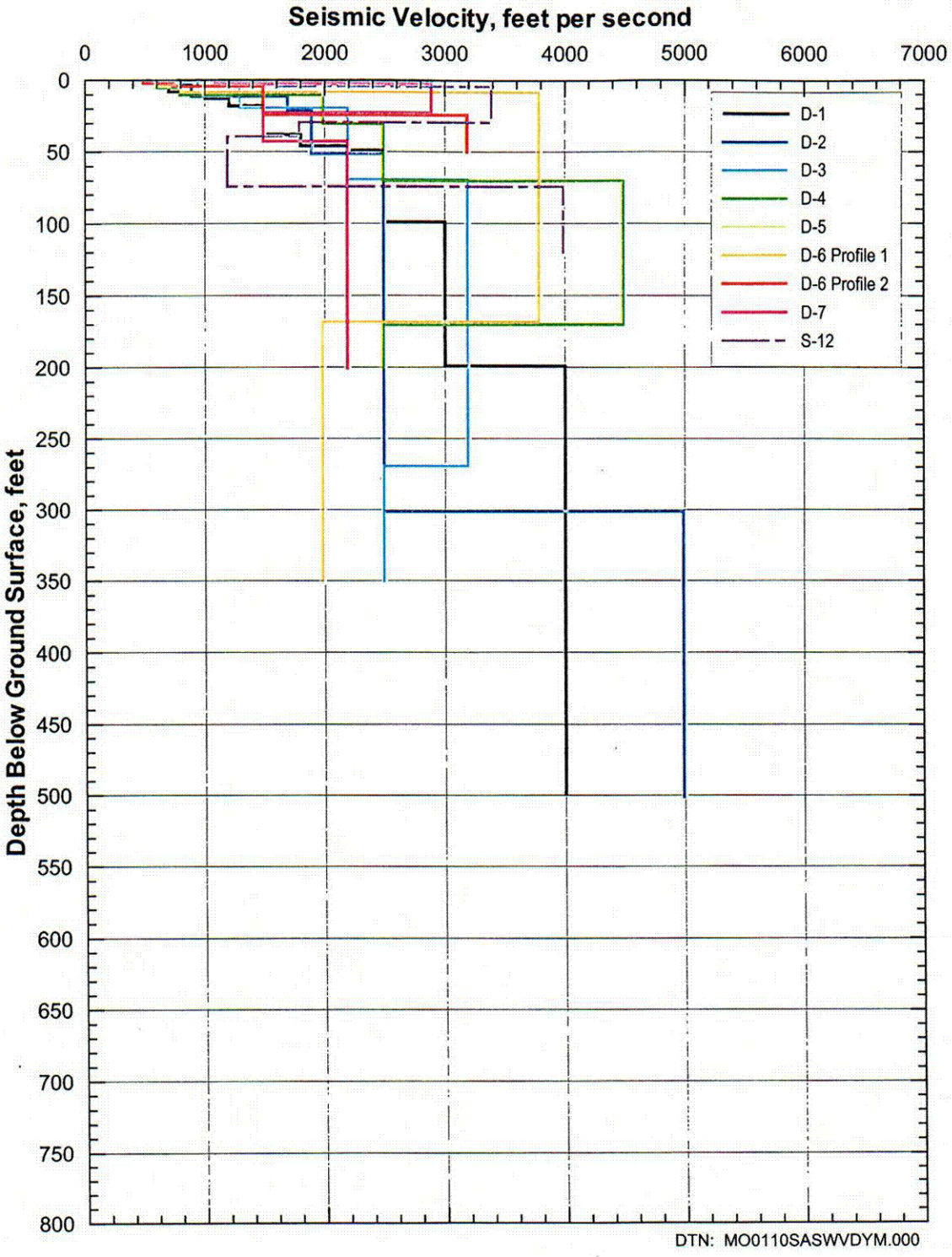

Note: D-5 and D-6, Profile 1, have identical profiles (line for D-5 is hidden by line for D-6, Profile 1).

Figure 197. Shear-Wave Velocity Profiles Off the Crest of Yucca Mountain

C11

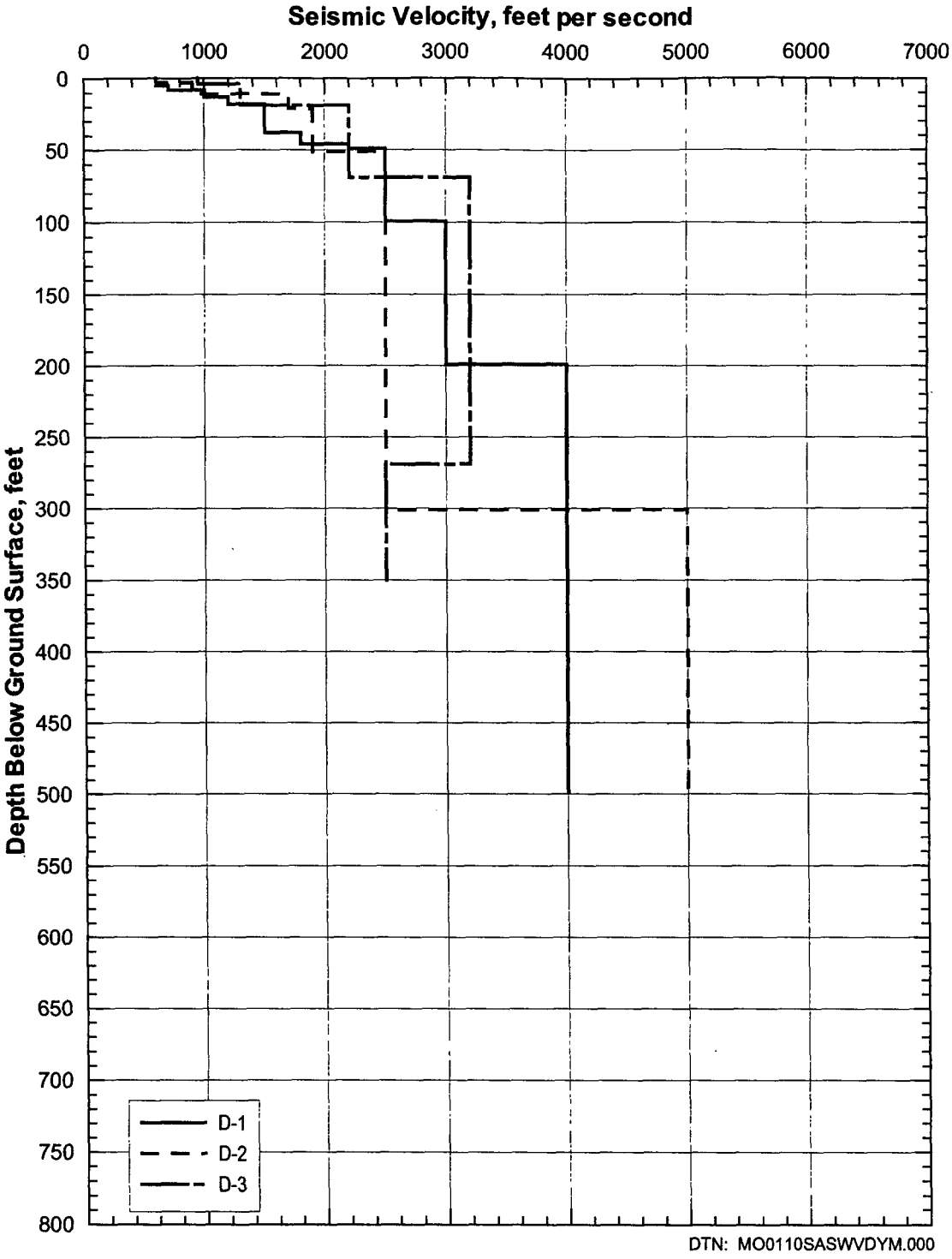

Figure 198. Shear-Wave Velocity Profiles from SASW D-1, D-2, and D-3

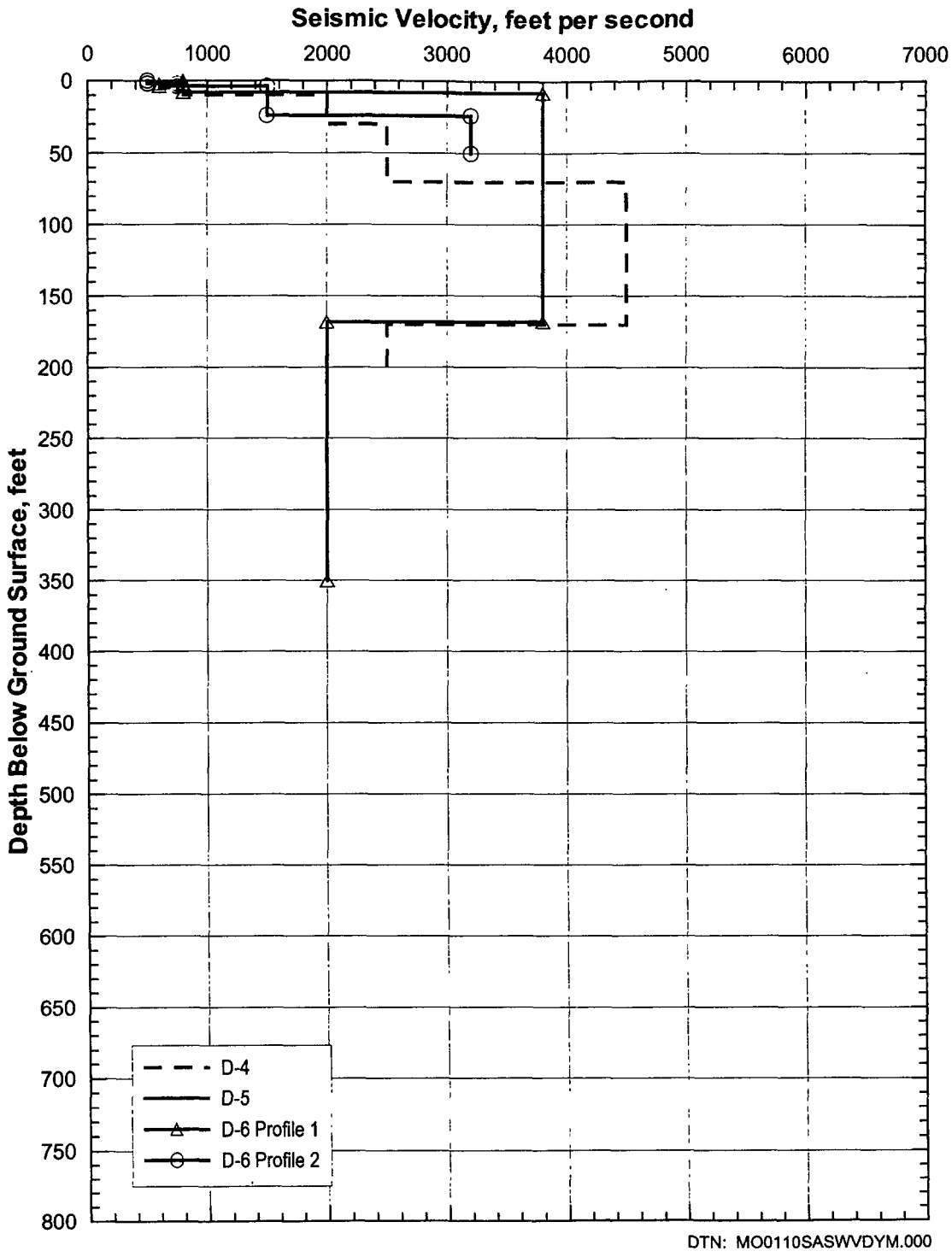

Figure 199. Shear-Wave Velocity Profiles from SASW D-4, D-5, and D-6

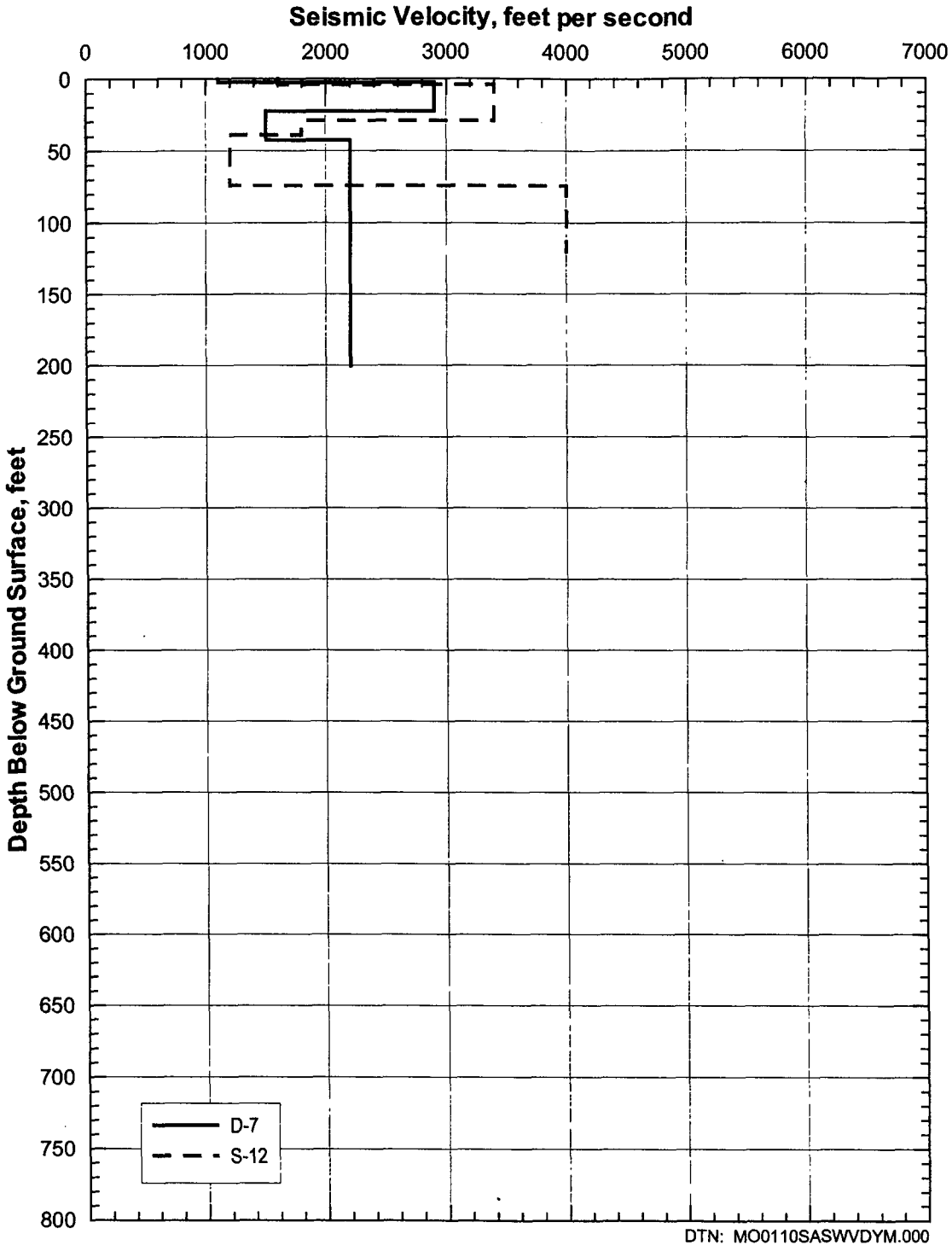

Figure 200. Shear-Wave Velocity Profiles from SASW D-7 and S-12

Three SASW surveys (R-1 to R-3) were performed to measure the shear-wave velocity of the exposed, visually intact (although weathered) rock (Figure 157). The rock outcrop size allowed only very close receiver spacings (0.5 ft to 1 ft) to be used. Figure 191 presents the three shear-wave velocity profiles estimated from these sites. The velocities range from 3,200 to 4,700 ft/s.

It is interesting to note that the shear-wave velocities from the exposed rock are much higher than the velocities recorded for wavelengths ranging from approximately 5 to 20 ft from the other surveys. For example, at C-1 adjacent to R-1 (Figure 157), the shear-wave velocities near the surface (top 5 ft) are on the order of 1,100 ft/s, much less than the 4,700 ft/s recorded at R-1. Likewise at C-3, the velocity in the top 7 ft is 900 ft/s compared with 4,000 ft/s at R-2. At D-10, the quality of the near-surface dispersion curve is poor and shows some variability; however, the same trend of lower velocities as compared with the rock site is observed. These results illustrate the difference between local and global measurements of surface-wave velocity at a discontinuous rock/soil site with lateral variability. Although there are localized regions of intact higher velocity rock, the SASW method at longer spacings measures the velocity of a larger area consisting of the matrix of rock, damaged rock, and infill material.

The results from D-11 indicate that, in some cases, these locally stiff regions may be detected by SASW measurements. Figure 201 shows the dispersion curve recorded from D-11. At shorter wavelengths (shallow penetration, close receiver spacings, and small lateral extent), it can be seen that three different shear-wave velocities are measured over similar wavelength ranges. These multiple dispersion curves indicate local regions of different stiffness that are detected by the SASW method. As the receivers are spread out and a larger volume of the ground is sampled, the global velocity is measured. The stiffest region measured at D-11 had a shear-wave velocity of 3,300 ft/s, which is within the range of velocities measured at the intact rock sites. The three profiles determined at D-11 are presented on Figure 178.

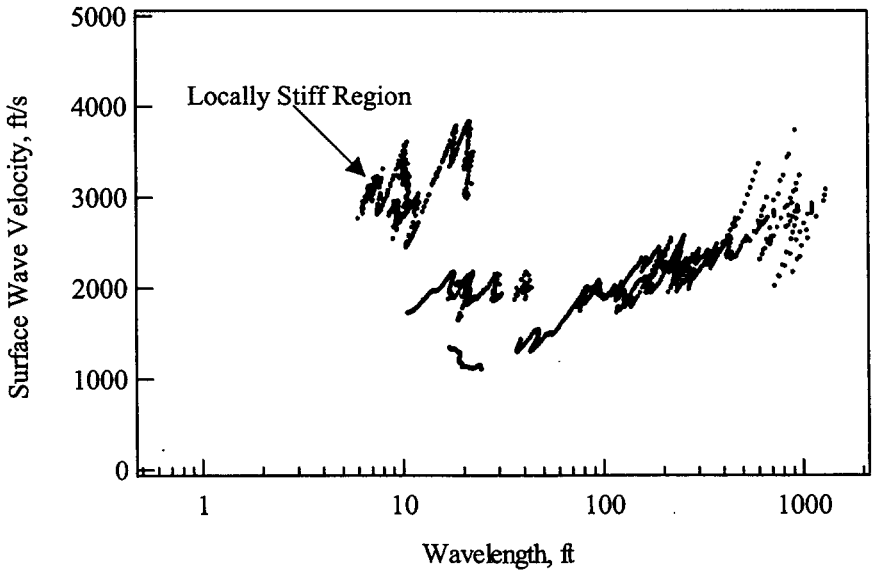

Source: Wong (2002a, Appendix 37)

Figure 201. Experimental Dispersion Curve Recorded at D-11 showing the Variability in Surface Wave Velocity at Shallow Depths